Advances in Whole-Brain Diffusion MRI at High and Ultra-High Field

Inaugural-Dissertation

zur Erlangung des Doktorgrades
der Mathematisch-Naturwissenschaftlichen Fakultät
der Heinrich-Heine-Universität Düsseldorf

vorgelegt von
Marten Veldmann
aus Nordhorn

Düsseldorf, den 22.10.2024

Gedruckt mit der Genehmigung der Mathematisch-Naturwissenschaftlichen Fakultät
der Heinrich-Heine-Universität Düsseldorf

Erstgutachter:	Prof. Dr. Tony Stöcker
Zweitgutachter:	Prof. Dr. Thomas Heinzel
Tag der mündlichen Prüfung:	21.02.2025
Erscheinungsjahr:	2025

Contents

Summary

Magnetic Resonance Imaging (MRI) is an essential tool in both clinical diagnostics and research, offering a wide range of contrast mechanisms for imaging anatomical structures and assessing tissue properties. One key MRI application is diffusion-weighted imaging (DWI), which sensitizes the MRI signal to the diffusive motion of water molecules, enabling the investigation of tissue microstructure. This is especially valuable for imaging the human brain, as DWI can reveal white matter pathways by measuring diffusion anisotropy. DWI provides a non-invasive method to indirectly assess structures on the micrometer scale, despite MRI's typical millimeter-scale spatial resolution. This thesis focuses on the design of fast sequences for whole-brain DWI, which are combined with techniques for correcting field inhomogeneity effects at high (3T) and ultra-high (7T) field strengths.

In the first part, a framework for open-source sequence development and image reconstruction is presented. Different open-source tools for sequence design, image reconstruction and image analysis were combined to form a workflow that allows rapid prototyping of MR sequences and reconstructions, can be shared among other researchers, and is independent from proprietary software. The workflow was validated by acquiring and reconstructing data from different MRI scanners of different vendors. Example applications included a 3D gradient echo (GRE) sequence with controlled aliasing (CAIPIRINHA) acceleration, mapping of static deviations from the main magnetic field B_0 and non-Cartesian imaging with spiral k-space trajectories. Both Cartesian and non-Cartesian image reconstruction algorithms were integrated into the workflow using open-source image reconstruction toolboxes. The reconstruction algorithms included optional k-space trajectory correction using the gradient impulse response function and correction for magnetic field inhomogeneity. The workflow was additionally integrated into the MRI simulation framework JEMRIS to allow direct comparison of experimental results to simulation results. The proposed pipeline was extensively used for sequence design and image reconstruction in the subsequent chapters.

The second part describes the improvement of non-invasive axon radius estimation in the human white matter using a multiband spiral sequence on a 3T scanner with a high-performance gradient system. Magnetic field monitoring was used to reduce artifacts stemming from dynamic field inhomogeneities, mainly caused by eddy currents during

the course of the DWI sequence. The actual encoding fields, measured up to the third spatial order, and static magnetic field inhomogeneities, measured using a dual-echo GRE sequence, were both incorporated into the image reconstruction algorithm. The spiral sequence was compared to the current gold standard multiband echo-planar imaging (EPI) sequence with image-based field corrections. An established diffusion-weighted imaging protocol, which showed reproducible results in a previous study, was used to estimate axon radii in white matter voxels. Strong diffusion weighting was applied to suppress all extra-axonal signals, enabling the use of a single-compartment model for the intra-axonal space. The axon radii were then estimated from the orientationally averaged DWI signal. A test–retest study was performed to assess the repeatability of axon radius estimation with EPI and spiral sequences. The higher signal-to-noise ratio (SNR) provided by the spiral readout led to reduced test–retest variability of axon radius estimates. Incorporating the actual encoding fields in the image reconstruction algorithm effectively reduced artifacts related to eddy currents, which are caused by strong diffusion gradients. However, a significant bias was detected in the test–retest measurements of some subjects for both EPI and spiral sequences, indicating a potential issue with the repeatability of axon radius estimation.

In the third part a new variant of the 3D dual refocusing echo acquisition mode (3DREAM) sequence is developed at a 7T scanner. The 3DREAM sequence allows for mapping of the B_1 field, which is a prerequisite for parallel transmit (pTx) techniques. The new variant uses a 3D stack-of-spirals instead of a Cartesian readout scheme, with the aim of reducing blurring and increasing the effective resolution in B_1 maps. The blurring is caused by the fast decay of the stimulated echo signal, which is prepared only once at the beginning of the sequence and decays with each following excitation. Using a spiral readout allows for more efficient k-space sampling, thus reducing the number of excitations. The spiral 3DREAM sequence was compared to the Cartesian 3DREAM sequence and three other established B_1 mapping methods in phantom and in-vivo measurements. Both 3DREAM sequences showed excellent agreement with the three other methods, while their acquisition time was significantly lower. Blurring and ventricular contrast in B_1 maps were reduced for the spiral 3DREAM compared to Cartesian 3DREAM, with the reduction becoming more significant at higher resolutions.

In the last part of this thesis, whole-brain DWI is performed on an ultra-high field (7T) scanner. At ultra-high fields the inhomogeneity of the B_1 field leads to severe signal dropouts in lower brain areas such as the cerebellum. An eight transmit channel RF coil and specifically designed pTx pulses were used to mitigate these inhomogeneities. Multiband pTx pulses were integrated into EPI and spiral DWI sequences. Static and dynamic field inhomogeneities were addressed by using field monitoring and static B_0 field mapping. The performance of the pTx pulses was compared to standard circularly polarized pulses. EPI and spiral images reconstructed with field monitoring data were compared to EPI data with image-based field inhomogeneity correction. It was found

that deteriorating effects of B_1 inhomogeneities were largely resolved by using pTx pulses. Increased signal in the cerebellum improved diffusion tensor fitting and resulted in more accurate fractional anisotropy and mean diffusivity maps. A remaining challenge is the low bandwidth of the pTx pulses, which results in bended slices in regions with large B_0 inhomogeneity. In accordance to the results of part two, the SNR for spiral DWI was increased compared to EPI DWI. However, at a field strength of 7T, static B_0 inhomogeneity posed a more severe problem in image reconstruction compared to 3T, as artifacts such as geometric distortions and blurring could not be fully resolved.

Zusammenfassung

Die Magnetresonanztomographie (MRT) ist ein wesentliches Werkzeug sowohl in der klinischen Diagnostik als auch in der Forschung. Sie bietet verschiedene Kontrastmechanismen zur Abbildung anatomischer Strukturen und zur Untersuchung von Gewebeeigenschaften. Eine Schlüsselanwendung der MRT ist die diffusionsgewichtete Bildgebung (DWI), die das MR-Signal auf die diffusive Bewegung von Wassermolekülen sensibilisiert und somit die Untersuchung der Gewebemikrostruktur ermöglicht. Dies ist besonders wertvoll für die Bildgebung des menschlichen Gehirns, da die DWI durch Messung der Diffusionsanisotropie Nervenfaserbahnen in der weiße Substanz sichtbar machen kann. DWI ist eine nicht-invasive Methode, die es erlaubt Strukturen im Mikrometerbereich sichtbar zu machen, obwohl die räumliche Auflösung der MRT typischerweise im Millimeterbereich liegt. Diese Dissertation konzentriert sich auf die Entwicklung schneller Sequenzen für die DWI des gesamten Gehirns, die mit Techniken zur Korrektur von Feldinhomogenitäten bei hohen (3T) und ultra-hohen (7T) Feldstärken kombiniert werden.

Im ersten Teil wird eine Entwicklungsumgebung für Pulssequenzen und Bildrekonstruktionsalgorithmen vorgestellt, die quelloffene Software nutzt. Verschiedene quelloffene Tools für Sequenzdesign, Bildrekonstruktion und Bildanalyse wurden kombiniert, um einen Workflow zu erstellen, der eine schnelle Prototypenentwicklung von MRT Sequenzen und Rekonstruktionsalgorithmen ermöglicht, mit anderen Forschern geteilt werden kann und unabhängig von proprietärer Software ist. Der Workflow wurde validiert, indem Daten mit verschiedenen MRT-Scannern unterschiedlicher Hersteller akquiriert und rekonstruiert wurden. Beispielanwendungen umfassten eine 3D Gradienten-Echo (GRE) Sequenz mit „controlled aliasing (CAIPIRINHA)“-Beschleunigung, Messung von statischen Magnetfeldabweichungen und nicht-kartesische Bildgebung mit spiralförmigen k-Raum-Trajektorien. Sowohl kartesische als auch nicht-kartesische Bildrekonstruktionsalgorithmen wurden unter Verwendung von quelloffener Software in den Workflow integriert. Die Rekonstruktionsalgorithmen beinhalteten eine optionale Korrektur von k-Raum-Trajektorien unter Verwendung der Gradienten-Impuls-Antwort-Funktion und Korrekturen für Magnetfeldinhomogenitäten. Der Workflow wurde zusätzlich in die MRT-Simulationssoftware JEMRIS integriert, um einen direkten Vergleich der experimentellen Ergebnisse mit Simulationsergebnissen zu ermöglichen. Der entwickelte Workflow wurde in den darauffolgenden Kapiteln ausgiebig für die Sequenzentwicklung und

die Bildrekonstruktion verwendet.

Der zweite Teil beschreibt die Verbesserung der nicht-invasiven Quantifizierung des Axonradius in der weißen Substanz des menschlichen Gehirns unter Verwendung einer Multiband-Spiralsequenz an einem 3T-Scanner mit einem Hochleistungsgradientensystem. Messungen der Gradientenfelder mit räumlich verteilten Magnetfeldsonden wurden durchgeführt, um Artefakte zu reduzieren, die durch dynamische Feldinhomogenitäten entstehen, welche hauptsächlich durch Wirbelströme während der DWI-Sequenz verursacht werden. Die tatsächlichen Gradientenfelder, gemessen bis zur dritten Raumordnung, sowie statische Magnetfeldinhomogenitäten, gemessen mit einer GRE-Sequenz mit zwei verschiedenen Echozeiten, wurden in den Bildrekonstruktionsalgorithmus integriert. Die Spiralsequenz wurde mit dem aktuellen Goldstandard, einer Multiband „Echo-Planar Imaging (EPI)“ Sequenz mit bildbasierten Feldkorrekturen verglichen. Ein etabliertes diffusionsgewichtetes Bildgebungsprotokoll, das in einer früheren Studie reproduzierbare Ergebnisse zeigte, wurde verwendet, um Axonradien in Voxeln innerhalb der weißen Substanz abzuschätzen. Starke Diffusionsgewichtung wurde angewendet, um das MR Signal außerhalb der Axone zu unterdrücken, wodurch die Modellierung des diffusionsgewichteten Signals auf den intra-axonalen Raum beschränkt werden kann. Die Axonradien wurden dann aus dem über alle Raumrichtungen gemittelten DWI Signal berechnet. Eine Test-Retest-Studie wurde durchgeführt, um die Wiederholbarkeit der Axonradius Messung mit EPI- und Spiralsequenzen zu bewerten. Das höhere Signal-Rausch-Verhältnis (SNR), das durch die Spiraltrajektorie erreicht wurde, führte zu einer reduzierten Test-Retest-Variabilität der Axonradiusmessungen. Die Einbeziehung der gemessenen Gradientenfelder in den Bildrekonstruktionsalgorithmus reduzierte Artefakte, die von Wirbelströmen aufgrund starker Diffusionsgradienten verursacht werden. Es wurde jedoch ein signifikanter systematischer Fehler in den Test-Retest-Messungen bei einigen Probanden sowohl für EPI- als auch für Spiralsequenzen festgestellt, was auf ein potenzielles Problem bei der Wiederholbarkeit der Axonradiusmessungen hindeutet.

Im dritten Teil wurde eine neue Variante der „3D Dual Refocusing Echo Acquisition Mode (3DREAM)“-Sequenz an einem 7T MRT entwickelt. Die 3DREAM Sequenz erlaubt die Messung des Radiofrequenzfeldes B_1, was eine Vorraussetzung für die Nutzung von parallelen Sendetechniken (pTx) ist. Die Sequenz verwendet einen 3D Stapel von Spiralen anstelle einer kartesischen Auslesetrajektorie, um Bildunschärfe zu reduzieren und die effektive Auflösung in B_1-Karten zu erhöhen. Diese Unschärfe wird durch den schnellen Zerfall des stimulierten Echosignals verursacht, das nur einmal zu Beginn der Sequenz präpariert wird und mit jeder folgenden Anregung zerfällt. Die Verwendung einer Spiraltrajektorie ermöglicht eine effizientere k-Raum-Abtastung, wodurch die Anzahl der Anregungen reduziert wird. Die Spiral-3DREAM Sequenz wurde mit der kartesischen 3DREAM-Sequenz und drei anderen etablierten B_1-Messmethoden in Phantom- und in-vivo-Messungen verglichen. Beide 3DREAM-Sequenzen zeigten eine hervorragende Übereinstimmung mit den drei anderen Methoden, während ihre Akquisitionszeit deut-

lich kürzer war. Bildunschärfe und ventrikulärer Kontrast in B_1-Karten wurden bei der Spiral-3DREAM im Vergleich zur kartesischen 3DREAM reduziert, wobei die Reduktion bei höheren Auflösungen stärker ausgeprägt ist.

Im letzten Teil dieser Dissertation wurde die diffusionsgewichtete Bildgebung des gesamten Gehirns an einem Ultra-Hochfeld (7T) MRT durchgeführt. Bei ultra-hohen Feldstärken führt die Inhomogenität des B_1-Feldes zu erheblichen Signalausfällen in unteren Hirnregionen wie dem Kleinhirn. Eine achtkanalige Radiofrequenzspule und speziell entwickelte parallele Transmissionspulse (pTx Pulse) wurden verwendet, um diese Inhomogenitäten zu verringern. Multiband pTx Pulse wurden in EPI- und Spiral-DWI-Sequenzen integriert. Statische und dynamische Feldinhomogenitäten wurden durch Messung der Gradientenfelder und der statischen B_0 Abweichungen korrigiert. Die pTx Pulse wurden mit zirkular polarisierten Pulsen verglichen. EPI- und Spiralbilder, die unter Berücksichtigung der gemessenen Gradientenfelder und statischen B_0 Abweichungen rekonstruiert wurden, wurden mit EPI-Daten mit bildbasierter Feldinhomogenitätskorrektur verglichen. Es wurde festgestellt, dass die negativen Auswirkungen von B_1-Inhomogenitäten auf die Bildqualität durch die Verwendung von pTx Pulsen weitgehend behoben werden konnten. Ein erhöhtes SNR im Kleinhirn verbesserte den Fit eines Diffusionstensors an die DWI Daten und führte zur genaueren Quantifizierung der fraktionellen Anisotropie- und mittleren Diffusivität in diesem Hirnbereich. Eine verbleibende Herausforderung ist die geringe Bandbreite der pTx Pulse, die zu gekrümmten Schichten in Bereichen mit großen B_0-Inhomogenitäten führt. In Übereinstimmung mit den Ergebnissen des zweiten Teils war das SNR der Spiral-DWI Sequenz im Vergleich zur EPI-DWI Sequenz erhöht. Bei einer Feldstärke von 7T stellten im Vergleich zu einer Feldstärke von 3T jedoch statische B_0-Inhomogenitäten ein größeres Problem bei der Bildrekonstruktion dar, da Artefakte wie geometrische Verzerrungen und Bildunschärfe nicht vollständig behoben werden konnten.

Chapter 1

Introduction

Magnetic resonance imaging (MRI) is one of the most versatile imaging modalities in clinical diagnosis and research. It provides a wide range of contrasts, which can be used to visualize anatomical structures, tissue properties, and functional information. One important contrast mechanism is the ability to sensitize the MRI signal to the diffusive motion of water molecules [1]. This sensitivity is exploited in diffusion-weighted MRI (DWI), which is used to probe tissue microstructure in the brain and other organs [2]. For example, investigation of diffusion anisotropy in the human brain can reveal neural pathways in the white matter [3]. While the typical spatial resolution of MRI is in the order of millimeters, DWI provides an indirect measure of tissue structure on a micrometer level. Diffusion-sensitizing gradients generate a signal loss that depends on the displacement of water molecules during the diffusion time. These displacements are on the order of micrometers during typical diffusion times employed in DWI. This principle is the foundation of all modern DWI pulse sequences.

The design of diffusion-weighted MRI pulse sequences and the development of advanced image reconstruction methods for these sequences are active fields of research. Pulse sequence development for DWI includes improvements of radiofrequency (RF) waveforms and readout gradients, as well as the development of new diffusion-sensitizing gradient waveforms. Improvements in the design of RF pulses and readout gradients aim to reduce image artifacts, decrease acquisition times and increase the signal-to-noise ratio (SNR), while new diffusion-sensitizing waveforms are developed to reduce peripheral nerve stimulation, reduce artifacts related to eddy currents, or accomodate specific advanced biophysical models.

Until today, the gold standard acquisition for whole-brain DWI is a multiband single-shot echo-planar imaging (MB-EPI) sequence [4]. However, MB-EPI has some limitations, such as long echo times resulting in reduced signal and long readout times, which lead to geometric distortions and susceptibility artifacts. Spiral imaging has gained interest as an alternative to EPI [5], [6], as it provides higher SNR due to shorter echo times and more time-efficient k-space sampling. However, spiral imaging also poses challenges, as it requires non-Cartesian image reconstruction and correction for field inhomogeneity effects.

Imaging at higher field strengths is another way to increase SNR [7], but field inhomogeneity effects also become more pronounced. Inhomogeneities of the main magnetic field and the encoding gradients lead to severe image artifacts such as geometric distortions, while inhomogeneity of the RF field causes SNR reduction especially in lower areas of the brain. Different strategies to mitigate these field inhomogeneity effects have been proposed. Magnetic field monitoring [8] is a method to measure the actual encoding fields during a pulse sequence, enabling the correction of dynamic field effects, such as eddy currents, during image reconstruction [9]. Parallel transmit (pTx) techniques [10] allow more control over the spatial RF transmit field (B_1) distribution and can be used to mitigate the effects of B_1 inhomogeneity.

In this thesis, fast DWI sequences are combined with techniques for field inhomogeneity correction in order to improve DWI at high and ultra high field strengths. Chapter 2 gives an introduction to MRI and diffusion-weighted MRI (DWI). This chapter also includes a description of static and dynamic field inhomogeneity effects that disturb image encoding, and their quantification with field monitoring. The chapter continues with an introduction to fast imaging techniques for DWI and concludes with an overview of advanced image reconstruction techniques accounting for field inhomogeneity effects.

In Chapter 3, a framework for open-source sequence development and image reconstruction is described. Different open-source tools for sequence design, image reconstruction and data analysis are combined to form a workflow that allows flexible prototyping of MRI sequences and reconstructions, can be shared among other researchers and is independent from proprietary software. The workflow is validated by acquiring and reconstructing data from MRI scanners of various vendors. Additionally, it is integrated into an existing simulation framework to allow direct comparison of experimental to simulated results. The proposed workflow is used to design pulse sequences and implement image reconstruction algorithms, leading to the results of the subsequent chapters.

In Chapter 4, non-invasive axon radius estimation in the human white matter using a 3T scanner with a high-performance gradient system is described. An established diffusion-weighted imaging protocol that showed reproducible results in a previous study is modified by using a spiral instead of an EPI k-space trajectory. The spiral k-space trajectory is monitored with a magnetic field camera to reduce artifacts from magnetic field inhomogeneity. The aim of this study is to increase SNR of diffusion-weighted images at ultra-high b-values. A test–retest study is performed to compare the repeatability of axon radius estimation using EPI and spiral DWI sequences.

In chapter 5, a variant of the 3D dual refocusing echo acquisition mode (3DREAM) sequence is proposed. The 3DREAM sequence allows for mapping of the B_1 field, which is a prerequisite for parallel transmit (pTx) techniques. The new variant uses a 3D stack-of-spirals instead of a Cartesian readout scheme to efficiently acquire 3D k-space and thus to reduce blurring in B_1 maps caused by fast decay of the stimulated echo signal. The new sequence is compared to the Cartesian 3DREAM sequence and three other established B_1 mapping methods in both phantom and in vivo measurements.

Chapter 6 investigates whole-brain DWI at 7T using multiband pTx pulses to mitigate effects of B_1 inhomogeneity in the brain. PTx pulses are integrated into both EPI and spiral DWI sequences, and the encoding fields of these sequences are monitored with a magnetic field camera. The performance of the pTx pulses is assessed in simulations and in vivo measurements by comparing SNR maps and slice profiles of pTx pulses to those of standard circularly polarized pulses. Additionally, EPI and spiral images reconstructed with field monitoring data are compared to EPI data with image-based field inhomogeneity correction. A diffusion tensor fit is performed for all images, and the resulting fractional anisotropy and mean diffusivity maps are compared.

Chapters 3 and 4 correspond to first author publications, chapter 5 corresponds to a shared first author publication and chapter 6 is partly based on abstracts presented at two conferences (ESMRMB 2023 and 2024). The publications including personal contributions are listed in the List of Publications.

Chapter 2

Background

2.1 Basic Principles of MRI

2.1.1 Nuclear Magnetic Resonance (NMR)

MRI is based on the physical phenomenom of nuclear magnetic resonance (NMR). NMR describes the behaviour of atomic nuclei in the presence of external magnetic fields and was discovered by Rabi in 1938 [11] and demonstrated in condensed matter by Bloch and Purcell in 1946 [12], [13]. The nuclei have a property called spin, which gives rise to a magnetic dipole moment, if the nuclei has nonzero spin. This is the case for all nuclei with an odd number of protons or neutrons. If a sample containing many nuclei is placed in an external magnetic field B_0, the spins in the sample tend to align with the external field, which polarizes the sample. As a result, a macroscopic magnetization can be observed, which equals the vector sum of all microscopic magnetic moments in the sample. This macroscopic magnetization increases with the field strength of the external field, the number of spins in the sample and the gyromagnetic ratio. It decreases with the temperature of the sample as thermal motion is counteracting the alignment of the spins with the external field. At room temperature, a high number of spins is required to obtain a measurable magnetization. Therefore, in MRI the most commonly used nucleus for imaging of the human body is the proton, as the body consists mostly of water molecules and the proton has a high gyromagnetic ratio of $\gamma = 42.58\,\mathrm{MHz\,T^{-1}}$. Typical field strengths in MRI are in the range of 1.5 to 7 Tesla, which corresponds to Larmor frequencies of 63 to 300 MHz for protons.

If the magnetic moments are not aligned with the direction of the external magnetic field, a torque acts on them. This causes a motion that is analogous to the precession of a spinning top in the gravity field. The precession frequency ω_0 is called the Larmor frequency and is defined by

$$\omega_0 = \gamma B_0, \tag{2.1}$$

where B_0 is the magnetic field strength of the external field.

By applying a radio frequency (RF) field B_1 oscillating at the Larmor frequency perpendicular to B_0, the macroscopic magnetization is tipped away from the direction of the main magnetic field B_0 towards the transverse plane. This process is called excitation and the rotation angle is called flip angle. The magnetization now precesses around the main magnetic field and an alternating current – the NMR signal – can be measured in a coil, that is placed around the sample. The time evolution of the macroscopic magnetization vector during and after excitation can be described in a classical way by the Bloch equation [12]. To simplify the description of the process of excitation, a rotating frame of reference oscillating at the Larmor frequency is defined. In this rotating

frame the B_1 field is stationary. The Bloch equation for the excitation reads

$$\frac{\mathrm{d}\boldsymbol{M}_{\mathrm{rot}}}{\mathrm{d}t} = \gamma \boldsymbol{M}_{\mathrm{rot}} \times \boldsymbol{B}_{\mathrm{eff}}, \tag{2.2}$$

where $\boldsymbol{M}_{\mathrm{rot}}$ refers to the magnetization vector in the rotating frame, and $\boldsymbol{B}_{\mathrm{eff}}$ denotes the effective magnetic field. If B_0 points into z-direction and B_1 with amplitude $\hat{B}_1$ into x-direction, the effective field is given by

$$\boldsymbol{B}_{\mathrm{eff}} = \hat{B}_1 \boldsymbol{e}_x + (B_0 - \frac{\omega}{\gamma})\boldsymbol{e}_z. \tag{2.3}$$

In the case of on-resonant excitation, meaning all spins precess at the Larmor frequency ($\omega = \omega_0$), the effective field becomes $B_{\mathrm{eff}} = \hat{B}_1 \ \boldsymbol{e}_x$. In this case, the flip angle is

$$\alpha(t) = \gamma \int_0^t \hat{B}_1(\tau)\mathrm{d}\tau. \tag{2.4}$$

Off-resonance can be caused by inhomogeneity of the main magnetic field and properties of the sample as chemical shift and susceptibility. Off-resonances lead to a less effective excitation and therefore to a lower flip angle as the rotation axis is altered. Controlled off-resonances in the form of magnetic field gradients can be used to only excite parts of the sample.

After excitation, the magnetization gradually returns to its equilibrium state. This process is called relaxation. Including relaxation, the Bloch equation in the laboratory frame is given by

$$\frac{\mathrm{d}\boldsymbol{M}}{\mathrm{d}t} = \gamma \boldsymbol{M} \times \boldsymbol{B} - \frac{M_z - M_0}{T_1} \ \boldsymbol{e}_z - \frac{M_x \boldsymbol{e}_x + M_y \boldsymbol{e}_y}{T_2}. \tag{2.5}$$

Here T_1 and T_2 are the longitudinal and the transverse relaxation constants. The longitudinal magnetization returns to equilibrium by exchanging energy with the surrounding tissue in the form of heat transfer, which is described by the time constant T_1. Transverse relaxation always accompanies longitudinal relaxation, but can additionally occur due to spin-spin interactions, causing spins to irreversibly lose their phase coherence or 'dephase', leading to the decay of transverse magnetization towards zero, characterized by the time constant T_2. Magnetic field inhomogeneities and susceptibility effects further decrease the transverse relaxation time, resulting in a T_2^* relaxation time. The values of T_1 and T_2 vary depending on the tissue, making them important contrast parameters for MR imaging.

The measurable NMR signal after excitation is also called free induction decay (FID). The time evolution of the FID signal $S(t)$ of a sample with volume V is described by the signal equation

$$S(t) = \int_V M_{xy}(t, \boldsymbol{r}) \ \mathrm{d}^3 r. \tag{2.6}$$

The evolution of the transverse magnetization after excitation can be calculated using the Bloch equation. In the case of a homogenous main magnetic field $\boldsymbol{B} = B_0\boldsymbol{e}_z$ and an ideal excitation with resulting magnetization $\boldsymbol{M}(\boldsymbol{r}) = M_0(\boldsymbol{r})\boldsymbol{e}_x$, the longitudinal and transverse components of the Bloch equation decouple. If further all spins precess at the Larmor frequency and T_2 is spatially constant, the solution for the transverse magnetization is

$$M_{xy}(t, \boldsymbol{r}) = M_0(\boldsymbol{r})e^{-i\omega_0 t}e^{-\frac{t}{T_2}}. \tag{2.7}$$

The resulting signal oscillates at the Larmor frequency decays with the transverse relaxation time constant T_2. The initial magnetization $M_0(\boldsymbol{r})$ is dependent on the spin density $\rho(\boldsymbol{r})$ of the sample: $M_0(\boldsymbol{r}) \sim \rho(\boldsymbol{r})$.

2.1.2 Spatial Encoding and k-space Formalism

The NMR signal contains much information on the properties of the investigated sample. The signal strength and shape is dependent on the spin density, relaxation times, chemical composition, magnetic field variation, motion of the molecules and many other factors. As the signal originates from all nuclei within the excited sample, a form of spatial encoding is required to derive spatial information from the measured signal. This is achieved by modifying the precession frequency with magnetic field gradients along the three spatial dimensions.

If a magnetic field gradient is applied along one spatial dimension, the precession frequency becomes dependent on the position of the spins. This is used to encode spatial information in the MRI signal. Three gradients are applied to encode the three spatial dimensions. The gradient fields are defined as

$$G_i = \frac{\mathrm{d}B_z}{\mathrm{d}r_i} \qquad i = x, y, z \tag{2.8}$$

and are typically in the order of $10 - 100\,\mathrm{mT/m}$. The magnetic field of the gradients point in the direction of the main field B_0, here the z-direction. The fields vary linearly in space along one of the three dimensions dependent on the distance r_i to the origin (the 'isocenter') of the gradient. If a magnetic field gradient is applied along the z-direction, the precession frequency in the rotating frame along the z-axis is

$$\omega(z) = \gamma z G_z. \tag{2.9}$$

Magnetic field gradients are used in different ways to encode spatial information. Three common concepts are slice selection, phase encoding and frequency encoding. In order to excite only one slice of a three-dimensional sample, a slice-selection gradient is applied along one dimension during the excitation RF pulse. This alters the precession frequency of the spins along the slice-selection axis. According to equation 2.3, spins that

do not precess at the frequency of the RF pulse are excited less effectively. The thickness of the excited slice Δz is dependent on the amplitude of the slice-selection gradient G_z, here in z-direction and the bandwidth Δf of the RF pulse:

$$\Delta z = \frac{2\pi\Delta f}{\gamma G_z}. \tag{2.10}$$

It can be shown that at small flip angles ($\leq 90°$) the excited frequency band profile corresponds to the Fourier Transform of the RF shape. Therefore, a rectangular frequency band is excited by an infinitely long sinc-shaped RF pulse. As infinitely long RF pulses are not feasible, often filtered sinc pulses with limited sidelobes are used in practice.

The other two spatial dimensions are encoded by applying gradients before (phase-encoding gradient G_y) and during (frequency-encoding gradient G_x) signal reception. The phase of the spins at time t during the application of a gradient, here in x-direction, is given by

$$\phi(x,t) = \omega(x,t)t = \gamma x G_x(t)t. \tag{2.11}$$

Frequency encoding leads to a time-varying phase of the spins during signal reception, while phase encoding modifies the phase of the spins before signal reception. As the phase of spins at different positions can not be disentangled from the MRI signal, phase encoding has to be repeated n times with different amplitudes of the phase-encoding gradient to encode a frequency. The solution of the Bloch equation in the rotating frame for the transverse magnetization in the presence of phase and frequency encoding gradients (ignoring relaxation) is given by:

$$M_{xy}(t) = \rho(\boldsymbol{r}) e^{-i\boldsymbol{r}\gamma \int_0^t \boldsymbol{G}(\tau)\mathrm{d}\tau}. \tag{2.12}$$

The signal in the rotating frame is then:

$$S(t) = \int_V \rho(\boldsymbol{r}) e^{-i\boldsymbol{r}\gamma \int_0^t \boldsymbol{G}(\tau)\mathrm{d}\tau} = \int_V \rho(\boldsymbol{r}) e^{-i\boldsymbol{k}(t)\boldsymbol{r}}\mathrm{d}\boldsymbol{r}. \tag{2.13}$$

From equation 2.13 the signal is identified as the Fourier transform of the spin density $\rho(\boldsymbol{r})$. The spatial frequency $\boldsymbol{k}(t)$ defines the position in k-space, which is a reciprocal space to the image space containing the spatial frequencies of the image. The path through k-space is referred to as the k-space trajectory, which is defined by:

$$\boldsymbol{k}(t) = \gamma \int_0^t \boldsymbol{G}(\tau)\mathrm{d}\tau. \tag{2.14}$$

Spatial information on the magnetization is reconstructed from the measured signal by applying an inverse Fourier transform to the signal, typically in form of a fast Fourier

transform (FFT), which assigns a grayscale value to each position in image space as shown in Figure 2.1. In the one-dimensional case, the spin density $\rho(x)$ after applying the inverse Fourier transform is given by

$$\rho(x) = \int_{k_x} S(k_x) \exp\left(2\pi i k_x x\right) \mathrm{d}k_x. \tag{2.15}$$

The k-space is an infinitely sized continuous three-dimensional space, where low spatial frequencies belong to the center of k-space and high frequencies to its periphery. In an MRI experiment the signal is successively acquired at N equidistant discrete positions in k-space dimension with distance Δk and a finite maximum k-space position $k_{\max}$. The finite and discrete sampling limits both the resolution and the field of view (FOV) of the image. Replacing the continuous integral in equation 2.15 by a sum with discrete positions yields

$$\rho(j\Delta x) = \sum_{l=0}^{N-1} S(k_x) \exp\left(2\pi i l j \Delta k_x \Delta x\right). \tag{2.16}$$

The j-th element of the one-dimensional inverse discrete Fourier transform (DFT) [14] of a series of data points d is defined as:

$$DFT^{-1}\left[d\right]_j = \frac{1}{N} \sum_{l=0}^{N-1} d_k \exp\left(2\pi i \frac{jl}{N}\right). \tag{2.17}$$

Comparing the exponents of equations 2.16 and 2.17, a relation between k-space sampling and the image geometry can be derived:

$$\Delta x \Delta k = \frac{1}{N}. \tag{2.18}$$

If the k-space is sampled from $-k_{\max}$ to $k_{\max}$ with $k_{\max} = \Delta k N/2$, the image resolution x is dependent on the maximum acquired spatial frequency:

$$\Delta x = \frac{1}{2k_x^{\max}}. \tag{2.19}$$

In practice the resolution is limited by decreased signal-to-noise ratio (SNR) due to dephasing of the spins caused by gradients, as well as relaxation and off-resonance effects. Typical resolutions achieved with modern MRI scanners are on the scale of 1-5 mm.

As the signal is acquired at discrete sampling points with sampling distance Δk, the reconstructed image repeats itself over a spatial interval – the FOV. It can be derived from equation 2.18:

$$FOV = N\Delta x = \frac{1}{\Delta k}. \tag{2.20}$$

This is known as the Nyquist sampling criterion, which states that the sampling frequency has to be twice as large as the maximum frequency in the signal to be recon-

structed. All signal stemming from outside the FOV will fold into the image, which is called aliasing. The FOV should therefore be chosen large enough to avoid such aliasing artifacts. Increasing either the FOV or the resolution requires a higher number of samples in k-space.

There are many different possibilities of covering k-space. One common way of k-space sampling is 2D 'spin-warp imaging'. One slice of a 3D volume is acquired by applying slice selection on one axis to excite a 2D slice, which is encoded by phase and frequency encoding gradients on the other two axes. The 2D k-space is sampled line-by-line by varying the amplitude of the phase encoding gradient.

Although the combination of a slice-selection, phase-encoding and frequency encoding gradient is a common way of encoding a three dimensional volume, other combinations of gradients are possible. For instance, the slice-selection gradient can be replaced by a second phase encoding gradient, if the whole volume instead of a single slice is excited. This is referred to as 3D imaging. It is also possible, to acquire multiple k-space lines or even the whole 2D k-space after one excitation pulse. Sampling on a non-equidistant (non-Cartesian) grid is also possible, but requires modifications to the reconstruction process, as the FFT can not be used anymore in a straightforward way. These fast imaging techniques are further discussed in section 2.4.

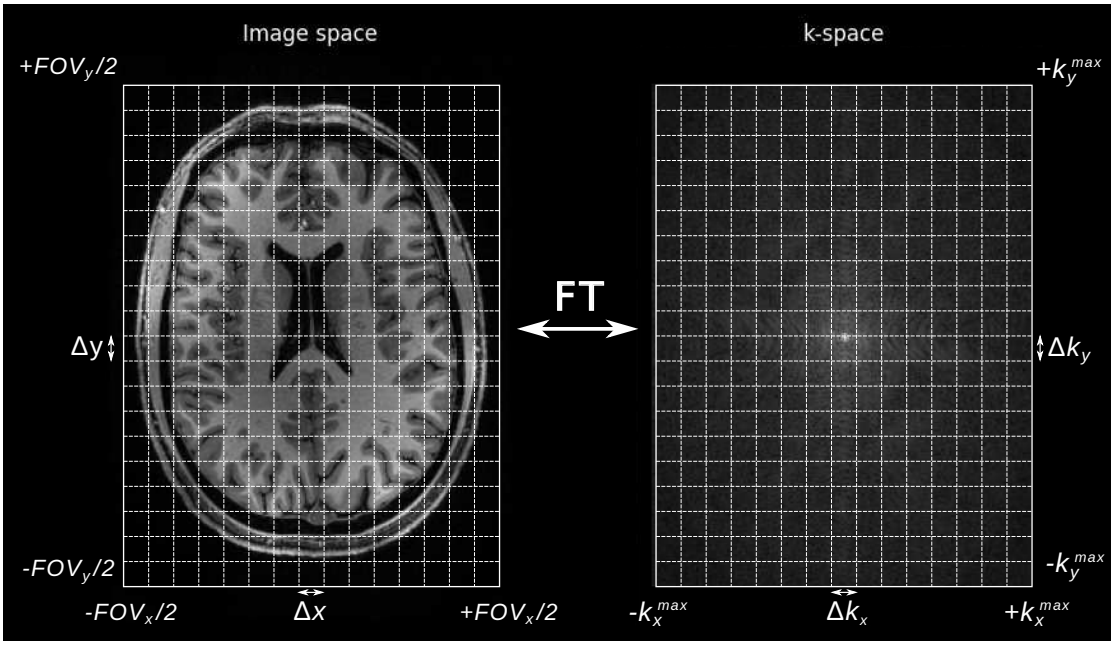

Figure 2.1: Image space and k-space are connected via a (inverse) Fourier Transform. The resolution defined by the voxel size Δx is inversely proportional to the maximum k-space position and the field of view (FOV) is inversely proportional to the sampling distance Δk. If the FOV is chosen too small, i.e. the sampling distance is too large, aliasing artifacts can occur.

2.1.3 Basic MRI Pulse Sequences

Two important classes of MRI pulse sequences are gradient echo (GRE) and spin echo (SE) sequences [14]. The basic two concepts are briefly explained as both gradient and spin echo sequences are used throughout this thesis. In the following, instead of the three 'physical' gradient axes G_x,G_y,G_z, 'logical' gradient axes G_r, G_p, G_s are used, the 'readout', 'phase' and 'slice' axes. These logical axes allow the description of pulse sequences regardless of the orientation of the acquired images.

2.1.3.1 Gradient Echo Sequence

The basic 2D gradient echo sequence (Figure 2.2) starts with an RF pulse with flip angle α, that is typically not larger than 90°. The RF pulse is accompanied by a slice selection gradient on the slice axis with the corresponding amplitude to excite a slice of the desired thickness according to equation 2.10. After the slice selection gradient a slice rewinder gradient is applied on the same axis. This rewinder has half the gradient moment of the slice selection gradient with opposite polarity and reverses dephasing of the spins in slice direction due to the slice selection gradient.

At the same time of the rewinder, a phase encoding gradient on the phase axis and a prephaser gradient on the readout axis are used to reach the k-space position $(-k_r^{\max}, -k_p)$. The subsequent readout gradient on the readout axis has twice the moment of the prephaser with opposite polarity, such that at the end of this gradient the k-space position $(k_r^{\max}, -k_p)$ is reached. During the readout gradient, the signal of this k-space line is acquired. In the middle of the readout gradient, the spins are completely rephased in readout direction, leading to a gradient echo. The time from the middle of the excitation pulse to the echo is referred to as the echo time *TE*. After the readout gradient, the phase encoding gradient is repeated with opposite polarity and a spoiler gradient is applied on the slice axis to dephase any remaining transverse magnetization. This basic sequence building block is the sequence kernel and it is repeated with varying phase encoding gradient amplitude to acquire all lines of the 2D k-space from $-k_p^{\max}$ to $k_p^{\max}$. It is important that the net gradient moment is the same in each repetition to avoid undesired echoes in subsequent k-space lines. The time between successive excitation pulses is denoted as the repetition time *TR*. Both *TE* and *TR*, as well as the flip angle of the RF pulse are important parameters for the contrast of the image as they define how the longitudinal and transverse magnetization evolve during the sequence.

The kernel is additionally repeated with different frequency offsets of the RF pulse to acquire the desired number of slices. The line-by line acquisition of k-space is robust against gradient imperfections, but takes a long time, because excitation has to be repeated for every phase encoding step and every slice. Therefore, often some sort of acceleration is used, e.g. by acquiring multiple k-space lines or slices with one excitation or using parallel imaging techniques. This is explained in more detail in section 2.4.

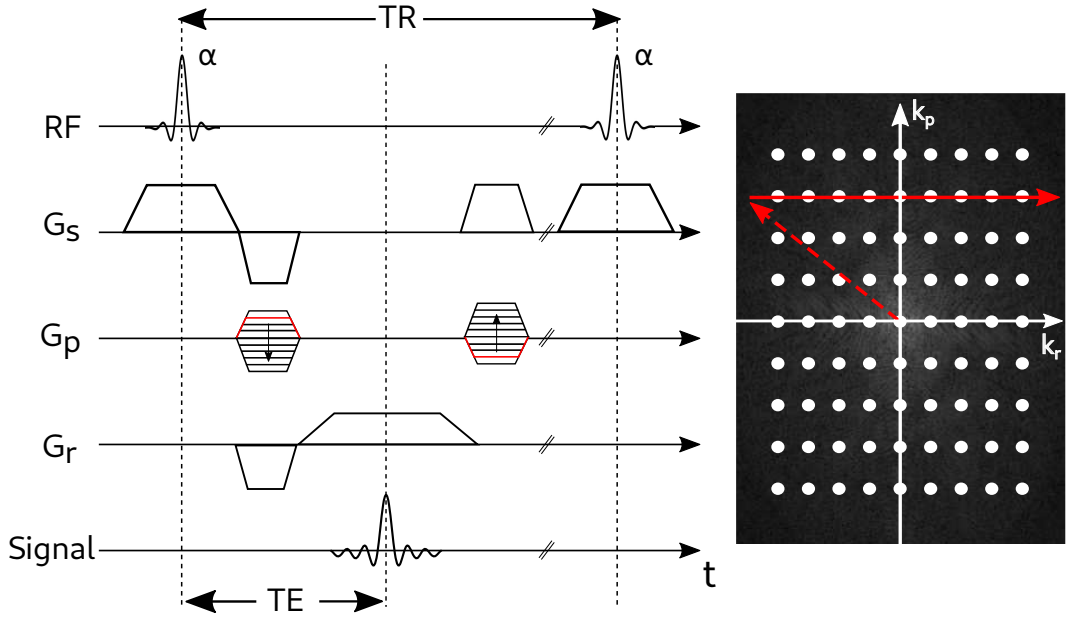

Figure 2.2: Gradient echo sequence timing diagram with RF, gradient and signal axes. The acquisition of one k-space line selected by the phase encoding gradient is illustrated on the right.

2.1.3.2 Spin Echo Sequence

In a spin echo sequence (Figure 2.3), a second 'refocusing' RF pulse with flip angle β is added after the excitation RF pulse. The refocusing pulse flips the dephasing spins to the opposite side of the transverse plane such that they rephase and form a spin echo. The echo time in the spin echo sequence is twice the time between the center of the two pulses. In the spin echo signal, dephasing from static field effects is refocused leading to a partial recovery of the FID signal. These static effects are T_2^* relaxation and inhomogeneities of the main magnetic field. Dephasing due to time dependent local field distortions experienced by moving spins as well as random field changes corresponding to T_2 relaxation are not refocused. The spin echo mechanism was first described by Hahn in 1950 [15].

The spin-warp acquisition of k-space in the spin echo sequence is similar to that in the gradient echo sequence. In order to acquire k-space lines in the same order as in the gradient echo sequence, the polarity of the prephaser on the readout axis and of the phase encoding gradient have to be inverted, if they are applied before the refocusing pulse. That is, because after the refocusing pulse, the k-space position is reflected around k-space center. The readout gradient and the acquisition window are typically centered around the echo time TE.

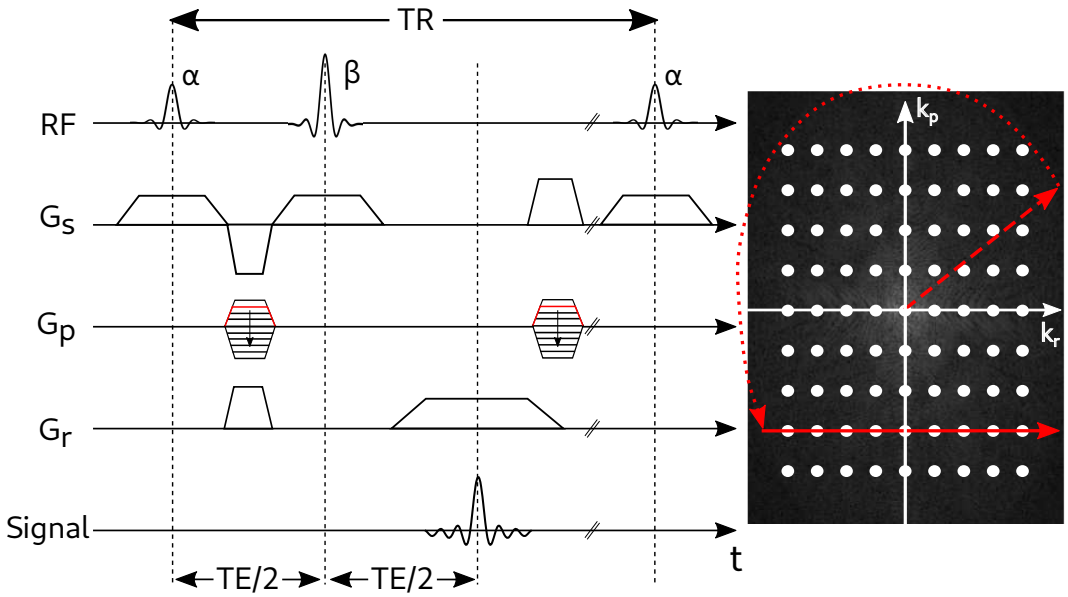

Figure 2.3: Spin echo sequence timing diagram with RF, gradient and signal axes. The acquisition of one k-space line selected by the phase encoding gradient is illustrated on the right. After the refocusing pulse, the k-space position is flipped around the k-space center.

2.2 Diffusion-weighted MRI

This section focuses on how the diffusion process of water molecules in human tissue can be used as a contrast mechanism in MRI. Diffusion-weighted MRI (DWI) allows to probe the microstructure of human tissue indirectly by quantifying the diffusive motion of water molecules. The voxel size of MR images is typically on the order of 1-5 mm^3, while the biological structures in human tissue are on a micrometer scale and can therefore not directly be assessed. However, diffusing water molecules move on a micrometer scale during typical time intervals of an MRI sequence (1-100 ms). As the diffusive motion is hindered or restricted by cell boundaries, tissue structure can be investigated by quantifying diffusion anisotropy. The most investigated tissue compartment in brain diffusion MRI is white matter, where the diffusion process is highly anisotropic due to the presence of myelinated axons.

In this section, the principles of the diffusion process are explained, followed by a description of the Stejskal-Tanner sequence, which is a common way to sensitize the MRI signal to the diffusion process. The section concludes with a brief overview of quantifying microstructure with diffusion MRI.

2.2.1 Principles of Diffusion and DWI

The diffusive motion of water molecules in the human body is caused by random thermal motion. A one-dimensional diffusion process can be described by Fick's second law [16]:

$$\frac{\partial c(x,t)}{\partial t} = D\frac{\partial^2 c(x,t)}{\partial x^2}, \tag{2.21}$$

where $c(x,t)$ is the concentration of water molecules at position x and time t and D is the diffusion coefficient. The solution of the diffusion equation in the case of free diffusion is a Gaussian distribution

$$c(x,t) = \frac{1}{\sqrt{4\pi Dt}} \exp\left(-\frac{x^2}{4Dt}\right). \tag{2.22}$$

The MRI signal can be sensitized to the diffusive motion by applying magnetic field gradients. Any diffusive motion during and between the application of gradients leads to a loss of phase coherence of moving spins, which results in a signal attenuation. The effect of molecular diffusion on the MRI signal can be described by the Bloch-Torrey equation [17], which is an extension of the Bloch equation (eq. 2.5) to include the diffusion process:

$$\frac{\partial \boldsymbol{M}}{\partial t} = \gamma \boldsymbol{M} \times \boldsymbol{B} - \frac{M_z - M_0}{T_1}\boldsymbol{e}_z - \frac{M_x \boldsymbol{e}_x + M_y \boldsymbol{e}_y}{T_2} + D\nabla^2 \boldsymbol{M}, \tag{2.23}$$

A solution of the Bloch-Torrey equation in the case of free (Gaussian) diffusion is

$$\begin{aligned} M_{xy}(t,\boldsymbol{r}) =& M_{xy}^{\text{Bloch}} \exp\left(-\boldsymbol{D}\gamma^2 \int_0^t \left[\int_0^{t'} \boldsymbol{G}(t'')\mathrm{d}t''\right]^2 \mathrm{d}t'\right) \\ =& M_{xy}^{\text{Bloch}} \exp\left(-\boldsymbol{B}:\boldsymbol{D}\right) = M_{xy}^{\text{Bloch}} \exp\left(-\sum_i \sum_j B_{ij} D_{ij}\right) \end{aligned} \tag{2.24}$$

where M_{xy}^{Bloch} is the solution of the Bloch equation (eq. 2.12), $\boldsymbol{G}$ is the effective gradient vector considering phase-reversal from refocusing RF pulses, $\boldsymbol{B}$ is the B-tensor, $\boldsymbol{D}$ is the diffusion tensor and $\boldsymbol{B}:\boldsymbol{D}$ is the scalar product of the two tensors. The B-tensor and the diffusion tensor are symmetric 3×3 matrices, that describe the diffusion weighting of the MRI sequence and the diffusive motion in all three dimensions, respectively [18]. The trace of the B-tensor is called the b-value, a scalar that represents the overall diffusion weighting due to the gradients in the MRI sequence. The trace of the diffusion tensor is the apparent diffusion coefficient (ADC). The term 'apparent' considers that the diffusion coefficient is averaged over multiple different tissue compartments in a voxel, which might have different diffusion coefficients, and that water diffusion in human cells is restricted, e.g. by cell membranes.

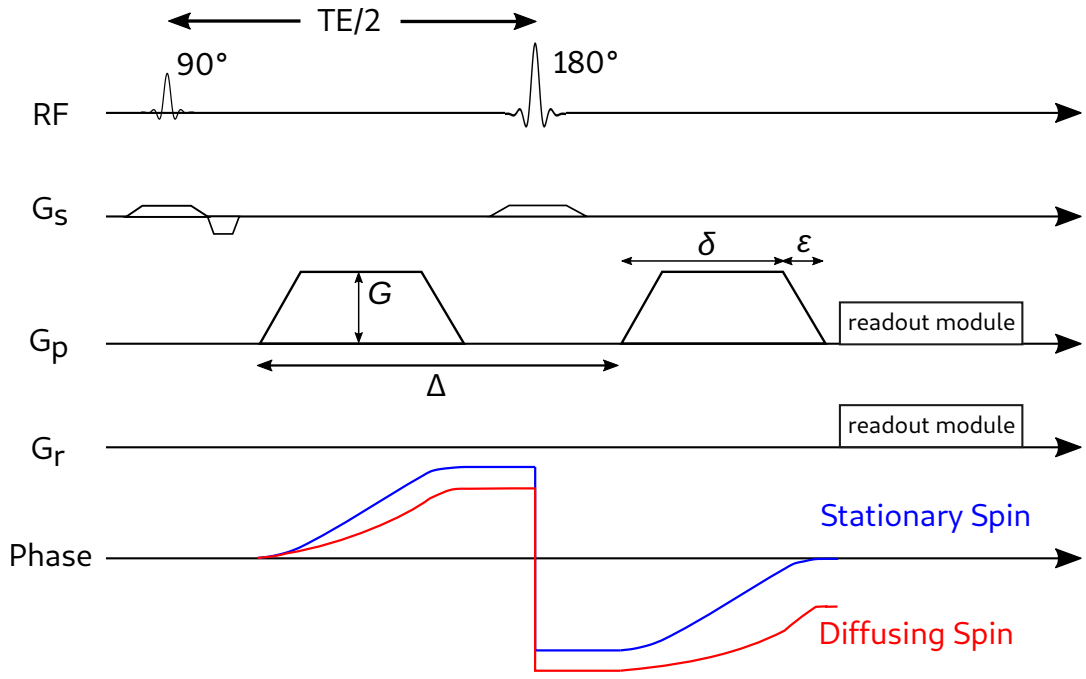

Figure 2.4: Illustration of the single pulsed gradient spin echo sequence. The sequence consists of a 90 ° RF pulse, a pair of two monopolar diffusion sensitizing gradients and a 180 ° refocusing pulse. The diffusion sensitizing gradients are applied along the phase axis. For stationary spins the accumulated phase from the first diffusion gradient is reversed by the second diffusion gradient, while diffusing spins experience dephasing, which leads to phase dispersion and signal cancellation inside a voxel.

The signal attenuation due to free diffusion is described by

$$S = S_0 e^{-\boldsymbol{B}:\boldsymbol{D}}, \tag{2.25}$$

where S_0 is the signal without diffusion weighting (zero b-value). According to equation 2.24, each gradient in an MRI sequence is contributing to the diffusion weighting of the signal. In practice, specific gradients with large amplitudes and duration are used as diffusion sensitizing gradients and the contribution of imaging gradients can be neglected at sufficiently high b-values. The signal S_0 is then the signal without the application of any diffusion sensitizing gradients.

2.2.2 Stejskal-Tanner Sequence

Diffusion-weighted encoding can be realized with the pulsed gradient spin echo technique (PGSE) developed by Stejskal and Tanner in 1965 [1]. In the PGSE sequence (Figure 2.4) a pair of two monopolar gradient pulses is applied before and after the 180° refocusing pulse of a spin echo sequence. The gradient pulses are applied along the same axis and have the same amplitude and duration. Stationary spins are not affected by these gradients, as the phase evolution of the spins due to the first gradient is refocused by the

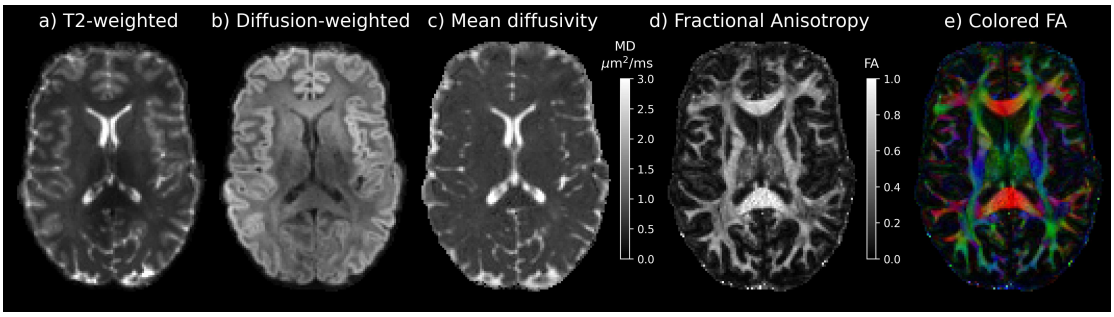

Figure 2.5: Raw T_2-weighted and diffusion-weighted images ($b = 1000\,\mathrm{s/mm^2}$) are shown in a) and b). Diffusion-weighted images were obtained for 30 diffusion directions. The resulting mean diffusivity (MD) and fractional anisotropy (FA) maps are displayed in (c) and (d). The FA map is color-coded in e) to show the principal diffusion direction (red=left-right, green=anterior-posterior, blue=inferior-superior).

second gradient after the 180° pulse. This refocusing is incomplete for diffusing spins, as they are exposed to a different magnetic field during the second diffusion gradient. This leads to phase dispersion inside a voxel and results in signal reduction dependent on the diffusion coefficient (Figure 2.4). While any gradients without a net moment, $\int_0^{TE} G(t')\mathrm{d}t' = 0$, can be used as diffusion gradients, a pair of two trapezoidal gradients is the most time-efficient choice to realize a certain b-value. The b-value of the PGSE sequence with two trapezoidal gradients with amplitude G, duration δ and ramp time ϵ on one axis is given by:

$$b = \gamma^2 G^2 \left[\delta^2(\Delta - \delta/3) + \epsilon^3/30 - \delta\epsilon^2/6\right], \tag{2.26}$$

where Δ is the time between the center of the two gradients – the diffusion time.

The signal in the PGSE sequence is acquired with a readout module, that typically samples 2D k-space data along a single-shot k-space trajectory. Single-shot trajectories are more time-efficient and motion-insensitive than multi-shot trajectories as the whole 2D slice is encoded in one shot and the diffusion preparation is only applied once. However, they are also more sensitive to static and dynamic field imperfections and suffer from T_2^* decay. Single-shot echo planar imaging (EPI) and spiral trajectories will be discussed in section 2.4. Multi-shot and 3D acquisition schemes have been proposed for high resolution diffusion imaging [19]–[22], but require longer scan times and need to be corrected for motion-induced phase inconsistencies between shots [23], [24].

2.2.3 Quantification of Microstructure

The diffusion-weighted signal provides an indirect measure of the properties of tissue microstructure. Properties of interest include, among many others, the size, orientation and characteristic length scales of pore microstructure or the volume fraction of different tissue compartments.

Different approaches for the quantification of microstructure can be divided into

signal representations and tissue or biophysical models [25]. Signal representations are mathematical functions that approximate the signal attenuation due to the diffusion process without making any assumptions about the underlying microstructure, while models try to increase specificity to the microstructure by taking into account only relevant biophysical parameters to explain the diffusion-weighted signal [25].

One of the most widely used signal representations is the characterization of the diffusion signal with the diffusion tensor. The diagonal elements of the diffusion tensor can be determined from equation 2.25 by acquiring three images with diffusion gradients in three different orthogonal directions and one image without diffusion-weighting. These three images can be combined by taking the geometric mean resulting in an image that is weighted by the trace of the diffusion tensor:

$$S_{\text{trace}} = \sqrt[3]{S_{xx}S_{yy}S_{zz}} = S_0 e^{-b(D_{xx}+D_{yy}+D_{zz}/3)} = S_0 e^{-b\text{ADC}}. \tag{2.27}$$

The average of the trace is typically referred to as the ADC or the mean diffusivity (MD). The whole diffusion tensor can be obtained, if the diffusion-weighted signal is measured along a minimum of six non-colinear directions, which is the number of unique elements of the tensor. This is the concept of Diffusion Tensor Imaging (DTI) [18]. Usually more than six directions are acquired to increase the accuracy of the tensor estimation by linear least squares fitting of equation 2.25. The diffusion tensor can be transformed to a frame of reference, in which the off-diagonal elements disappear. This frame is spanned by the three eigenvectors of the tensor. Together with the corresponding eigenvalues, the tensor can be represented by an ellipsoid.

As the diffusion tensor is rotationally invariant, the mean diffusivity can be calculated as the average of the eigenvalues of the diffusion tensor:

$$MD = \frac{1}{3}(\lambda_1 + \lambda_2 + \lambda_3). \tag{2.28}$$

Defining $\lambda_1 \geq \lambda_2 \geq \lambda_3$, the axial diffusivity ($D_{||} = \lambda_1$) is a measure for the diffusive motion along the principal diffusion direction and the radial diffusivity ($D_{\perp} = \sqrt{\lambda_2^2 + \lambda_3^2}$) corresponds to the magnitude of diffusive motion in the orthogonal direction.

The fractional anisotropy (FA) is a measure of diffusion asymmetry inside a voxel. The FA is defined as

$$FA = \sqrt{\frac{3}{2}\frac{(\lambda_1 - \text{MD})^2 + (\lambda_2 - \text{MD})^2 + (\lambda_3 - \text{MD})^2}{\lambda_1^2 + \lambda_2^2 + \lambda_3^2}}, \tag{2.29}$$

Fractional anisotropy and mean diffusivity maps obtained from a scan with 30 diffusion directions at a b-value of $b = 1000\,\text{s/mm}^2$ are shown in Figure 2.5. The fractional anisotropy can be color-coded to show the principal diffusion direction by modulating the FA with the directional cosines of the principal eigenvector (Figure 2.5 e).

The principal diffusion directions obtained from DTI can also be used for fiber track-

ing [26], which is a method to estimate the trajectories of white matter fiber bundles in the brain. Fiber tracking is based on the assumption that the principal diffusion direction is parallel to the main fiber orientation in white matter. This points to a major limitation of DTI, which can not resolve different fiber populations in a voxel, if they are crossing, kissing or bending. Additionally, at b-values much higher than $b = 1000\,\mathrm{s/mm^2}$, the signal attenuation is not well described by the diffusion tensor anymore, as restricted non-Gaussian diffusion becomes more important.

Several advanced concepts have been proposed to account for different fiber orientations inside a voxel. Diffusion Kurtosis Imaging (DKI) extends equation 2.25 by a kurtosis tensor, which is a metric for the deviation of the diffusion process from a Gaussian distribution [27]. DKI requires at least two non-zero b-values and 15 diffusion directions. Double or multidimensional diffusion encoding has been proposed to disentangle compartment sizes and shapes from their orientation distribution in a voxel by adding a second (or third) pair of diffusion gradients to the PGSE sequence [28]–[30]. Lastly, specific biophysical models have been used to assign the diffusion signal to specific tissue compartments, e.g. by modelling white matter tissue as a composition of small axons represented by sticks and the extra-axonal space [31]. These and several more advanced signal representation and modelling concepts are explained in more detail in chapter 22 of Ref. [32].

2.3 Field Imperfections

In this section, deviations from the main magnetic field B_0, their impact on image encoding and their measurement are discussed. These deviations can be classified into static field deviations, which arise mainly due to susceptibility effects and are independent of the MRI sequence, and dynamic field deviations, mainly caused by eddy currents due to the magnetic field gradients. Additionally, inhomogeneities of the transmit B_1 field and parallel transmit techniques are briefly discussed.

2.3.1 Static Field Imperfections

Image encoding in MRI relies on a homogeneous background magnetic field B_0 in the imaged volume of interest. For a commercial MRI scanner, the deviations from the specified magnetic field are typically smaller than one part per million. However, different magnetic susceptibility of the components of an object placed inside the scanner bore leads to a spatially varying magnetic field in the object. In the human brain, the largest deviations of the magnetic field arise at the interfaces of air and tissue, e.g. at the paranasal sinuses. Local deviations from the specified magnetic field lead to spatially varying precessional frequencies $\Delta\omega(\boldsymbol{r})$ (off-resonances). Another source of off-resonance effects is the chemical shift especially in fat tissue: The resonance frequency of protons in fat molecules is reduced compared to that in water by about 3.5 ppm because protons in

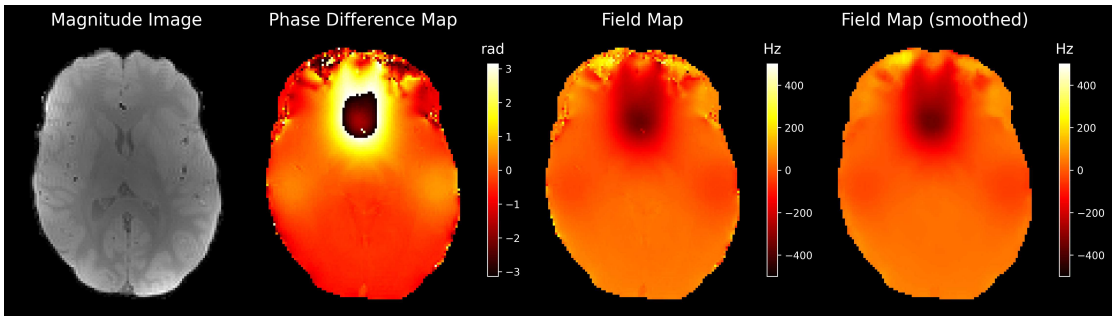

Figure 2.6: One slice of a static field map obtained from a dual-echo gradient echo sequence at a 7T scanner. The phase difference map, calculated from the phase images of the two echoes, contains phase wraps especially in the frontal part of the brain. The phase difference map was spatially unwrapped and a field map was calculated using the echo time difference ΔTE. Voxels containing only noise were masked with a brain mask calculated from the magnitude image of the first echo shown on the left. In the last step, outliers were removed with a despiking filter and the field map was smoothed with a Gaussian filter ($\sigma = 0.5$).

fat are more strongly shielded from the external magnetic field by surrounding electrons.

The signal equation 2.13 can be extended by including the spatial off-resonance distribution:

$$S(t) = \int_V \rho(\boldsymbol{r}) e^{-i\boldsymbol{k}(t)\boldsymbol{r}} e^{-i\Delta\omega(\boldsymbol{r})t} \mathrm{d}\boldsymbol{r}. \tag{2.30}$$

The off-resonance term distorts image encoding with magnetic field gradients, as the signal phase depends not only on the k-space trajectory anymore. This leads to different artifacts in the reconstructed images, which are dependent on the magnitude of the field deviations, the acquisition strategy, k-space trajectory and the sequence parameters. Typical artifacts are geometric distortions, reduced effective resolution (blurring) and signal loss due to intravoxel dephasing [33]. Signal loss is especially challenging in GRE sequences, as dephasing due to off-resonances is not refocused. In 2D imaging, large off-resonances on the order of the RF pulse bandwidth can additionally lead to incomplete excitation and refocusing as well as bended slices. These artifacts are more severe at higher fields as the maximum field deviations are proportional to the strength of the background field [34].

Strategies for reduction of artifacts include prospective field homogenization (shimming), and retrospective corrections. Shimming is typically done with specific shim coils, which can produce spherical harmonic fields of up to second or third spatial order. The shim fields are adjusted to counteract the field inhomogeneity, but the limited spatial order is not sufficient to completely homogenize the field. Different strategies for retrospective off-resonance correction exist, which are applied in k-space or image space and during image reconstruction or postprocessing. These strategies will be discussed in section 2.5.3.

2.3.2 Static Field Mapping

Both prospective shimming and retrospective off-resonance correction require accurate mapping of local deviations from the precessional frequency ('B_0 mapping'). This is done in a calibration prescan before the actual imaging scan is performed. The most common approach to B_0 mapping is the dual-echo gradient echo method, where two gradient echo images are acquired at different echo times. The phase evolution of the spins inside a voxel is a function of the local off-resonance:

$$\Delta\phi(\boldsymbol{r}) = \Delta\omega(\boldsymbol{r})\Delta TE, \tag{2.31}$$

where $\Delta\phi(\boldsymbol{r})$ is the phase difference between the two images and ΔTE is the echo time difference. The choice of the echo times impacts the accuracy of the field maps [35], [36]. Lower echo times lead to less T_2^* decay and therefore higher SNR especially in areas with large off-resonance, where T_2^* decay is stronger. A higher echo time difference increases the SNR in the phase difference measurement, as the accumulated phase difference is higher. The downside of a higher echo time difference is increased phase wrapping, especially in regions with large off-resonance. Spatial phase unwrapping [37] can recover the actual phase accrual, but might fail at very strong local gradients in the off-resonance map. Acquiring more than two echoes allows for voxel-wise temporal phase unwrapping [38], which can improve unwrapping in these areas. An example unwrapped field map obtained from a dual-echo gradient echo sequence is shown in Figure 2.6.

Another confounding factor for field mapping is the fat signal, that mixes with the water signal and disturbs the assumption of a linear phase evolution. A possible solution is to select echo times at which the (on-resonant) water and fat signals are in phase, which is dependent on the off-resonance frequency of fat. Another solution is to use fat suppression or water specific excitation in the GRE field mapping sequence [39].

B_0 field maps tend to become inaccurate, especially near air-tissue interfaces, where the GRE signal is low and large off-resonances occur. Therefore, voxels containing only noise or with low SNR are masked. As B_0 deviations in the brain are typically spatially smooth, applying spatial smoothing, as shown in Figure 2.6, can improve the field map. Global smoothing operations include Gaussian or median filters, while local smoothing removes spikes in the field maps [40]. Gaps in the field map can be filled by inter- and extrapolation.

Static B_0 field mapping can be compromised by subject motion, which is especially problematic for retrospective field correction, as the field maps geometrically do not fit the imaging data anymore. Additionally, the B_0 field can change significantly due to motion [41].

2.3.3 Dynamic Field Imperfections

Besides static field deviations, temporal changes of the magnetic field in the sample occur during the course of an MRI sequence. These dynamic field imperfections are mainly caused by eddy currents due to the magnetic field gradients. Eddy currents are induced in the conducting structures of the MRI scanner, e.g. the gradient coils, and generate a magnetic field that opposes the change of the original magnetic field [42]. The field generated by eddy currents is dependent on the gradient waveforms applied during the MRI sequence. Eddy currents can persist for several milliseconds after the gradient is switched off. Other sources of dynamic field imperfections are mechanical vibrations and bandwidth limitations of the gradient coils [43], thermal drift due to heating of the coils [44], timing delays between the gradients and the receive coil and head motion as well as physiological noise. Additionally, concomitant fields always accompany gradient fields as a direct consequence of the Maxwell equations. These fields increase with higher gradient amplitudes and decrease with higher main magnetic field strength [45].

Dynamic field imperfections distort the encoding fields, generated by magnetic field gradients, during image acquisition. As dynamic field imperfections originate mostly from structures outside the imaging volume, they are spatially smooth inside the volume [8]. The field components fulfill the Laplace equation, assuming there are no sources of dynamic fields inside the volume. In most MRI sequences, field deviations of zeroth and first spatial order are predominant, which correspond to global phase shifts and deviations from the ideal magnetic field gradients. Strong gradients, such as those used for diffusion-weighted imaging, can result in significant higher order field deviations.

Changes in the gradient time courses lead to deviations from the nominal k-space trajectory, resulting in shifted k-space sampling positions. In image reconstruction, the signal will be assigned to incorrect positions in k-space leading to different artifacts depending on the specific k-space trajectory. Adjusting the signal equation for zeroth and first order effects yields:

$$S(t) = \int_V \rho(\boldsymbol{r}) e^{-i[\boldsymbol{k}(t)+\Delta\boldsymbol{k}(t)]\boldsymbol{r}} e^{-i[\Delta\omega(\boldsymbol{r})t+\Delta\phi(t)]} \mathrm{d}\boldsymbol{r}, \tag{2.32}$$

where $\Delta\phi$ represents a global phase evolution and Δk deviations from the k-space trajectory due to field imperfections.

Shifts of the k-space trajectory caused by dynamic field imperfections lead to phase shifts in the signal, which in turn results in spatial shifts in image space. This manifests as ghosting, skewed and rotated images, or leads to blurring. Artifacts caused by dynamic field imperfections can often be corrected if the actual encoding fields are known. Correction might not be possible if field deviations are so large that essential k-space information is missing, e.g. when the Nyquist criterion is violated.

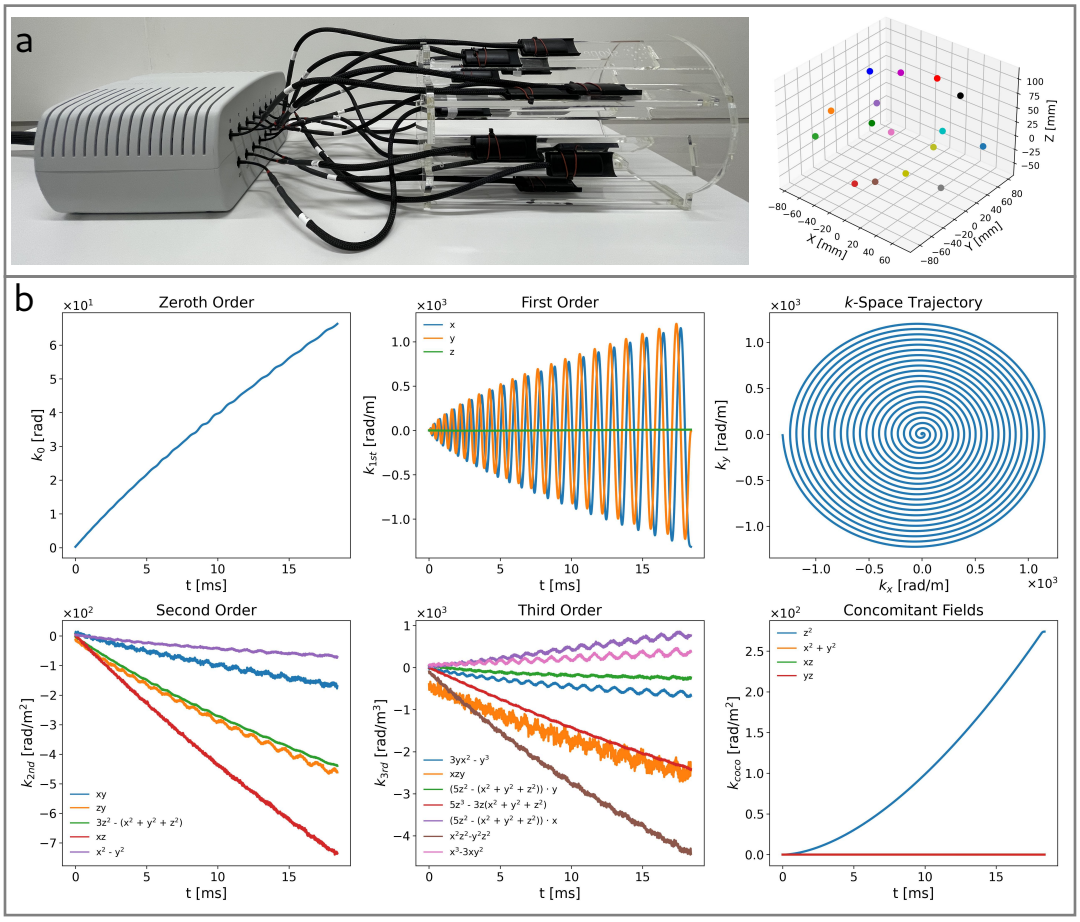

Figure 2.7: Spatiotemporal magnetic field monitoring with an NMR field probe system. a) Field probes mounted to a plastic frame with field probe positions relative to the gradient isocenter shown on the right. b) Example data from a field probe measurement of a spiral sequence. Field coefficients of up to third order are shown along with concomitant field coefficients of second order. At the top right of b), the two-dimensional k-space trajectory of the spiral sequence is plotted.

2.3.4 Spatiotemporal Magnetic Field Monitoring

Accurate measurement of the actual encoding fields with high temporal and sufficient spatial resolution is a prerequisite for correcting dynamic field imperfections. In this thesis, an approach based on small NMR field probes is used [8], [46]. The field probes consist of a small NMR-active sample that is surrounded by a solenoid coil for both transmission and reception. If the field probe is placed in a magnetic field at position $\boldsymbol{r}_p$ and the sample is excited by applying an RF pulse at the Larmor frequency of the sample, an FID signal can be measured by the surrounding coil. The phase evolution $\varphi(\boldsymbol{r}_p, t)$ of the FID signal is dependent on the amplitude of the magnetic field at the probe position:

$$\varphi(\boldsymbol{r}_p, t) = \gamma_p \left[\int_0^t B_d(\boldsymbol{r}_p, \tau) \mathrm{d}\tau + B_s(\boldsymbol{r}_p) t \right] + \varphi_0. \tag{2.33}$$

where γ_p is the gyromagnetic ratio of the probe sample, $B_d(\boldsymbol{r}_p, \tau)$ is the dynamic (temporally changing) component of the magnetic field amplitude, $B_s(\boldsymbol{r}_p)$ is the static component and φ_0 is the initial phase after excitation. The dynamic component can be extracted by taking the time derivative of the phase evolution if the static field component is known:

$$\frac{\mathrm{d}\varphi(\boldsymbol{r}_p, t)}{\mathrm{d}t} = \omega(\boldsymbol{r}_p) = \gamma B_d(\boldsymbol{r}_p) + \omega_s(\boldsymbol{r}_p). \tag{2.34}$$

where $\omega(\boldsymbol{r}_p)$ represents the angular frequency at the probe position and $\omega_s(\boldsymbol{r}_p)$ represents the angular frequency due to the static field component. The temporal resolution of this field measurement is limited only by the resolution of the spectrometer, which is typically on the order of microseconds.

Assuming a spatially smooth dynamic magnetic field in the imaging volume, it can be approximated by a small number N_L of basis functions $f_l(\boldsymbol{r})$ as

$$B_d(\boldsymbol{r}, t) = \sum_{l=1}^{N_L} c_l(t) f_l(\boldsymbol{r}), \tag{2.35}$$

with dynamic field coefficients $c_l(t)$. Defining the phase coefficients $k_l(t) = \gamma \int_0^t c_l(\tau)\mathrm{d}\tau$ with γ as the gyromagnetic ratio of the imaged object, the phase of the probe neglecting the initial phase yields

$$\varphi(\boldsymbol{r}_p, t) = \frac{\gamma_p}{\gamma} \sum_{l=1}^{N_L} k_l(t) f_l(\boldsymbol{r}_p) + \omega_s(\boldsymbol{r}_p) t \tag{2.36}$$

If the phase of a number N_P of field probes at different positions around the imaging volume is measured, equation 2.36 can be rewritten as a linear system of equations:

$$\boldsymbol{\varphi}(t) = \boldsymbol{P}\boldsymbol{k}(t) + \boldsymbol{\omega}_s t. \tag{2.37}$$

Here, $\boldsymbol{\varphi}(t)$, $\boldsymbol{k}(t)$ and $\boldsymbol{\omega}_s$ are vectors of length N_P. The probing matrix $\boldsymbol{P}$ has size $N_P \times N_L$ with elements $\boldsymbol{P}_{pl} = \frac{\gamma_p}{\gamma} f_l(\boldsymbol{r}_p)$. The phase coefficients $\boldsymbol{k}(t)$ can be estimated by measuring the phase evolution of each probe, subtracting the initial phase φ_0 and solving the linear system in equation 2.37 with a least squares approach using the pseudoinverse of the probing matrix:

$$\boldsymbol{k}(t) = (\boldsymbol{P}^{\mathrm{T}}\boldsymbol{P})^{-1}\boldsymbol{P}^{\mathrm{T}}\left[\boldsymbol{\varphi}_p(t) - \omega_s(\boldsymbol{r}_p)t\right]. \tag{2.38}$$

The number of field probes N_P should be at least equal to the number of basis functions N_L, and the field probes should be distributed evenly around the imaging volume within the linear range of the gradients to ensure good conditioning of the least squares fit. An optimized field probe placement is shown in Figure 2.7. Spherical harmonics are used as basis functions, as they fulfill the Laplace equation within a sphere and can approximate smooth fields effectively with a relatively low number of basis functions. They are also

Table 2.1: Real-valued spherical harmonics used as basis functions for field monitoring.

Spatial order	Spherical harmonic
0	1
1	x
1	y
1	t
2	xy
2	zy
2	$3z^2 - (x^2 + y^2 + z^2)$
2	xz
2	$x^2 - y^2$
3	$3yx^2 - y^3$
3	xzy
3	$(5z^2 - (x^2 + y^2 + z^2)) \cdot y$
3	$5z^3 - 3z(x^2 + y^2 + z^2)$
3	$(5z^2 - (x^2 + y^2 + z^2)) \cdot x$
3	$x^2z - y^2z$
3	$x^3 - 3xy^2$

commonly used for shimming purposes. The spherical harmonics of up to third spatial order are displayed in Table 2.1.

After determination of the field coefficients, the phase in the object can be estimated by

$$\varphi(\boldsymbol{r}, t) = \sum_{l=1}^{N_L} k_l(t) f_l(\boldsymbol{r}) + \omega_s(\boldsymbol{r}) t. \tag{2.39}$$

Expanding the phase up to first spatial order ignoring the static field yields $\varphi(\boldsymbol{r}, t) = k_0(t) + k_1(t)x + k_2(t)y + k_3(t)z$. Here $k_0(t)$ is a global phase evolution and $k_1(t) = k_x(t)$, $k_2(t) = k_y(t)$ and $k_3(t) = k_z(t)$ represent the k-space trajectory. Example phase coefficients for a spiral sequence are shown in Figure 2.7.

In order to fit the k-space coefficients, the field probe positions and the static field frequency ω_s are determined in a calibration prescan. The frequency ω_s is determined by unwrapping the phase of the FID signal and conducting a linear fit. In order to combine the dynamic phase model with a B_0 field map, the FID should be acquired with the same shim settings as the field map. The probe positions are determined by acquiring three FIDs with a constant gradient with known amplitude in all three dimensions and applying equation 2.36.

The NMR field probes used in this thesis contain a fluorine-based sample, instead of a water-based one [46]. Fluorine has a gyromagnetic ratio of $\gamma_{\mathrm{F}} = 40.08$ MHz/T, which is similar to that of protons and yields high NMR sensitivity. However, the Larmor frequencies are sufficiently different such that the fluorine sample is not excited by the transmit coil of the scanner allowing for simultaneous field monitoring and imaging. The field probe samples have a short T_1 to allow for fast re-excitation. Contrast agents are

used to achieve a low T_1 of $T_1 = 80\,\text{ms}$ while maintaining a sufficiently high T_2 of 50 ms ensuring accurate field measurements over a duration comparable to T_2.

2.3.5 Transmit Field Inhomogeneity

At high field strengths of 3 Tesla and above, inhomogeneity of the B_1 transmit field is observed in the human brain, which manifests as abnormally dark or bright areas in images. The cause of these inhomogeneities is partly attributed to destructive and constructive interference due to standing wave effects [47]. Spin-echo sequences with large flip angles such as the PGSE sequence are particularly sensitive to B_1 inhomogeneities as efficiency of the refocusing pulse is reduced. In the human brain, flip angles are typically higher than the nominal flip angle at the center, while being lower in the periphery. At a field strength of 7 Tesla, this typically leads to significant signal loss in the cerebellum.

Parallel transmission techniques (pTx) aim to mitigate B_1 inhomogeneities by employing multiple transmit channels distributed around the sample. These transmit channels can be controlled individually to create a B_1 field that counteracts the field inhomogeneities. The resulting B_1 field of a transmit array consisting of N_c transmit channels can be expressed by:

$$B_1(\boldsymbol{r}, t) = \sum_{i=1}^{N_c} p_i(t) S_i(\boldsymbol{r}), \tag{2.40}$$

where $p_i(t)$ is the pulse form applied on the respective transmit channel and $S_i(\boldsymbol{r})$ is the spatial sensitivity profile of that channel [10].

The most basic pTx implementation is to use the same pulse form for each channel and only apply a set of complex weights $w_i(\boldsymbol{r})$ to each channel, which is referred to as B_1 shimming or static pTx. Usually the deviation from a nominal flip angle distribution is minimized based on measured B_1 sensitivity profiles, accounting for hardware and SAR limits. Dynamic pTx is more flexible by optimizing the pulse form for each channel individually along with the respective transmit k-space trajectory defined by the gradients applied during the pulse. Dynamic pTx pulse design algorithms rely on simulations of the Bloch equation to obtain the rotation of the magnetization given a set of pulse forms and transmit coil sensitivities [10].

A requirement for the design of pTx pulses is an accurate measurement of the transmit field sensitivities, for which several spatial B_1 mapping techniques have been proposed [48]–[50]. Additionally, a B_0 map is required to account for off-resonances in pTx pulse design. Both B_0 and B_1 maps are subject-specific, therefore calibration measurements have to be repeated for each subject before the pTx pulses can be designed. Since B_1 and B_0 mapping are time-consuming and pTx pulse design algorithms are computationally demanding, the universal pulse (UP) design concept [51] has been proposed as a calibration-free pTx technique. The basic idea of UPs is to optimize the pTx pulses on a database of pre-acquired B_0 and B_1 instead of acquiring subject-specific maps in each scan session. This concept relies on the assumption that B_1 and B_0 maps are similar

up to certain degree for different subjects. For the human brain, initial results indicate that performance of UPs is similar to subject-specific pulses even for subjects not in the pulse design database [51].

2.4 Fast MRI Sequences for DWI

Quantification of brain microstructure with DWI requires acquisition of diffusion-weighted images at different b-values and with different diffusion directions covering the whole brain. Therefore, a high number of volumes has to be acquired in a reasonable amount of time. Additionally, the large diffusion gradients increase undesired sensitivity to bulk and physiological motion. Rapid imaging techniques are used in DWI to address these requirements.

Another important factor in DWI is image SNR, which is inherently low for DWI acquisitions at high b-values. The transverse magnetization of a spin-echo sequence at the echo time is given by [52]:

$$M\left(TE\right) = M_0 \left(1 - 2e^{-(TR-TE/2)/T_1} + e^{-TR/T_1}\right) e^{-TE/T_2}. \tag{2.41}$$

As TR is typically long in DWI sequences, the signal is mainly dependent on T_2. Therefore, the echo time TE should be minimized to maximize the SNR. This is especially important at ultra-high fields above 3 T as T_2 decreases at these field strengths [7]. Echo time reduction can be achieved by optimizing the readout module of the sequence or by improvement of the gradient hardware allowing higher gradient amplitudes and slew rates for the diffusion gradients [53].

2.4.1 Single-Shot EPI

Different image encoding strategies can be used for the readout module of the PGSE sequence (Figure 2.4). The most common strategy is a single-shot 2D EPI k-space trajectory, shown in Figure 2.8 (left) [54]. The EPI trajectory starts at one edge of the 2D k-space and all k-space lines are acquired by adding small phase-encoding gradients ('blips') between frequency-encoding gradients, which are reversed for subsequent lines. In this way, all k-space lines are acquired in one TR. The data is sampled on a Cartesian grid, but every second k-space line is acquired in reversed order.

The achievable echo time of an EPI readout, defined at the center of k-space, depends on the length of the EPI imaging train. The readout length of the EPI trajectory increases with higher resolution, larger FOV of the imaging plane and lower bandwidth in readout direction and can reach up to several tens of milliseconds. Parallel imaging (section 2.4.3) and Partial Fourier (PF) techniques allow to reduce the readout length and therefore the echo time. The PF technique uses the conjugate symmetry of k-space by acquiring only a fraction of the first half of k-space lines and filling the rest based on this symmetry (Figure 2.8 middle). As field imperfections and motion lead to phase

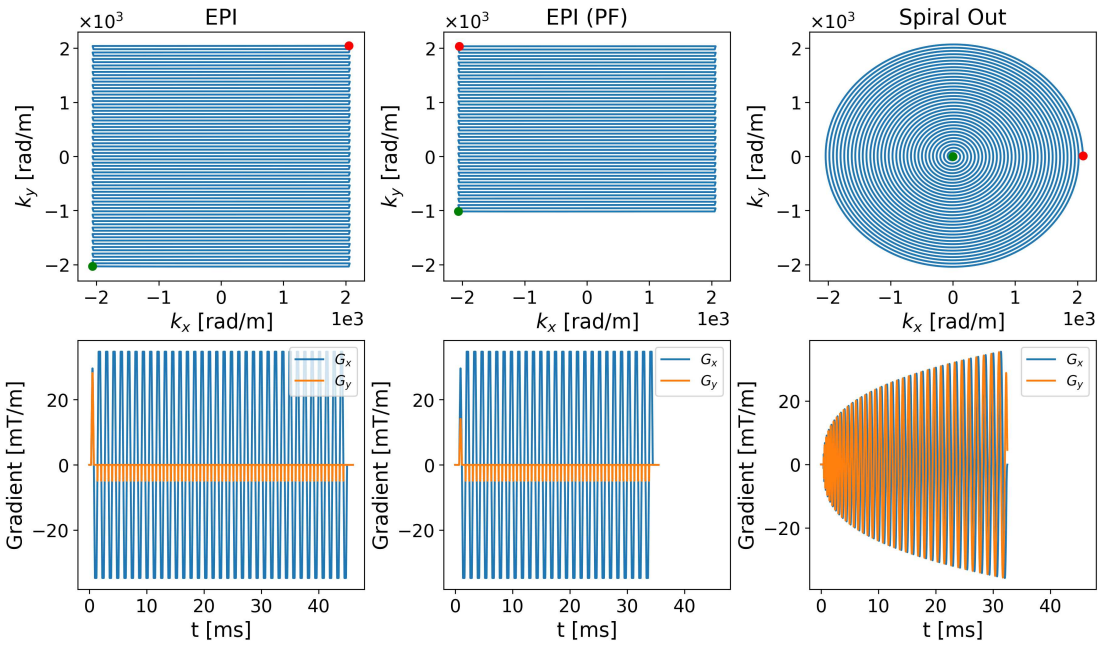

Figure 2.8: EPI and spiral k-space trajectories undersampled by an acceleration factor of $R = 2$. Left: EPI trajectory with corresponding readout und phase-encoding gradients. Middle: Same EPI trajectory accelerated with the Partial Fourier (PF) technique. Right: Spiral out trajectory with oscillating gradients. Beginning and end of the trajectories are marked with green and red dots.

errors in k-space, more than half of k-space has to be acquired to be able to correct for these phase errors.

Shifts of the EPI trajectory caused by dynamic field imperfections lead to a shift between the echo centers of subsequent phase encoding lines. This results in replicas of the image that are shifted by half the FOV in phase encoding direction, commonly referred to as N/2 or Nyquist ghosts, which are a common artifact in EPI. Static field inhomogeneities lead to geometric distortions mainly along the phase encoding direction as the bandwidth is significantly lower than in readout direction. Distortions are more severe for longer EPI readout trajectories.

2.4.2 Single-Shot Spiral

Spiral k-space trajectories represent an alternative to EPI trajectories. The spiral trajectory is generated by two oscillating frequency encoding gradients defining a spiral path through k-space as shown in Figure 2.8 (right) [55]. Spirals allow for faster sampling of k-space compared to EPI trajectories, as the gradient hardware is used more efficiently for spatial encoding. Therefore, the required readout length for acquiring images at the same resolution and FOV is usually shorter than for EPI trajectories. The velocity at which k-space is sampled is mainly limited the maximum gradient slew rate, as the gradient hardware has to be able to switch the gradients fast enough to follow the spiral path.

Spiral trajectories can vary in their starting points, with some beginning at the center (spiral out) and others at the periphery (spiral in) of k-space. The spiral out trajectory is particularly advantageous for DWI because it samples the k-space center early in the trajectory, thereby minimizing the echo time [6].

The single-shot spiral out k-space trajectory is sensitive to different artifacts than the EPI trajectory. The trajectory is susceptible to gradient imperfections, as the gradients constantly change during data acquisition. Therefore, accurate measurement of the actual k-space trajectories is important for image reconstruction. Distortions of the spiral k-space trajectory lead to rotated and shifted images, as well as blurring [56]. Static field imperfections and T_2^* decay can lead to image blurring, which is more severe for long readouts, as outer k-space is acquired at the end of the readout. Compared to EPI, spirals are less sensitive to motion artifacts due to the fast coverage of k-space and dense sampling of its k-space center.

As spiral trajectories sample the k-space on a non-Cartesian grid, special reconstruction techniques are needed, which are introduced in section 2.5.2.

2.4.3 Parallel Imaging

Parallel imaging is a widely used technique to accelerate the image acquisition by undersampling k-space and exploiting different spatial sensitivities of the RF receive coil array [57]: Instead of one volume coil, modern MRI scanners use an array of RF coils for signal detection, which consist of multiple overlapping coil elements that are placed around the imaging volume. The individual receive elements contain spatial information about the imaged object, as parts of the object close to the coil element contribute more to the signal. The image ρ_j reconstructed from the j-th receive channel is weighted by the spatial sensitivity profile c_j of the j-th coil element:

$$\rho_j(\boldsymbol{r}) = c_j(\boldsymbol{r})\rho(\boldsymbol{r}). \tag{2.42}$$

The spatial information and differences in coil sensitivities of the different receiver channels can be used to accelerate image acquisition. Acceleration is realized by undersampling of k-space, which refers to a higher sampling distance between k-space points than required for a given FOV according to the Nyquist criterion. In the EPI trajectory this is typically done by acquiring only every R-th phase-encoding line, where R is the acceleration factor. A single-shot spiral trajectory can be undersampled by designing a trajectory with R spiral arms and then omitting all but one during image acquisition. The achievable acceleration factor is typically much smaller than the number of coils, as non-ideal coil geometry and noise prohibit higher acceleration factors.

In order to avoid aliasing artifacts in the reconstructed images, the missing k-space information has to be recovered in image reconstruction, which is covered in section 2.4.3. Filling the missing k-space information requires mapping of the spatial coil sensitivities. Various methods have been proposed for the determination of coil sensitivity maps [58]–

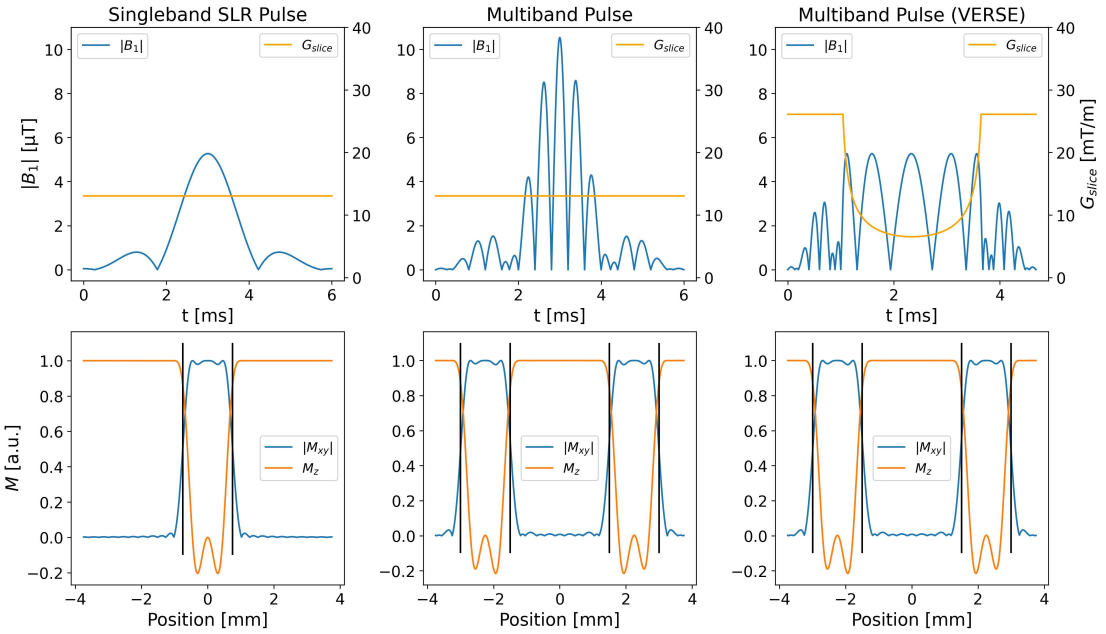

Figure 2.9: The top row shows singleband, multiband and minimum-time VERSE multiband 90° excitation pulses with the corresponding slice selection gradients for 1.5 mm slice thickness. The singleband RF shape was calculated with the SLR algorithm. For visualization purposes, the multiband pulses have only a small slice separation of 4.5 mm. The RF pulse duration of the minimum-time VERSE pulse is reduced, as the sidelobes of the pulse are compressed in time. The bottom row shows the corresponding longitudinal and transverse magnetization profiles along the slice direction. Vertical black lines indicate the nominal slice positions.

[60], which are typically obtained from a fully-sampled low-resolution calibration prescan.

2.4.4 Multiband Imaging

In-plane acceleration as presented in the previous section reduces the readout length and therefore reduces artifacts from field imperfections. However, the acquisition time of the PGSE sequence is dominated by the length of the diffusion gradients and the number of slices to be acquired. Considerable reduction of the acquisition time is therefore only possible by additional parallel imaging acceleration along the slice dimension. This requires excitation of multiple slices at once, which should be spatially separated as far as possible. Otherwise, the differences in coil sensitivities may be too small to disentangle the slices. Simultaneous excitation of multiple slices can be achieved by superimposing multiple slice-selective RF pulses with amplitude $A(t)$ and phase φ_j, each shifted by a frequency offset $\Delta\omega_j(z)$ that depends on the slice separation:

$$B_1^{\mathrm{MB}}(t) = A(t) \sum_{j=1}^{N} e^{i(\Delta\omega_j(z)t + \varphi_j)}. \tag{2.43}$$

This technique is called multiband (MB) or simultaneous multislice (SMS) imaging [61]. The resulting multiband pulse $B_1^{\mathrm{MB}}(t)$ is applied together with the same slice gradient as the initial singleband pulse. An example for singleband and multiband pulses along with their simulated slice profiles is shown in Figure 2.9.

If multiple slices are excited, k-space becomes three-dimensional rather than two-dimensional with the Nyquist criterion in slice direction being $\Delta k_z = 1/\mathrm{FOV}_z = 1/(N\Delta z)$ [62]. Here, the FOV in slice direction (FOV_z) is defined by the slice center-to-center distance Δz and the number of simultaneously excited slices N. If a single-shot 2D readout is used, the k-space in slice direction is undersampled by a factor of N. In order to achieve a more homogenous sampling of k-space, an additional gradient on the slice axis can be used during signal readout, which results in a better conditioning of the reconstruction problem. The initial singleband RF shapes for the excitation and refocusing pulses of the PGSE sequence are usually calculated with the Shinnar-Le Roux (SLR) algorithm [63], [64], which allows to derive the RF shape from the desired slice profile even at large flip angles. A detailed description of the SLR algorithm can be found in Ref. [63].

Peak amplitude and power deposition of multiband pulses is increased compared to singleband pulses, which can lead to a violation of the maximum allowed RF amplitude or the maximum specific absorption rate (SAR). One way to reduce both peak amplitude and SAR is to stretch the pulse in time. However, this makes the pulse more susceptible to off-resonance and relaxation effects and might result in a longer echo time. An alternative to stretching the whole pulse is to use variable stretching factors along the RF shape, a method known as variable-rate selective excitation (VERSE) [65]. Variable stretching factors allow to decrease peak amplitudes of the pulse, while amplifying the sidelobes. As SAR scales with the square of the pulse amplitude, the total SAR is reduced, while the duration of the pulse is kept short.

For a piece-wise constant RF pulse shape, the stretching factor $\alpha(k)$ for the k-th sample of duration Δt is defined as $\alpha(k) = \Delta t/t(k)$, where $t(k)$ is the dilated time-vector. The resulting VERSE pulse samples $b_1(k)$ and the corresponding slice gradient $g(k)$ are defined as:

$$b_1(k) = \alpha(k)B_1(k), \quad g(k) = \alpha(k)G \tag{2.44}$$

where G is a constant slice select gradient amplitude and $B_1(k)$ is the k-th sample of the original RF shape. The resulting RF and gradient pair, when resampled to a uniform time grid, excites the same slice profile as the original pair in the case of on-resonant spins. This is shown for the multiband pulse in Figure 2.9. However, VERSE pulses are more susceptible to off-resonance effects, as their bandwidth is decreased in areas with high amplitude of the original pulse.

The stretching factors can be calculated by different design strategies, such as minimum-SAR or minimum-time formulations [65]. The design of VERSE pulses is constrained by hardware limits, which are the maximum gradient strength, the maximum slew-rate and

the maximum RF amplitude. An iterative algorithm for the design of minimum-time VERSE pulses, that is used in this thesis can be found in [66].

2.5 Advanced Image Reconstruction

This section provides a brief introduction to advanced image reconstruction methods, including the reconstruction of undersampled data with parallel imaging, reconstruction of non-Cartesian data, and strategies for off-resonance correction during image reconstruction. The section concludes with a description of an expanded encoding model that incorporates higher order dynamic fields.

2.5.1 Parallel Imaging Reconstruction

One of the most commonly used methods for the reconstruction of undersampled MRI data is SENSitivity Encoding (SENSE) [59]. In SENSE, the signal of the j-th receive coil is modeled by including the coil sensitivity profile $c_j(\boldsymbol{r})$ in the signal equation:

$$S_j(t) = \int_V \rho(\boldsymbol{r}) c_j(\boldsymbol{r}) e^{-i\boldsymbol{k}(t)\boldsymbol{r}} \mathrm{d}\boldsymbol{r}. \tag{2.45}$$

The signal equation can be rewritten in matrix-vector form

$$\boldsymbol{s} = \boldsymbol{E}\boldsymbol{\rho}, \tag{2.46}$$

with the encoding matrix $\boldsymbol{E}_{j,m,n} = c_j(\boldsymbol{r}_n) e^{-i\boldsymbol{k}_m \boldsymbol{r}_n}$, where $\boldsymbol{k}_m$ is the m-th position in k-space and $\boldsymbol{r}_n$ is the position of the n-th voxel. As equation 2.46 represents a linear system of equations, the image $\boldsymbol{\rho}$ can be reconstructed by inverting the encoding matrix. The encoding matrix is of size $n_c n_k \times n_v$, where n_c is the number of coils, n_k the number of k-space samples and n_v the number of voxels. The encoding matrix is in general not a square matrix, as the number of coils is typically larger than the acceleration factor R. The linear system is therefore overdetermined and a least squares solution maximizing SNR is given by

$$\boldsymbol{\rho} = \left(\boldsymbol{E}^H \boldsymbol{E}\right)^{-1} \boldsymbol{E}^H \boldsymbol{s}, \tag{2.47}$$

where $\boldsymbol{E}^H$ is the conjugate transpose of the encoding matrix. This equation assumes uncorrelated noise in the receive coils. Decorrelation of the receive channels is described in [59].

As the encoding matrix is typically a large matrix, the inversion is numerically demanding. In the case of regular Cartesian undersampling, the number of aliased voxels is equal to the acceleration factor and individual voxels can be unfolded using the coil sensitivities after reconstruction of aliased images via FFT. In the general case of arbitrary k-space trajectories, aliasing is more complex and image reconstruction is typically done by iteratively solving equation 2.47 [67]. Iterative reconstruction relies on find-

ing the image that best fits the measured data after a limited number of iterations by minimizing the error norm $\|\boldsymbol{s} - \boldsymbol{E}\boldsymbol{\rho}\|_2^2$, starting from an initial guess ρ_0. One popular method is the conjugate gradient (CG) algorithm, which achieves good results after only a few iterations for moderate acceleration factors. The main computation steps in CG are multiplications of the matrices $\boldsymbol{E}$ and $\boldsymbol{E}^H$ with intermediate vectors, which can be efficiently done with FFT for faster calculation [67].

The SNR of images reconstructed with SENSE is reduced compared to fully sampled images:

$$SNR_{\text{acc}} = \frac{SNR_{\text{full}}}{\sqrt{R}g}. \tag{2.48}$$

The geometry factor g is dependent on the spatial arrangement of the coils and the acceleration factor.

2.5.2 Non-Cartesian Image Reconstruction

In non-Cartesian MRI, k-space data is sampled on a non-equidistant grid. Non-Cartesian sampling is present in every MRI acquisition as field imperfections and motion lead to deviations from nominal Cartesian k-space trajectories. Intentional non-Cartesian k-space sampling with radial or spiral trajectories is used to reduce echo times, sample k-space more efficiently or to improve motion insensitivity. Reconstruction of non-Cartesian data is more complex than reconstruction of Cartesian data, as the FFT is not directly applicable. The DFT in equation 2.17 can be generalized for non-equidistant sampling points, but it is much slower than FFT reconstruction due to the higher number of operations.

In order to still be able to make use of the FFT, the non-Cartesian data has to be interpolated onto a regular Cartesian grid. A widely used method for this interpolation is gridding [68], where the non-Cartesian data is convolved with a kernel function and sampled on a Cartesian grid. Typical kernel functions are a windowed sinc or a Kaiser-Bessel window [69]. Finite kernels, such as these, can lead to undesired effects such as aliasing and apodization, which manifests as a reduction of the signal at the edges of the FOV. Aliasing can be avoided by performing gridding on a denser Cartesian grid and then cropping the image afterwards. Deapodization can be achieved by dividing the image by the Fourier transform of the kernel function in image space.

Non-Cartesian k-space trajectories sample k-space non-uniformly. For example, radial and spiral trajectories sample the center of k-space more densely than the periphery. This leads to blurred images, when the gridding reconstruction is performed due to the non-uniform weighting of k-space points. To account for this, the k-space data is multiplied by a density compensation function, calculated from the k-space trajectory [70], before the gridding reconstuctiong.

Gridding can be combined with iterative parallel imaging reconstruction [67]. While density compensation and deapodization are not essential in iterative reconstruction, they can facilitate faster convergence.

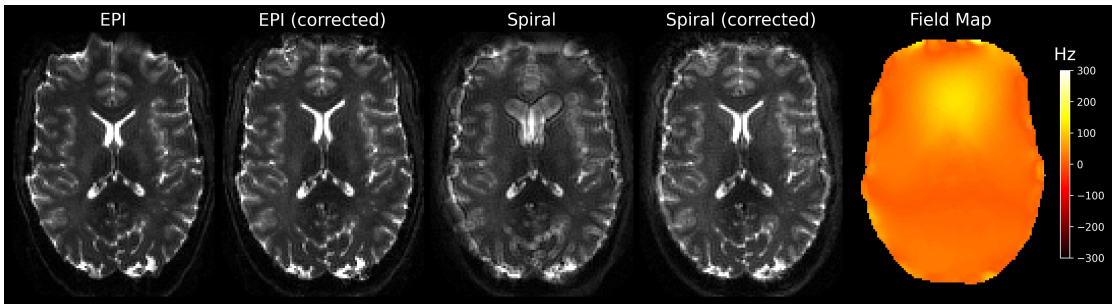

Figure 2.10: T_2-weighted images acquired with single-shot EPI and spiral trajectories are shown with and without off-resonance correction in the reconstruction. The corresponding B_0 field map is shown on the right. Off-resonance correction removes most off-resonance related artifacts. Remaining artifacts due to insufficient correction are visible especially in the frontal part of the brain.

2.5.3 Off-resonance Correction

Ignoring static field inhomogeneity in the image reconstruction can lead to severe artifacts in reconstructed images, especially when using long readouts. This is illustrated in Figure 2.10, where T_2-weighted images acquired with single-shot EPI and spiral trajectories are shown with and without correction for off-resonance. EPI images show dislocated voxels, while spiral images show considerable blurring especially in areas with large B_0 deviations. Equation 2.30 includes an off-resonance term in the signal equation. Following that equation, one approach for image reconstruction that accounts for spatially varying off-resonance is to demodulate the signal at each time point by the conjugate of the accrued phase [71], [72]:

$$\rho(\boldsymbol{r}) = \int_0^T S(t) e^{i\boldsymbol{k}(t)\boldsymbol{r}} e^{i\Delta\omega(\boldsymbol{r})t} \mathrm{d}t, \tag{2.49}$$

where T is the readout duration. This method is commonly referred to as conjugate phase (CP) reconstruction. Equation 2.49 does not represent a Fourier Transform anymore and the FFT can not be applied anymore. Instead the image has to be reconstructed for each voxel individually with the corresponding off-resonance frequency, which is computationally expensive.

Two different approximations to the CP reconstruction have been proposed, that remove the time dependency and the spatial dependency of the off-resonance term, respectively. One is the time-segmented CP reconstruction [73], which segments the total readout of duration T into L windows of width 2τ that are $\tau = T/L$ apart. For each window, the off-resonance phase contribution is assumed to be constant, which removes the time dependence of the off-resonance term. This allows for a standard FFT reconstruction for each time segment, followed by multiplying the resulting image by $e^{-i\Delta\omega(\boldsymbol{r})n\tau}$, where $n\tau$ is the center of the n-th time segment. The final image is obtained by summing up the images of all time segments. The k-space data of one window is usually weighted

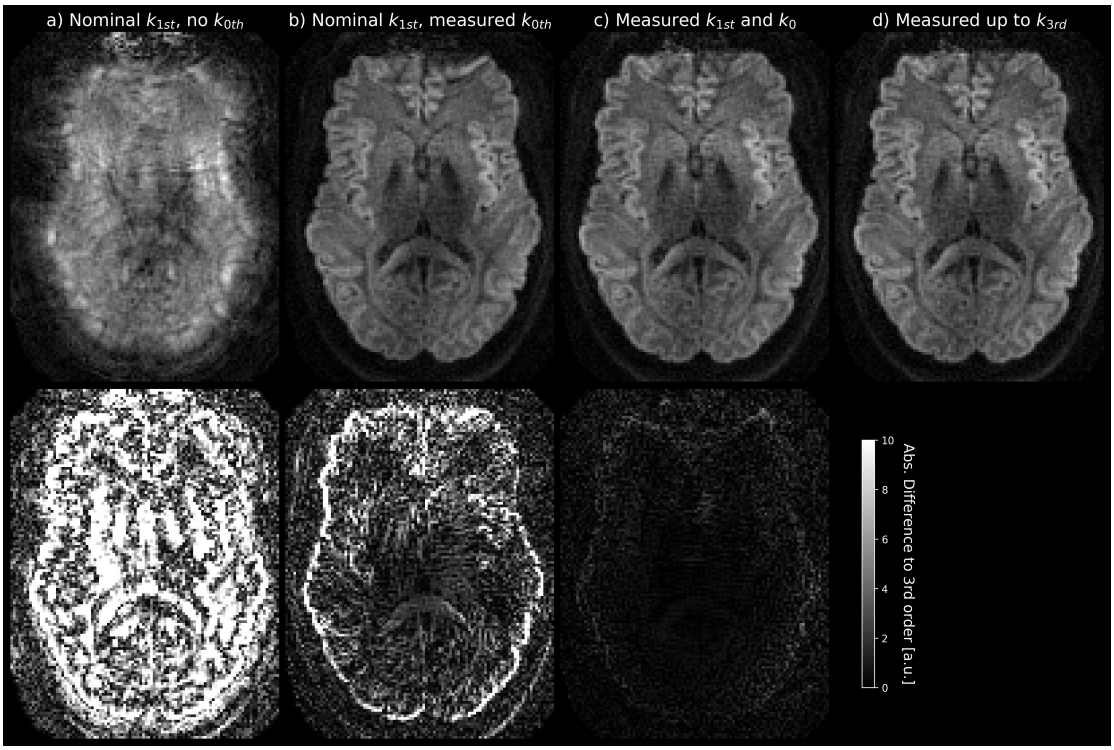

Figure 2.11: Diffusion-weighted images ($b = 1000\,\mathrm{s/mm^2}$) acquired with a single-shot spiral trajectory. The images are reconstructed with a) the nominal k-space trajectory and no correction of the global phase k_0, b) with measured k_0 and the nominal k-space trajectory, c) with measured k_0 and measured k-space trajectory, and d) with measured phase terms up to third spatial order. Note that in a) model based correction of the global phase via the vendors eddy current correction was disabled.

by a window function that accounts for the time distance between each k-space sample and the center of the window.

The other approximation is multifrequency interpolation [74], where L different images are reconstructed, each assuming a spatially independent offresonance term $e^{-i\Delta\omega_l t}$, where ω_l represents the l-th frequency. The signal is multiplied by the constant offresonance before applying the FFT, effectively demodulating the signal at different frequencies. This results in parts of the images being 'in focus' and other parts being 'out of focus'. The final image is reconstructed by interpolation of the L individual images accounting for the individual off-resonance frequency $\omega(\boldsymbol{r})$ of each voxel.

Both the time-segmented reconstruction and multifrequency interpolation are computationally more efficient than CP reconstruction but still require L times more operations than a standard FFT reconstruction. The choice of L depends on the range of off-resonance frequencies in the field map and can be reduced if the range is smaller.

2.5.4 Higher Order Image Reconstruction

The encoding matrix in equation 2.46 consists of the coil sensitivities and a phase term, which contains the k-space trajectory and describes the spatial encoding via magnetic

field gradients. Deviations from the nominal k-space trajectory can be accounted for in the encoding matrix by replacing the nominal with a measured trajectory obtained from field monitoring. However, during an MRI sequence, not only first order, but also zeroth and higher spatial order field deviations arise, which is especially the case when gradients of long duration and with high amplitudes are used. In order to include dynamic field deviations up to a certain spatial order in image reconstruction, the phase term in the encoding matrix can be expanded [9] with the phase coefficients obtained from field monitoring (equation 2.39):

$$\phi(\boldsymbol{r}, t) = \Delta\omega(\boldsymbol{r})t + \sum_{l=1}^{N_L} k_l(t) f_l(\boldsymbol{r}). \tag{2.50}$$

This already includes the correction for static field deviations $\Delta\omega(\boldsymbol{r})$ as described in the last section. The encoding matrix can be expressed as:

$$\boldsymbol{E}_{j,m,n} = c_j(\boldsymbol{r}_n) e^{-i\phi(\boldsymbol{r}_n, t_m)}. \tag{2.51}$$

If dynamic field coefficients of higher than first spatial order are included in the encoding matrix, Fourier Transforms can not be used for image reconstruction anymore due to the form of the phase term. Instead, iterative image reconstruction requires explicit matrix-vector multiplications, which makes it considerably slower than Fourier based algorithms [9].

Figure 2.11 shows diffusion-weighted images acquired with a single-shot spiral trajectory and reconstructed with different orders of dynamic field corrections. It can be seen that the image quality improves especially when correcting for zeroth and first order fields as these have a high impact on spatial encoding. Higher order corrections affect mostly the periphery of the FOV as the phase contributions increase with greater distance to the gradient's isocenter.

Chapter 3

Open-source MR Imaging and Reconstruction Workflow

Magnetic Resonance in Medicine, 2022;88;2395-2407

3.1 Introduction

Open science and open-source software tools are of increasing importance in today's MR research because the number of available open-source softwares has constantly grown over the years. The International Society for Magnetic Resonance in Medicine (ISMRM) website MR-Hub [75] and the website of the Open Source Imaging Initiative [76] currently list over 40 MRI-related open-source tools. Many of these tools are actively developed and contain state-of-the-art algorithms for MR imaging. Open-source imaging software and hardware readily helps many researchers to collaborate and improve their own research, as well as reproduce outcomes of published literature.

Recently, results from the first ISMRM reproducibility challenge targeting MR image reconstruction were published [77]. In this challenge, reconstruction results from conjugate gradient-SENSE implementations of different submissions were compared. It concluded that small variations in implementation details or input parameters can lead to significant differences in images, and that access to the original source code and data is indispensable for a reliable reproduction of research results. Well-maintained online resources consolidating open-source tools, such as opensourceimaging.org [76], are expected to play an increasingly important role in promoting reproducibility and sustainability of MR imaging studies.

Open-source software tools are available for many parts of the MR imaging process, including sequence development, data acquisition, image reconstruction, and image post-processing or analysis. In the case of development or modification of MRI sequences, the exact time course of RF pulses and gradients may be of high importance for reproducibility. However, publications typically do not contain the detailed fine-grained timing information of new sequences but only the general idea and high-level features. Sequence source code itself may also not be shareable for intellectual property or contractual reasons, and hardware and software versions may be incompatible.

The Pulseq [78] and TOPPE [79] file formats provide an open-source description of a complete pulse sequence's timing and waveforms defined in one file, which can be executed on scanners running different software versions and also from different vendors.

On the other end of the imaging pipeline, reconstruction of MR images is increasingly dependent on parameter choices as algorithms get more complicated and allow more tuning parameters. The results may depend on the specific implementation of a reconstruction algorithm, making comparisons between studies difficult. Novel reconstruction algorithms are often executed offline due to the difficulty of integrating them into the existing vendors' reconstruction frameworks. The Gadgetron [80] project addresses this problem by using an extensible image reconstruction framework based on streaming data pipelines that can be integrated into the existing reconstruction environment of the MRI scanner.

The diversity in input raw data such as format, ordering, and preprocessing further complicates the development of a generalizable pipeline. Therefore, widely used open-

source data formats, such as the MR Raw Data (MRD, originally ISMRMRD [81]) or the Neuroimaging Informatics Technology Initiative format [82] for image data, are crucial for standardizing data structures and sharing algorithms efficiently.

These openly available tools contribute toward improving reproducibility of published research results. However, there is currently no open-source workflow covering all aspects of the MR imaging process from sequence design to image reconstruction. For example, results may only be partly reproducible if specific raw datasets are needed to reproduce the results of an image reconstruction algorithm because the sequence may not be made available. The proposed workflow aims at combining different tools to form an open-source end-to-end imaging pipeline, which is completely shareable and can easily be extended by new tools. The pipeline covers MRI sequence development, data acquisition, image reconstruction, and postprocessing of images. MRI sequence development and data acquisition is based on the Pulseq framework, whereas the MRD format is used for storage of MR raw- and metadata. Acquired raw data are processed by a Python-based server. The data can be streamed to the reconstruction server either offline or online, for which the latter requires a vendor-dependent streaming interface. Reconstruction is done with the Berkeley Advanced Reconstruction Toolbox (BART) [83].

The pipeline was also integrated into the JEMRIS [84], [85] simulation framework by adding an interface to the image reconstruction pipeline to the framework. As a result, sequences designed and simulated in JEMRIS can be executed without modification on the MRI scanner, and simulated and acquired data can be reconstructed with the same pipeline.

The whole workflow is based on openly available tools, with the exception of the interfaces for on-scanner sequence execution and data streaming for online reconstruction. These interfaces are vendor-dependent and thus not entirely open-source. However, the streaming interface is optional because the image reconstruction pipeline can also be executed offline. The Pulseq interpreter sequence is also shared in the source code form within the respective vendor communities.

3.2 Methods

The open-source imaging workflow contains sequence design, data acquisition, image reconstruction, and optional postprocessing of images. An overview of the whole pipeline is shown in Figure 3.1.

3.2.1 Sequence Development

Sequence design can be done with the Pulseq framework using the MatLab (MathWorks, Natick, MA) implementation [86], the Python implementation PyPulseq [87] or JEMRIS. All tools generate Pulseq sequence files, which contain the complete timing for RF pulses, gradients, and ADC sampling points. Here, PyPulseq and JEMRIS are used because

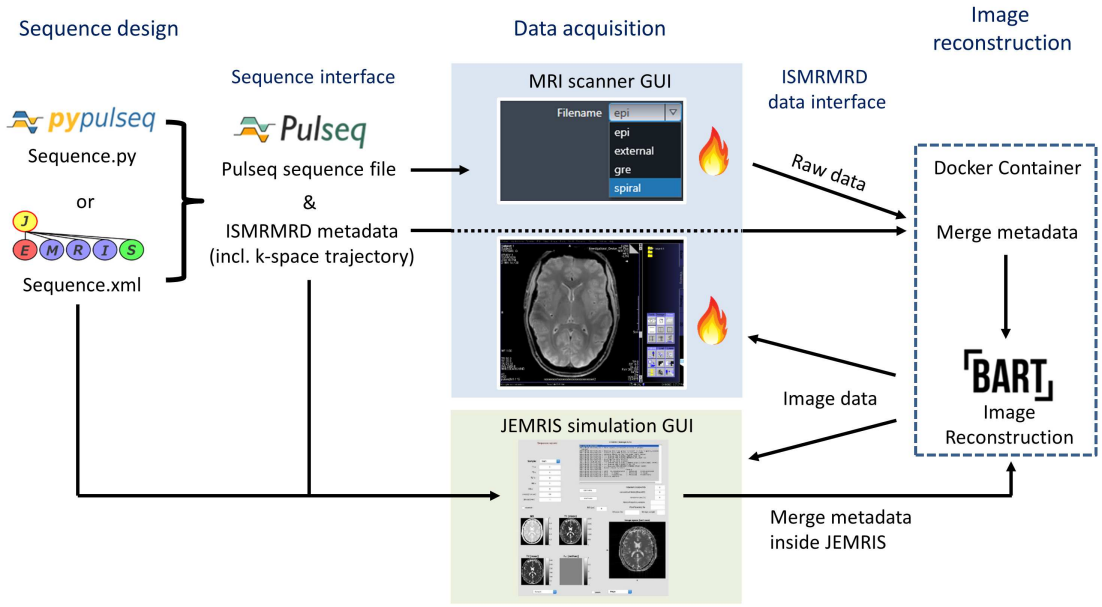

Figure 3.1: Overview of the whole workflow with data acquisition at an MRI scanner (light blue) or in JEMRIS simulations (light green). Pulseq sequence and MRD metadata files are created with either PyPulseq or JEMRIS. The sequence file is executed at the scanner using a vendor-specific interpreter. Raw data are sent to the reconstruction server via the FIRE interface, and the metadata from the MRD file are merged. Images are reconstructed with BART and sent back to the scanner via FIRE. In an offline reconstruction, the FIRE interface is replaced by an MRD converter and a Python-based client. Acquired data from JEMRIS simulations is merged with the metadata inside JEMRIS and saved in the MRD format. The same reconstruction pipeline as for data from an MRI scanner data is executed. BART, Berkeley Advanced Reconstruction Toolbox; FIRE, framework for image reconstruction environments; MRD, MR raw data.

neither depends on commercial software.

The Pulseq format currently has no support for transferring metadata and k-space information to the MRI scanner; it only contains the sequence timing. The vendor's raw data files that originate from the Pulseq sequence execution therefore contain only the acquired data with no information on k-space sampling. These raw data files do contain a header section, but only with dummy values. For this reason, an additional MRD metadata file is created together with the Pulseq sequence. This file contains all relevant information about the measurement and is merged with the raw data before image reconstruction.

For identification of the files, the Message-Digest Algorithm 5 (MD5) hash of the Pulseq sequence file is calculated and appended to both the sequence and the metadata file as a signature.

3.2.1.1 PyPulseq

The PyPulseq toolbox implements the functionalities of Pulseq in Python. It provides common RF pulses and gradient waveforms, as well as example sequences. Arbitrary gradient and RF waveforms are also possible, allowing for high flexibility. The additional

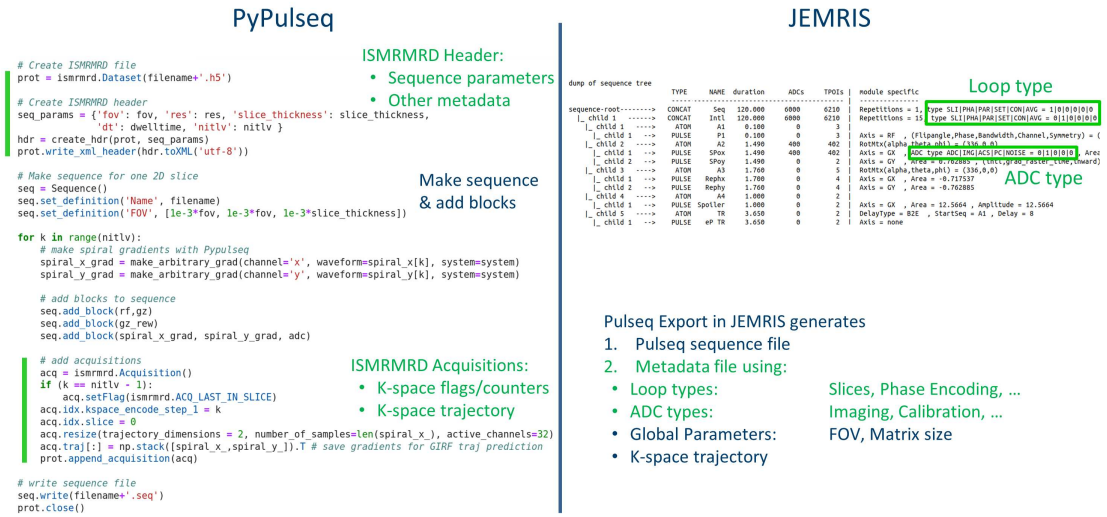

Figure 3.2: Left: Sequence development and metadata file creation with PyPulseq. The metadata file is initialized, and a header is created from global sequence parameters (full header function not shown). The sequence object is created, and event blocks are added. At the same time, readout information such as k-space flags, counters, and the k-space trajectory are added to the metadata file. Right: Dump of the sequence tree from a sequence developed with the JEMRIS simulation framework. The metadata header is generated from the global parameters in JEMRIS. Acquisition-specific k-space information is generated from the new JEMRIS loop-type and ADC-type parameters and added to the metadata, together with the k-space trajectory. Green color indicates new features.

metadata file is created with the Python implementation of the MRD format [81].

First, all elements of a sequence containing RF pulses, gradient waveforms, and ADCs are defined. Sequence parameters such as the FOV, resolution, number of slices, and k-space trajectory type are added to the MRD header as illustrated in Figure 3.2 (left). The timing of the sequence is represented as a gapless concatenation of time slices termed blocks in Pulseq. Each block may define a single RF, ADC or gradient pulse event per gradient axis, whereas each of these events may be delayed by an arbitrary period of time. The duration of each block is defined by the duration of the longest event within that block, or an optional additional delay object that can be used to increase the duration of the block.

For each ADC/readout event present in the sequence, acquisition parameters are added to the MRD metadata file, containing k-space counters, flags, and optionally the k-space trajectory. Further sequence-specific information for reconstruction and postprocessing (e.g., b values for diffusion sequences) can be added by using user defined parameters and arrays. Auxiliary information, such as the sequence name or the FOV, can be added to the Pulseq file. Knowledge about the FOV is useful for a correct visualization of the acquisition volume at the scanner.

3.2.1.2 JEMRIS

JEMRIS provides a graphical user interface for sequence development and the sequence timing is defined in XML files, that can also be edited directly. JEMRIS also provides common RF and gradient shapes, as well as the ability to import user-defined shapes via Hierarchical Data Format (HDF5) files. Sequences can be simulated directly in JEMRIS or exported to the Pulseq format for scanner execution. The export of the JEMRIS sequence XML file to Pulseq is done automatically based on the provided XML file. For this work, the Pulseq file export was extended to support rotations of gradient waveforms with a given rotation angle. This simplifies sequence development for rotationally symmetrical k-space trajectories such as radial or spiral trajectories. Additionally, a new time-optimized spiral gradient [88] was implemented in JEMRIS.

An MRD metadata file is automatically created during export to the Pulseq format. Header information is taken directly from the parameter module in JEMRIS. k-space positions are defined by the k-space trajectory, which is calculated for each ADC event in the sequence. However, because JEMRIS does not distinguish between different types of loops or ADCs, different k-space acquisitions cannot be separated easily. Therefore, the loop-type and ADC-type parameters were added to each pulse module, which is shown in Figure 3.2 (right). The loop type classifies loops to distinguish if different lines in k-space (e.g., phase encoding and partition loop) or different images (e.g., slice, contrast, set, or average loop) are acquired. The ADC type defines the ADC sampling as an imaging ADC or some sort of calibration ADC (noise, parallel imaging calibration, phase calibration).

3.2.2 Data Acquisition and Simulation

Raw data in the presented workflow can originate either from a real acquisition on an MRI scanner or from a simulation with the JEMRIS framework. For the latter, the sequence must be designed in JEMRIS because there is currently no efficient import of Pulseq sequences in JEMRIS.

In a real experiment, the sequence file is exported to the MRI scanner and selected in the scanner graphical user interface (GUI) for execution as shown in Figure 3.1. Pulseq sequences are run with a vendor-specific interpreter sequence, which supports integrated FOV positioning. Currently, sequence interpreters for Siemens (Siemens Healthineers, Erlangen, Germany), GE (General Electric Healthcare, Waukesha, WI, USA), and table-top MRI scanners are available. During sequence execution, both the sequence name and the MD5 signature are saved in the raw data header in order to identify the correct meta-data file in the reconstruction.

Simulation of a sequence in JEMRIS is executed either from the command line or in the GUI by providing the sequence XML file, the digital phantom and its MRI-relevant parameters, and optionally receive and transmit coil sensitivities. An MRD file is generated after simulation (Figure 3.1), containing both the MRI signal and the

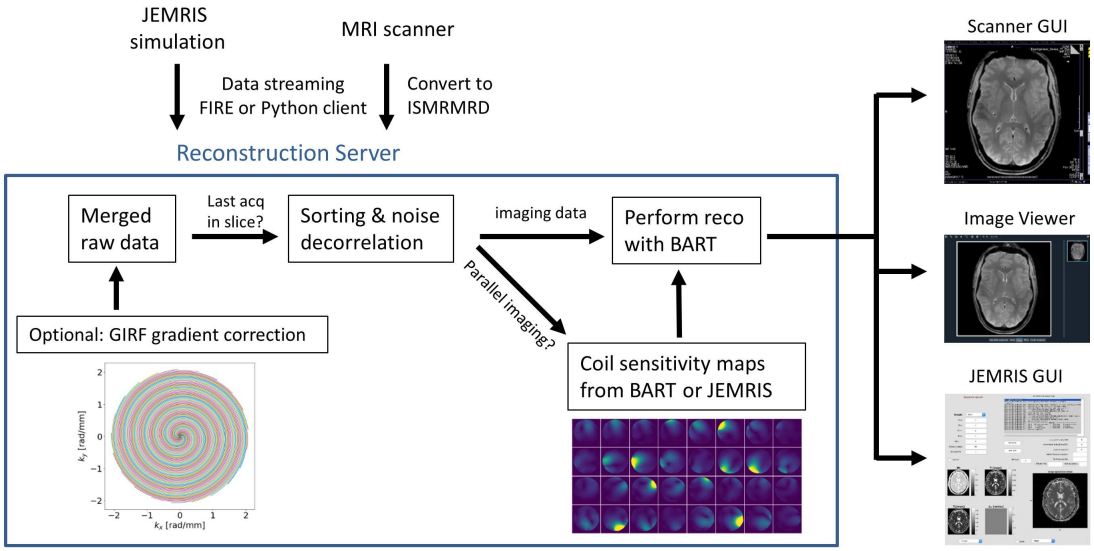

Figure 3.3: Detailed view of the reconstruction pipeline for raw data from an MRI scanner or the JEMRIS simulation framework. Raw data from the scanner are first converted to MRD. The data is streamed to the reconstruction server, which is where the reconstruction pipeline is started. The pipeline supports an optional correction of gradient imperfections with the GIRF. Image reconstruction and optional calculation of coil sensitivity maps are done with BART. Reconstructed images are displayed in the GUI of the scanner, the JEMRIS GUI, or saved to a file. GIRF, gradient impulse response function; GUI, graphical user interface.

metadata as well as receive coil sensitivities for multi-coil simulations.

3.2.3 Image Reconstruction and Postprocessing

The image reconstruction is initiated by streaming the raw data to a Python server running inside a Docker container. Data processing scripts are selected by a configuration string sent to the server together with the raw data. An overview of the pipeline is given in Figure 3.3.

3.2.3.1 MRI Scanner Data

Raw data from the scanner are converted to the MRD format and streamed to the reconstruction server by a client using a format initially developed by the Gadgetron framework and extended for other workflows. This is done either online with a vendor-dependent interface or offline with a converter and a Python-based client. Converters from the most common vendor data formats to MRD are provided by the MRD project (`https://github.com/ismrmrd`). The prototype Siemens framework for image reconstruction environments (FIRE) [89] was used as the vendor interface for online reconstruction in this work. This interface allows real-time streaming of acquired data, which can be selected in the scanner GUI prior to execution of the sequence. The online pipeline is configured with an XML file that is linked to the Pulseq interpreter sequence [89], similar to the configuration used by the Gadgetron project [80].

Prior to image reconstruction, the MRD metadata file is transferred to the reconstruction server. The header and k-space information from the metadata file are automatically merged with the corresponding raw data in the reconstruction pipeline. Optional trajectory correction with the gradient impulse response function (GIRF) [90] can be performed by supplying gradient shapes instead of k-space trajectories. This requires knowledge of the scanner-specific GIRF as well as additional information for aligning the trajectory with the ADC readout samples.

Image reconstruction is triggered when all data for a complete image is collected, for example, by a metadata flag identifying the last acquisition in a slice. The pipeline contains processing steps for sorting the data, noise prewhitening with noise scans, and parallel imaging calibration using reference k-space data. Prescan data is separated from imaging data by reading the corresponding metadata flags. Calculation of coil sensitivity maps is done with the eigenvector-based iterative self-consistent parallel imaging reconstruction (ESPIRiT) algorithm [58], implemented in BART. Other reconstruction steps, such as k-space filtering and application of phase navigator data, can be integrated into the existing pipeline.

Fully sampled Cartesian data are reconstructed with a simple fast Fourier transform (FFT) in Python, whereas undersampled and non-Cartesian data are processed with BART using its parallel imaging and Nonuniform fast Fourier transform (NUFFT) implementations. If sensitivity maps were calculated, the parallel imaging with compressed sensing reconstruction (pics) implemented in BART is executed. Online reconstructed data are streamed back to the MRI scanner in real time and can be viewed in the scanner console GUI while the acquisition is still ongoing. Images that were reconstructed in offline mode are stored in the MRD image format.

3.2.3.2 JEMRIS Simulation Data

For simulated data, the reconstruction pipeline can either be started from the JEMRIS GUI or from the command line. In the first step, the MRD data are streamed to the server application (Figure 3.3). Simulated data are processed with the same pipeline as data from the MRI scanner that were acquired with a JEMRIS sequence. The MRD file created after simulation already contains both metadata and imaging data. In the case of multiple simulated receiver coils, the coil sensitivities that were used during the simulation are directly passed to the pipeline. If no additional reference data for parallel imaging calibration are acquired in the simulation, these coil sensitivities are also used in the reconstruction.

Currently, it is not possible to define Cartesian k-space sampling for JEMRIS sequences in the metadata or to detect Cartesian sampling during the reconstruction. Therefore, the image reconstruction treats all simulated data as non-Cartesian and thus requires the k-space trajectory, even if all data points lie on a Cartesian grid. Reconstruction is done either with BART's NUFFT or with its parallel imaging reconstruction

implementation. After reconstruction, images are saved in the MRD image format and displayed in the JEMRIS GUI if the pipeline was started from the GUI.

3.2.4 Experiments

Different imaging sequences were created with the JEMRIS GUI, as well as with PyPulseq, to demonstrate the flexibility of the presented workflow. Experimental data were mainly acquired on a 7 Tesla (T) scanner in Bonn (Siemens Magnetom 7T Plus, Siemens Healthineers), whereas one example sequence was additionally executed on several 3T scanners as described below. The first example sequence designed with JEMRIS contains a 3D GRE Cartesian readout. Signal excitation was achieved by a nonselective block excitation pulse with a duration chosen to achieve water excitation (suppressing fat signal) at 7T ($d = 1.02\,\mathrm{ms}$). The acquisition was accelerated by a factor of $R = 4$ in the first phase-encoding direction, with and without a CAIPIRINHA [91] shift of $\delta = 1$. FLASH-based low-resolution reference scans were acquired prior to the measurement in order to obtain coil sensitivity maps. The FOV was $210 \times 210 \times 160\,\mathrm{mm}^3$ at 1 mm isotropic resolution. The measurement was repeated with 4 different variations:

1. TE = 5 ms, TR = 10 ms, with RF spoiling
2. TE = 5 ms, TR = 10 ms, with RF spoiling, fat-selective sinc-pulse (1 kHz bandwidth) instead of water excitation
3. TE = 25 ms, TR = 30 ms, no RF spoiling
4. TE = 25 ms, TR = 30 ms, no RF spoiling, no CAIPIRINHA shift

As a non-Cartesian example, a 2D spiral sequence with a time-optimized [88] k-space trajectory was created using both JEMRIS (without fat saturation pulse) and PyPulseq (with fat saturation pulse). One slice with a slice thickness of 1 mm and a FOV of $220 \times 220\,\mathrm{mm}^2$ at 1 mm isotropic resolution was acquired. The PyPulseq version of this sequence was additionally executed at 2 3T scanners in Bonn (3T Skyra, Siemens Healthineers) and Freiburg (3T Prisma, Siemens Healthineers) to demonstrate portability. It was successfully executed also on a 3T Vida scanner (Siemens Healthineers) running on a different vendor's software version (results not shown). Additionally, the sequence was converted to the TOPPE [79] file format using the PulseGEq converter provided by the TOPPE project [92]. It was then executed on a 3T UHP scanner (General Electric Healthcare) to show the compatibility of the pipeline across 2 different vendors. At 3T, both the slice thickness (3 mm) and TR (200 ms) were increased for higher SNR and better contrast. Because the TOPPE format currently does not support ADC sampling intervals of different duration, coil sensitivity calibration was performed with the spiral data.

A slightly modified version of the same spiral sequence was simulated in JEMRIS, demonstrating the influence of chemical shift and susceptibility in a sample. In the simu-

lation, gradient spoiling was replaced with long TR spoiling because correct simulation of gradient spoiling needs many simulated spins resulting in exceedingly long computation times [93].

A 2D Cartesian B0 mapping sequence was developed to show the postprocessing capabilities of the reconstruction pipeline and to allow for B0 correction of the spiral imaging data. One slice with 2 mm slice thickness and a FOV of $220 \times 220\,\mathrm{mm}^2$ at 2 mm isotropic resolution was acquired.

All images were reconstructed with BART. Calculation of the B0 field map from raw GRE images was done with Python, using the scikit-image [94] and SciPy [95] libraries for phase unwrapping and filtering. The spiral data acquired with the PyPulseq sequence were reconstructed with a GIRF predicted trajectory. The PowerGrid toolbox [96] was used in the pipeline to achieve B0 correction of the spiral data with a time-segmented reconstruction approach [97] using the B0 field map calculated before. Online reconstruction was performed exclusively on the 7T MRI scanner.

3.3 Results

Reconstructed images from the 3D GRE sequence designed with JEMRIS are displayed in Figure 3.4. Images with water excitation in the upper row show a typical T_1 weighted contrast at short TE. Fat signal in the skull is suppressed, whereas it is the dominant signal in the fat excited images in the lower row. However, images acquired with fat excitation still show some residual water signal in the brain. Figure 3.5 shows images from the same 3D GRE sequence with a longer TE time with and without CAIPIRINHA shifts, demonstrating a T_2^* contrast. The CAIPIRINHA shift reduces artifacts, which are especially visible in the sagittal view where stripe-shaped artifacts disappear.

In Figure 3.6 (A) the magnitude GRE image from the B_0 mapping sequence at the first TE ($\mathrm{TE} = 2.04\,\mathrm{ms}$) is shown. The phase difference map in Figure 3.6 (B), which was calculated from both echoes, has no visible phase wraps in the brain. Figure 3.6 (C) is the resultant B_0 field map, which was smoothed with Gaussian ($\sigma = 0.5\,\mathrm{pix}$) and median filters (kernel size 2×2 pix).

Images acquired with the 2D spiral sequence are shown in Figure 3.7. The image (A), acquired without fat suppression, shows a stripe-shaped artifact at the periphery of the brain caused by folded fat signal. The overall blurring in this image is mainly due to B0 inhomogeneities. In image (B), fat artifacts are removed due to the fat suppression pulse and blurring is reduced significantly. In (C), the same image with additional B0 correction using the map in (C) has even less blurring, and signal is recovered especially in the anterior part of the brain. The images acquired at all three 3T scanners in (D)-(F) show only minor artifacts in the frontal brain, mostly caused by B0 inhomogeneities. Slight geometric distortions presumably due to gradient imperfections are visible in the posterior part of the brain.

Reconstructed images from one simulated slice acquired with a spiral sequence are

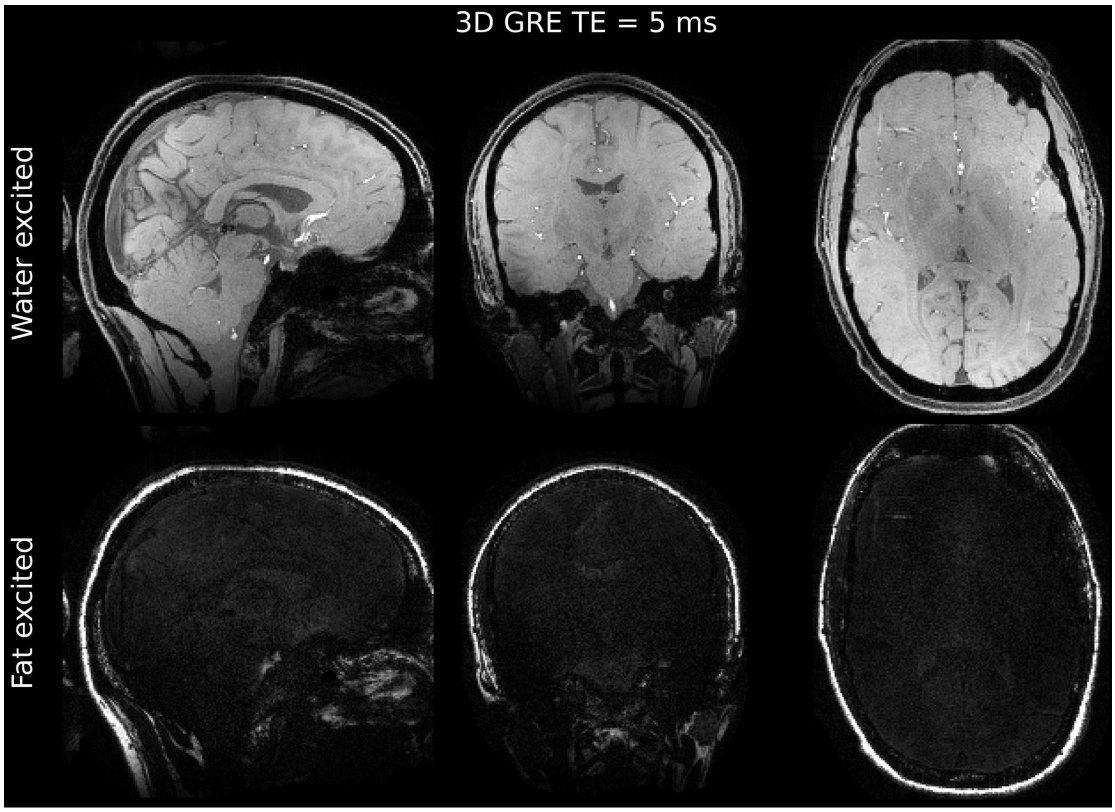

Figure 3.4: Reconstructed images from a T_1 weighted 3D GRE sequence created with JEMRIS, with a TE of 5 ms and 4× undersampling with a CAIPIRINHA shift. Water images were acquired with block pulses of 1.02 ms length suppressing fat signal (upper images), whereas fat excitation was achieved with fat-selective sinc-pulses (lower images). CAIPIRINHA, controlled aliasing in volumetric parallel imaging; GRE, gradient echo.

shown in Figure 3.8. Simulating a clean digital phantom yields artifact-free images. Adding the chemical shift of fat to the digital brain phantom results in stripe-shaped artifacts similar to the artifacts in Figure 3.7 (A). Including magnetic susceptibility in simulations that is causing B_0 inhomogeneities leads to the typical blurring artifact, well-known in spiral imaging. Both chemical shift and susceptibility differences lead to signal loss, especially in the lower brain (upper row in Figure 3.8).

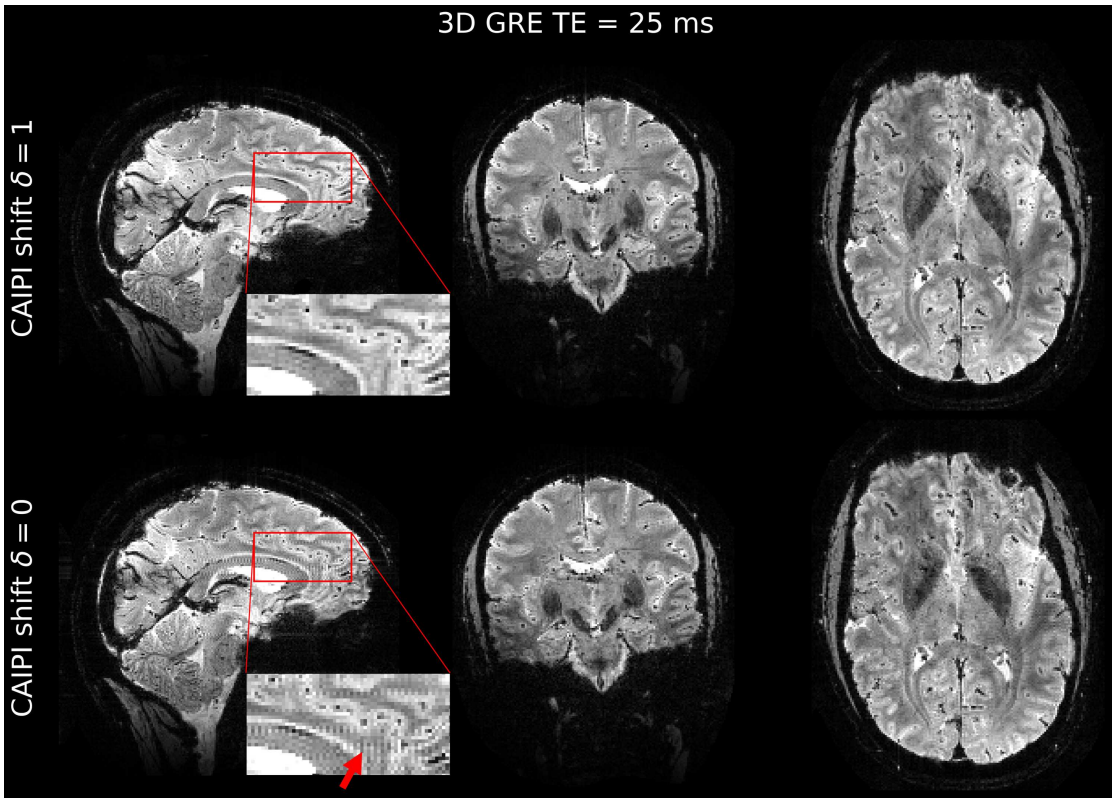

Figure 3.5: Images from the same 3D GRE sequence as in Figure 3.4, with a TE of 25 ms. Upper images were acquired with a CAIPIRINHA shift, whereas lower images were acquired without this shift. The red arrow indicates artifacts in images without CAIPIRINHA.

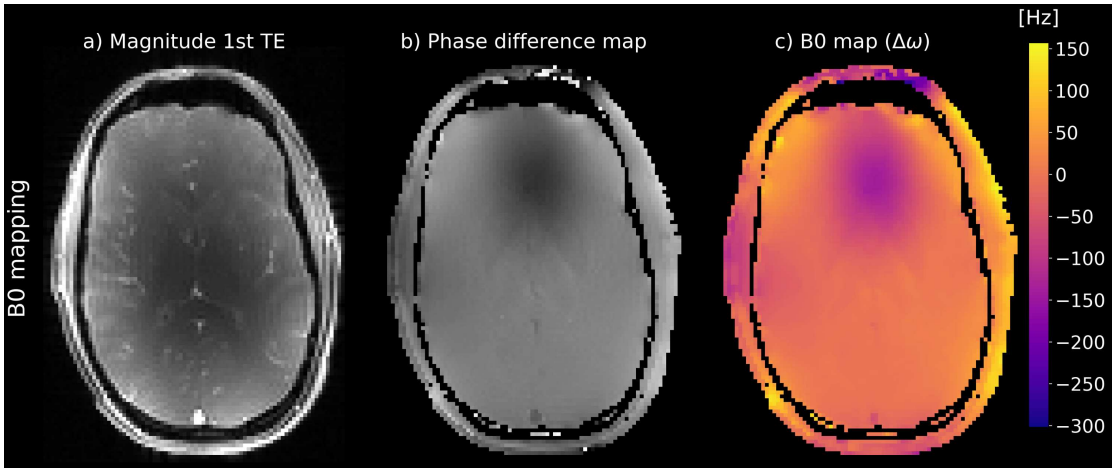

Figure 3.6: Reconstructed images from a B0 mapping sequence. Image (A) is the first magnitude image with TE = 2.04 ms; (B) is the phase difference map of the 2 echoes; and (C) shows the corresponding filtered B0 field map.

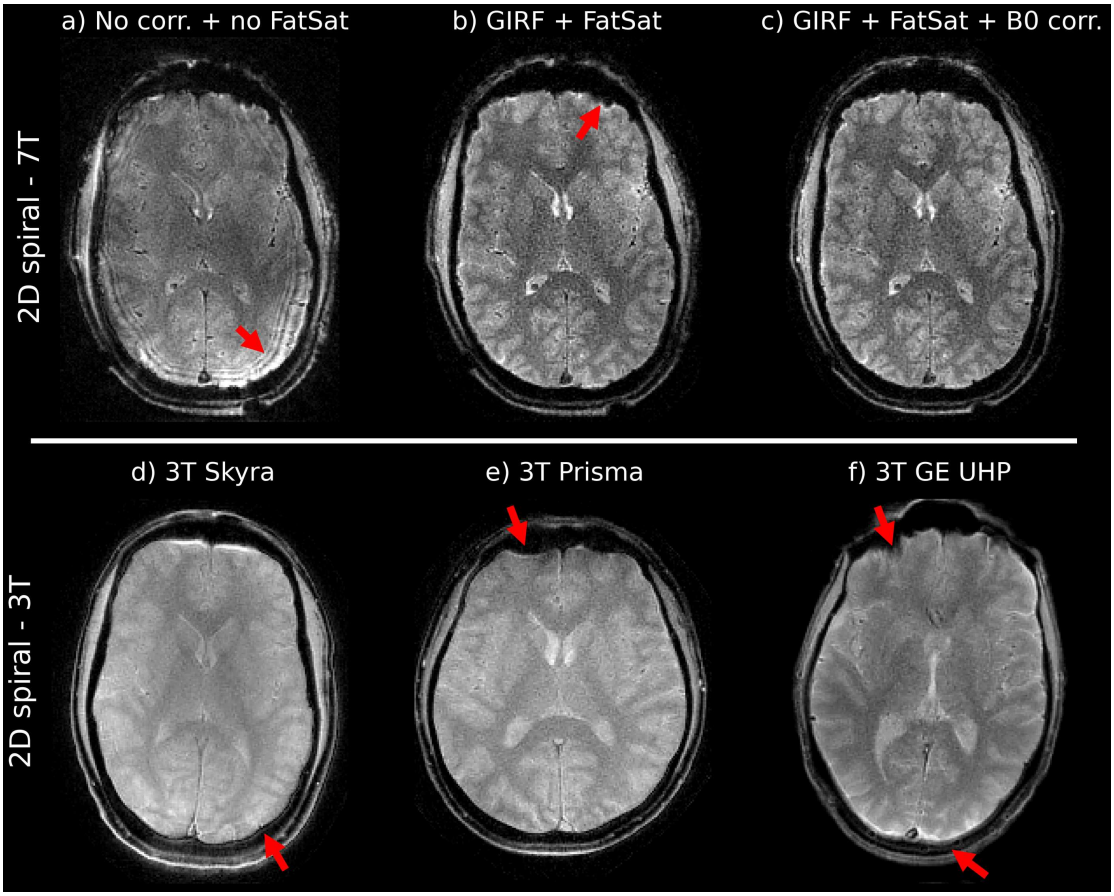

Figure 3.7: Reconstructed images from a 2D spiral GRE sequence acquired at 7T (A-C) and 3T (D,E) scanners from 4 different subjects. Image (A) was acquired with a spiral sequence without fat suppression; whereas in (B) fat suppression was added to the sequence, and GIRF trajectory correction was done in the reconstruction. Image (C) was reconstructed from the same raw data, but with an additional B0 correction using the field map shown in Figure 6C. Images (D-F) were acquired at 3 different 3T scanners with fat suppression, but without GIRF correction in the reconstruction. Red arrows indicate artifacts from gradient imperfections and from off-resonance due to chemical shift and magnetic susceptibility. T, Tesla.

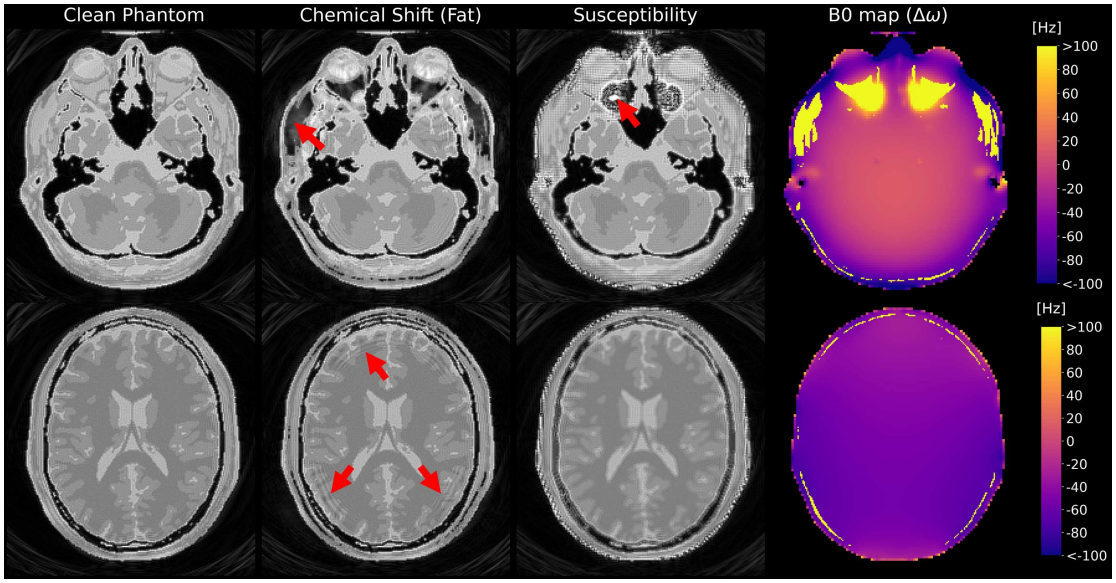

Figure 3.8: Images reconstructed from data simulated with the JEMRIS simulation framework. A spiral sequence was simulated for 2 different slices either with a clean digital phantom, with additional chemical shift from fat or with susceptibility differences across the digital brain phantom. Artifacts from chemical shift and susceptibility are indicated by red arrows. The B_0 maps on the right show both chemical shift (at approximately 1 kHz) and susceptibility-induced off-resonance effects.

3.4 Discussion

3.4.1 Flexibility and Extensibility

The examples presented in this chapter demonstrate the high flexibility of the proposed workflow regarding the sequence design methods and the applied reconstruction algorithms. Advanced imaging techniques such as parallel imaging with CAIPIRINHA or non-Cartesian sampling are integrated in the workflow. The workflow allows users to prototype new sequences and reconstruct the acquired data with vendor-independent tools. Existing code for sequence generation can easily be extended with additional sequence design tools, such as Sigpy [98] or the gradient optimization toolbox GrOpt [99].

Based on the example of a spiral sequence, we showed that sequence execution across different scanners and vendors is possible using the same image reconstruction pipeline (with minor modifications). However, porting a sequence from 1 acquisition system to another requires adhering to any differences in hardware properties and safety limits that may exist. For example, in the presented spiral sequence, the gradient slewrate had to be slightly reduced from 7T to 3T scanners due to peripheral nerve stimulation limits.

For the conversion of the spiral sequence to the GE-compatible format TOPPE, prescans for noise and coil sensitivity calibration had to be removed. These prescans can be acquired with separate sequences, but this does require manual integration of the calibration data into the spiral reconstruction. Small timing changes were needed to fit the requirements of the TOPPE format with only minimal effect on the acquired data for this particular sequence. Because TOPPE is a relatively young file format under active development, future improvements regarding the compatibility of Pulseq and TOPPE are expected.

Furthermore, the workflow allows for comparison of data from the JEMRIS MRI simulator with an actual acquisition at the MRI scanner. This is useful for testing sequences before running them on a real MRI scanner or to investigate the influence of specific physical properties (e.g., presence of fat) on data acquisition. However, simulating the exact same sequence that is running on the MRI scanner sometimes is not feasible because some physical effects might not be included in the simulated model or require excessively long computation times.

The available reconstruction pipelines for both Pulseq and JEMRIS data can reconstruct images from many different MR imaging sequences and can be used as a starting point for more elaborate reconstructions or postprocessing techniques. Additional sequence-specific meta information such as inversion times or b values can be transferred and accessed in the reconstruction pipeline by adding them as user-defined parameters or arrays to the MRD metadata file. BART already provides much functionality for preprocessing and calibration of data, as well as for advanced image reconstruction algorithms. However, integration of new reconstruction or postprocessing tools into the existing pipeline is also possible.

Online integration of the reconstruction pipeline simplifies testing of novel sequences that require nonstandard reconstruction techniques such as non-Cartesian sequences. It also allows using reconstructed images from novel sequences for calibration such as B_0 or B_1-shimming. Because reconstruction scripts can be dynamically embedded into the Docker container without rebuilding, reconstruction scripts can be changed and tested during a scanning session.

3.4.2 Openness and Reproducibility

All file formats used in the workflow are open-source, including the Pulseq sequence file, MRD metadata file, and JEMRIS XML files. Source code of the reconstruction pipelines and sequences developed in Python can be made openly available because no proprietary code is used. Reconstruction pipelines can be shared and deployed via Docker images, which require no additional modifications of the system because all dependencies are already installed inside the container.

In summary, the presented workflow allows sharing the whole imaging workflow by providing the sequence file, metadata file, and reconstruction pipeline. In this way, it is potentially possible to reproduce data acquisition and reconstruction with the same parameters at MRI scanners from different vendors, with different software versions and at different sites. Sharing the source code of both sequences and reconstruction can simplify collaborations between different sites. For sites already using the Pulseq framework, integration of the proposed workflow into existing pipelines would not require much effort.

We demonstrated the portability of the workflow by acquiring images with the same sequence at three different 3T scanners located at three different sites using the same image reconstruction pipeline.

Inline reconstruction directly on the vendor's interface significantly improves the workflow by providing real-time feedback during experiments and improves the user experience by automating the reconstruction. However, inline integration is optional, and all reconstruction pipelines can also be run offline if a vendor-dependent interface is unavailable or a fully open-source pipeline is desired. Therefore, no proprietary software is required for the postacquisition part of the workflow because converters to the MRD file format exist for all common vendor raw data formats.

3.4.3 Performance of the Pipeline

If sequence parameters are changed, both sequence and metadata files must be recreated and transferred to the scanner and the reconstruction server. This procedure can be automated, depending on the local scanner setup, although for long sequences metadata files can get quite large due to redundant trajectory information stored for each readout. The computation times for creating metadata files increases with file size, which might limit rapid testing of different protocols as well as manual parameter optimization at

the scanner for long sequences. However, recreation of the metadata file for online reconstruction is only necessary if reconstruction-specific parameters are changed.

The performance of the reconstruction pipeline depends on many factors, including configuration of reconstruction parameters and possible preprocessing steps. Performance optimization is especially important when the pipeline is to be executed online. The example 2D spiral reconstruction required about 10 s of computation, whereas the 2D Cartesian reconstruction finished in under 1 s. The much larger accelerated 3D Cartesian dataset required about 15 min of computation (16 core CPU, NVIDIA A6000 GPU [NVIDIA, Santa Clara, CA, USA]). Reconstruction times for the simulated data are negligible compared to the simulation times.

For complex reconstructions and large datasets, the total reconstruction time mainly depends on the time for the coil sensitivity calibration and the reconstruction with BART. Optimization of reconstruction parameters or the usage of coil compression hold potential for future performance improvements. For large datasets, reading and merging the metadata takes a significant amount of time. In future development, metadata could be stored in a less redundant way or transferred directly to the scanner at sequence runtime via the Pulseq format to accelerate the merging process.

3.4.4 Limitations

In the current implementation of the reconstruction pipeline, calibration data must be acquired within the same sequence as the imaging data. Separately acquired prescans for coil sensitivity calibration or field correction must be integrated manually into the reconstruction, requiring modification of the reconstruction code. This is unfavorable if the user wants to reconstruct multiple datasets using the same calibration from a single prescan. Future implementation of linking calibration to imaging data would increase usability of the pipeline.

The automatic metadata and sequence file creation from JEMRIS simplifies the development process because no programming is necessary. However, it is currently not possible to add arbitrary user-defined sequence-specific information to the metadata file. Further extension of JEMRIS to include such information may be the focus of future work. Data acquisition by simulation in JEMRIS is only possible for sequences designed in JEMRIS. Conversion of Pulseq sequence files to the JEMRIS XML format is possible [100] although the high-level loop structure of a sequence cannot be recovered from Pulseq files, leading to excessively long computation times in simulations.

Setting up the whole pipeline and extending it for one's own experiments might require some time and experience with Pulseq, the MRD file format, and the processing of streamed data. However, several examples for sequences and reconstruction scripts are available in the GitHub repository, which can be used or modified for one's own purposes.

Online reconstruction of acquired data requires a vendor-dependent interface and is

only feasible if the reconstruction time is not excessively long. Time-consuming reconstruction routines, for example, for non-Cartesian 3D acquisitions may therefore have to be performed offline depending on the computational power of the reconstruction computer.

3.5 Conclusion

The demonstrated end-to-end open-source sequence programming and image reconstruction workflow allows for rapid prototyping and testing of MRI sequences. By using the Pulseq framework, a flexible MRD-based metadata file, and streamed reconstruction pipelines, the whole imaging workflow becomes highly extensible. The workflow enables comparison of data from different MRI scanners and from MRI simulations in JEMRIS using the same pipeline for image reconstruction. The (online) image reconstruction pipeline is versatile because it is not restricted to particular types of MRI sequences and can be extended in various ways with one's own code or using available open-source tools. Because all software in the proposed workflow is open-source, both sequence code and image reconstruction pipelines are vendor-independent and can be shared freely, facilitating greater reproducibility of MRI experiments.

3.6 Data Availability

The source code, sequence and metadata files created with PyPulseq and JEMRIS, and raw data and reconstructed images can be found at `https://github.com/mrphysics-bonn/python-ismrmrd-reco` (Git hash 15df3aa, `https://doi.org/10.5281/zenodo.6683903`). The filenames in the repository are linked to the figures of this chapter as shown in Appendix Table A1. The repository also contains the reconstruction server with instructions on how to set up and use the pipeline (with and without GPU support). A Docker image of the reconstruction server can be found at `https://hub.docker.com/repository/docker/mavel101/bart-reco-server`. The new JEMRIS version with additional examples for the metadata file export and the reconstruction of simulated data are available in the JEMRIS GitHub repository (`https://github.com/JEMRIS/jemris`) and on the JEMRIS website (`https://www.jemris.org/`).

Chapter 4

Improving MR Axon Radius Estimation in Human White Matter using Spiral Acquisition and Field Monitoring

Magnetic Resonance in Medicine, 2024;92:1898-1912

4.1 Introduction

Axons form the neural pathways in the white matter of the human brain. The axon radius is a crucial factor influencing the speed and efficiency of axonal signal transmission [101]. Previous ex vivo studies have associated axonal degeneration with various diseases; for instance, acute axonal damage is a key morphological feature in the early stages of multiple sclerosis [102]. Therefore, the axon radius could serve as an important biomarker, if accurate noninvasive in vivo quantification were possible.

Diffusion-weighted MRI (dMRI) has been proposed as a method for measuring axon radii in the human brain noninvasively [103], [104]. Approaches to model the diffusion-weighted signal in the white matter include both single- and multi-compartment models. Multi-compartment models typically differentiate intra-axonal, extra-axonal and free diffusion (CSF) compartments [103], [105]. If any extra-axonal and free water signal is fully suppressed with sufficiently strong diffusion-weighting [106], it is possible to reduce the model to only the intra-axonal compartment, where axons are typically modeled as impermeable cylinders with finite axon radius [31].

Sensitizing the MR signal to the axon radius requires data acquisition with very strong diffusion-weighting, as the signal attenuation due to diffusion perpendicular to the axonal cylinder is typically small. Therefore, high amplitude gradients are required to achieve imaging at high b-values. In recent years, the noninvasive quantification of axon radii in the human white matter has come into reach, due to the development of high-performance gradient systems like the Connectom system with gradient strengths of up to 300 mT/m [53]. However, even with these gradient systems, the sensitivity of the diffusion-weighted signal is still restricted to large axons greater than approximately 3 µm in diameter [107], which represent only a small fraction of the axon radius distribution [108]. Additionally, pointwise estimates of axon radii using diffusion MRI are heavily weighted towards the larger radii represented by the tail of the distribution [107], [109]. This makes it difficult to gain any information about the underlying distribution of axon radii within a voxel without making any assumptions regarding that distribution [104] or further approximations [106]. In order to maximize the signal attenuation and decrease the resolution limit of axon diameter mapping, the b-value has to be maximized while preserving enough SNR.

Fast MRI sequences are required to acquire diffusion data at sufficiently short echo times and to achieve reasonable scan times. These sequences typically suffer from artifacts due to magnetic field inhomogeneities and eddy currents. The workhorse of dMRI is a 2D multi-band single-shot EPI sequence [4] used in most dMRI studies. This sequence offers fast acquisition of the 2D k-space, but suffers from susceptibility and eddy current induced geometric distortions. Advanced correction methods in image space have been developed [110] allowing the elimination of most of these distortion artifacts. Spiral k-space trajectories offer a promising alternative to a rectilinear EPI readout, as acquisition starts in the center of k-space, resulting in a reduced echo time and potentially

higher SNR [6]. However, single-shot spiral acquisitions are prone to artifacts arising from hardware imperfections and eddy currents, especially in the presence of strong diffusion sensitizing gradients. These artifacts typically manifest as image blurring and can not easily be corrected in image space, due to the non-Cartesian acquisition of k-space. Measurement of the actual encoding fields during the MR sequence, also termed field monitoring, aims to mitigate these artifacts [8]. Combined with an expanded encoding model, even higher order eddy current effects can be corrected in the image reconstruction [9].

In this work we used a custom 2D multi-band spiral sequence combined with field monitoring for the quantification of in vivo MR axon radius estimates. We compared this approach to an established EPI-based axon radius mapping approach using a protocol, which previously showed high repeatability[111]. SNR measures for both sequences were investigated and the variability of the derived axon radius estimates was compared both within one measurement and across two measurements using a test–retest design.

4.2 Methods

A single-compartment model for the diffusion-weighted signal representing only the intra-axonal space was used to derive axon radius estimates [106]. Diffusion-weighted images were acquired at two different high b-value shells as proposed in Veraart et. al.[111]. The lower b-value was set to $6000\,\mathrm{s/mm^2}$ to fully suppress the extra-axonal signal, while keeping the sensitivity to the axon radius at a minimum. The higher b-value was set to $30450\,\mathrm{s/mm^2}$ to maximize the sensitivity to the axon radius, while not exceeding the hardware limits of the scanner and maintaining sufficient SNR.

4.2.1 Data Acquisition

A multi-band single-shot spiral sequence was implemented as part of a pipeline [112] shown in Figure 4.1. The sequence was created with PyPulseq [87] and exported to the Pulseq file format [78]. A spiral k-space trajectory with two interleaves was designed for a nominal resolution of 2.5 mm and accelerated by a factor of R = 2 by using only the first interleave. The spiral trajectory was implemented with time-optimized gradients [88]. The sampling dwell time was 2.2 µs with an oversampling factor of two and 8364 samples per shot. The multi-band pulses (acceleration factor MB = 2) were created from single-band Shinnar–Le Roux RF pulses from the vendor's pulse library, applying a minimum-time VERSE algorithm to reduce peak RF power [66].

The spiral sequence included a dual-echo GRE prescan at $1 \times 1 \times 2.5\,\mathrm{mm^3}$ resolution with an acquisition time of TA = 1:40 min. Data were acquired at echo times $\mathrm{TE_1}$ = 2.42 ms and $\mathrm{TE_2}$ = 4.84 ms, where the water and fat signals are in phase at a field strength of 3 T. This prescan was used for mapping of the static off-resonance fields and estimation of coil sensitivities. The spiral data were acquired straight axial, with no tilt

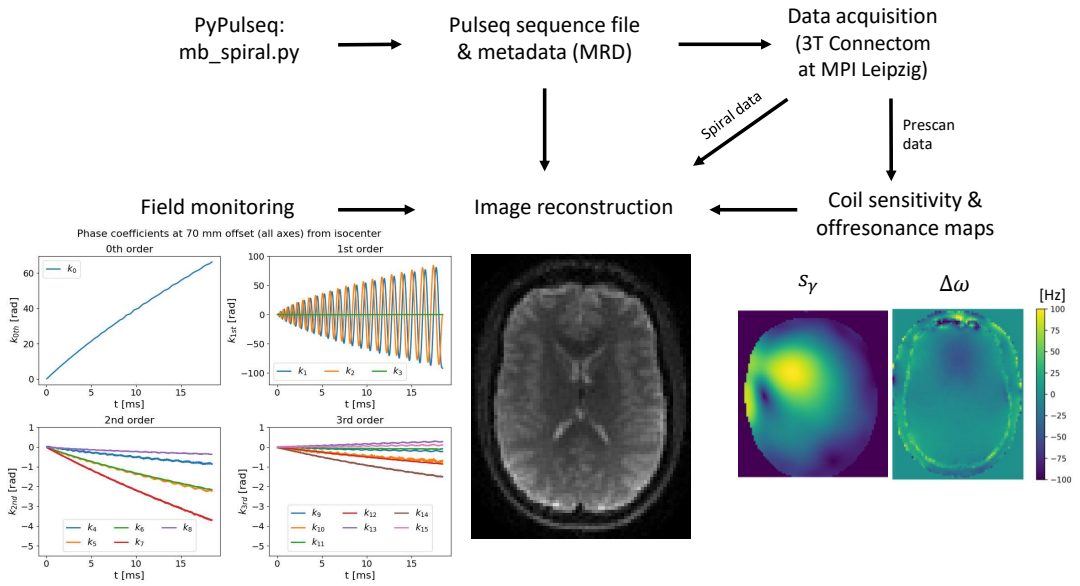

Figure 4.1: Spiral sequence development and image reconstruction pipeline [112]. The spiral sequence was designed using PyPulseq and Pulseq. The sequence includes a dual-echo gradient echo (GRE) prescan for coil sensitivity calibration and mapping of static off-resonance. Image reconstruction with an expanded encoding model was implemented in the PowerGrid toolbox using k-space phase coefficients of up to third spatial order. An example set of phase coefficients measured with a field camera (Skope) is shown on the left.

applied.

A multi-band EPI sequence with blipped-CAIPI (MB = 2) and in-plane GRAPPA acceleration (R = 2) [4] was used as a reference method, as it gave repeatable results in a previous study [111]. In contrast to that study, we only used one instead of two repetitions of the diffusion protocol. The phase-encoding resolution was 88 % of the nominal resolution of 2.5 mm, resulting in 77 phase-encoding lines and 13552 samples per shot (no partial Fourier). The missing phase-encoding lines were zero-filled in the reconstruction. The EPI sequence uses ramp sampling and the sampling dwell time was 2.5 µs with an oversampling factor of two. The EPI data were acquired with anterior-posterior phase-encoding with a slight tilt along the bottom of the corpus callosum, approximately along the anterior commissure – posterior commissure line.

The following parameters were kept constant for both sequences: TR = 3.5 s, FOV = $220 \times 220 \times 135\,\mathrm{mm}^3$, 2.5 mm isotropic voxels. Data were acquired with interleaved b-values $b = 0\,\mathrm{s/mm}^2$ (b0; ten volumes), $b = 6000\,\mathrm{s/mm}^2$ (60 non-colinear directions on the sphere) and $b = 30450\,\mathrm{s/mm}^2$ (120 non-colinear directions on the sphere) with diffusion gradient parameters $G_{max} = 280\,\mathrm{mT/m}$ (maximum amplitude), $\Delta = 29.25\,\mathrm{ms}$ (spacing between diffusion gradients) and $\delta = 15\,\mathrm{ms}$ (diffusion gradient duration). For the EPI sequence, ten b0 volumes were acquired with inverted phase-encoding direction (posterior-anterior) for susceptibility-induced distortion correction.

The respective echo times of the spiral (TE = 52 ms) and EPI sequences (TE = 66 ms) were minimized for the given parameters. The readout durations were 18.4 ms

for the spiral and 22.8 ms for the EPI sequence, and the total acquisition times were TA = 13:07 min (spiral) and TA = 13:27 min (EPI) including all prescans and the inverted phase-encoding b0 acquisition.

In addition to the diffusion data, T1-weighted anatomical images were acquired with an MPRAGE sequence. These images were used for registration and segmentation of white matter. MPRAGE data were acquired at 1 mm isotropic resolution with a FOV of $256 \times 256 \times 192\,\mathrm{mm}^3$.

Data were acquired from ten healthy volunteers (five male, five female, age between 19–36) after giving informed consent on a 3 T Connectom scanner with a maximum gradient strength of 300 mT/m using a 32 channel RF-receive coil (Siemens Healthcare, Erlangen). For each volunteer, test and retest data were collected in two scanning sessions with a short break of 10-20 min in-between using the same imaging protocol. The subject was removed from the scanner and then repositioned during the break. For one subject (subject 7), the test–retest acquisition was repeated twice to investigate the source of a bias in the repeatability metrics observed during the analysis in three of the subjects. The initial scan for this participant had been in the afternoon after several subjects had already been scanned, and so the second acquisition was performed first thing in the morning to investigate the effect of scanner load on the repeatability.

4.2.2 Field Monitoring and Image Reconstruction

For the spiral sequence only, the dynamic field evolution was monitored using a field camera (Skope Magnetic Resonance Technologies AG, Zurich) with 16 ^{19}F-based NMR field probes. The spatially-varying field was estimated with spherical harmonic basis functions up to third order and second order concomitant field functions [8].

The field monitoring data were acquired in a separate scan session with the field probes placed inside the RF coil mounted on a plastic frame in optimized positions [113] to allow for third spatial order spherical harmonic fitting. Field data were captured for every second spiral shot as the shot-TR of 130 ms was too low to allow for proper relaxation of the field probes. The field probe data of the missing shots were acquired in a second scan, which was performed after a break to regain the initial state of the MR scanner. The field data collected in this separate scan session was used for reconstruction of spiral data from all subjects.

Image reconstruction was done with an iterative sensitivity encoding (SENSE) reconstruction [67] using the PowerGrid toolbox [96]. Image reconstruction was based on an expanded signal model [9]:

$$\sigma_\gamma(t) = \int \rho(\mathbf{r}) s_\gamma(\mathbf{r}) e^{-i[\sum_j k_j(t) h_j(\mathbf{r}) + \Delta\omega(\mathbf{r}) t]}. \tag{4.1}$$

Here, $\sigma_\gamma(t)$ is the signal of receive coil γ at time point t, $\rho(\mathbf{r})$ is the transverse magnetization at voxel position $\mathbf{r}$ and $s_\gamma(\mathbf{r})$ is the sensitivity of the respective receiver coil

at that position. The phase term includes the phase coefficients $k_j(t)$, measured with the field camera, multiplied by the respective spatial basis function $h_j(\mathbf{r})$ [8]. A zeroth order phase shift $k_0(t)$ is already applied to the data by the vendor's eddy current compensation (ECC) at the acquisition stage. As the vendor does not allow this ECC to be disabled, this additional global phase shift had to be reversed before image reconstruction. Otherwise, this phase would be corrected twice by the ECC and the field probe data. During conversion of the raw data to the MRD format [81], the global phase $k_0(t)$ applied by the ECC is calculated using the nominal gradient time courses of the sequence and the vendor's eddy current model. Afterwards, the raw data is multiplied by the conjugate of these values to reverse the ECC [1].

The signal model additionally considers the phase evolution due to the spatially-dependent static off-resonance field $\Delta\omega(\mathbf{r})$. For the calculation of static off-resonance field maps, phase difference maps between the first and second echo were calculated channel-wise from the GRE prescan using the Hermitian product. After phase-unwrapping, the lowest and highest quartile of phase difference values in a voxel across channels was removed [40]. Off-resonance maps were calculated by combining channel-wise maps with a weighted sum, where the weights represent the magnitudes of the respective channels, and dividing by the echo-time difference. Coil sensitivity maps were determined from the first echo of the prescan using the ESPIRiT algorithm [58]. The conjugate-gradient algorithm was used to solve the signal model for the image $\rho(\mathbf{r})$ [67]. Iteration was stopped after a maximum number of 20 iterations or when the relative change of the iteration error norm fell below a threshold of 0.01 %.

4.2.3 Image Preprocessing

Preprocessing of the images included Gibbs-Ringing correction [114], susceptibility-induced distortion correction, motion correction, eddy current correction up to 3rd order with "FSL eddy" [110], [115], [116] and gradient nonlinearity correction [117]. In the spiral data, "eddy" was only used for motion correction as eddy currents and distortions were already addressed during the reconstruction. The diffusion-weighted images were normalized to the mean non diffusion-weighted (mean b0) image and spherical-harmonic coefficients of up to sixth order were calculated for both b-value shells using a maximum-likelihood estimator [118]. In order to account for the Rician distribution of the data, a noise map was calculated [119] using only the lower b-value ($b = 6000\,\mathrm{s/mm^2}$) shell and the non diffusion-weighted images. This noise map was used to improve the precision of the spherical-harmonic fit.

Although, in "eddy" an alignment of the shells is performed, we observed a shift between the two shells in the EPI data after spherical-harmonic fitting. Therefore, in the EPI data an additional registration of the higher b-value shell to the lower b-value shell was done using "FSL FLIRT" [120]. The warp fields of "eddy", the gradient

[1] `https://github.com/SkopeMagneticResonanceTechnologies/siemens_to_ismrmrd`

nonlinearity correction and the additional alignment with FLIRT were concatenated to avoid repeated interpolation.

The T1-weighted anatomical images were brain-extracted, denoised and bias field corrected using ANTsPy and ANTsPyNet [121].

The exact parameters used in each image (pre)processing step can be found in the Github repository included in the Data Availability Statement.

4.2.4 MR Axon Radius Quantification

The powder-averaged signals $\bar{S}(b)$ of both shells were computed from the zeroth order spherical harmonic coefficients [122]. In the absence of extra-axonal signal, the intra-axonal radial diffusivity, $D_a^{\perp}$ can be estimated from the powder-averaged signals using the relation[111]:

$$\bar{S}(b) = \frac{\beta}{\sqrt{b}} e^{-b_{\text{eff}} D_a^{\perp}}, \tag{4.2}$$

where β is a signal scaling factor. An effective b-value was calculated for each voxel to account for gradient nonlinearities [123], [124]:

$$b_{\text{eff}} = \frac{1}{n} \sum_{i=1}^{n} \text{Tr}(\mathbf{B}_{i,\text{eff}}), \tag{4.3}$$

where n is the number of directions for the respective b-value and $\mathbf{B}_{\text{eff}}$ is the effective B-tensor in each voxel. The effective B-tensor was calculated for each direction using the spatial deviations from the nominal magnetic field gradients, which were determined in the gradient nonlinearity correction. The radial diffusivity $D_a^{\perp}$ was then estimated together with the prefactor β by non-linear least squares fitting. The MR estimate of the axon radius r_{MR} was calculated with the relation [106]:

$$r_{\text{MR}} = \left(\frac{48}{7} \delta(\Delta - \delta/3) D_0 D_a^{\perp} \right)^{1/4}, \tag{4.4}$$

where D_0 is the diffusivity of the axoplasm, which was set to $D_0 = 2500\,\mu\text{m}^2/\text{s}$ [111].

All axon radius maps were registered to T1-weighted MPRAGE images using FSL FLIRT [120]. Afterwards, white matter was segmented based on the T1-weighted images with FSL FAST [125]. A white matter mask was calculated from white matter partial volume maps using a threshold of > 0.85. Masks of the corpus callosum were generated using the “Hammersmith n30r95" atlas [126]. The corpus callosum was extracted from the atlas and registered from MNI to T1 space with ANTsPy using the “MNI152-T1 1mm" template. The resulting masks were slightly eroded to avoid including voxels containing CSF.

The axon radius was additionally estimated along the left corticospinal tract (left CST) by applying along-fibre quantification [127] using Dipy [128] and pyAFQ [129]. In a first step, 3000 tract-specific streamlines were generated for the left CST using

MRTrix3 [130]–[132]. Streamline outliers were removed by a cleaning process described in Ref. [127]. The ends of the fibre bundle were clipped to a compact bundle without strongly diverging streamlines. Fibre bundles were calculated only once for each subject based on the first spiral dataset after it was registered to the halfway space of the first and second session. Prior to along-fibre quantification, individual datasets were registered to this halfway space.

The bundle was divided into 100 equidistant segments of equal length and the powder-averaged signals of both shells and the effective b-values were averaged in each segment. Gaussian weights were applied in the averaging to suppress contribution from streamlines that diverge strongly from the center line of the bundle [127]. The axon radius was then estimated for each segment along the tract in the same way as in the voxel-wise analysis.

4.2.5 Statistics

SNR measures were generated by dividing the mean b0 images and the mean images of both shells by the noise map from the denoising step. The ratio of the mean SNR measure between spiral and EPI data in white matter voxels was calculated for all shells across all subjects and both sessions.

In order to investigate the repeatability, the test–retest variability (TRV) of axon radius estimates in the white matter and in segments of the left CST was calculated by [111]

$$\mathrm{TRV} = \frac{\sqrt{\pi}}{2N} \sum_{i=1}^{N} \frac{|\Delta_r(i)|}{\mu_r(i)}, \tag{4.5}$$

where $\Delta_r(i)$ is the difference and $\mu_r(i)$ the mean axon radius estimate of test and retest for the i-th voxel or segment respectively.

4.3 Results

4.3.1 SNR Comparison

Maps of the SNR measure for the first subject are shown in Figure 4.2 for the mean images of all shells. The SNR was higher in spiral images compared to EPI in all shells for all white matter regions. The SNR was overall higher in the periphery and in superior parts compared to the center and inferior parts of the brain.

The average SNR gain across all subjects and sessions is shown below the SNR maps as a ratio of spiral and EPI mean SNR values. The SNR gain was higher in the mean b0 images (30 %) and the lower b-value shell (29 %) compared to the high b-value shell with 19 % SNR gain. The SNR ratio was consistent with a standard deviation of around $\sigma = 0.02$ across all subjects and sessions for all three cases.

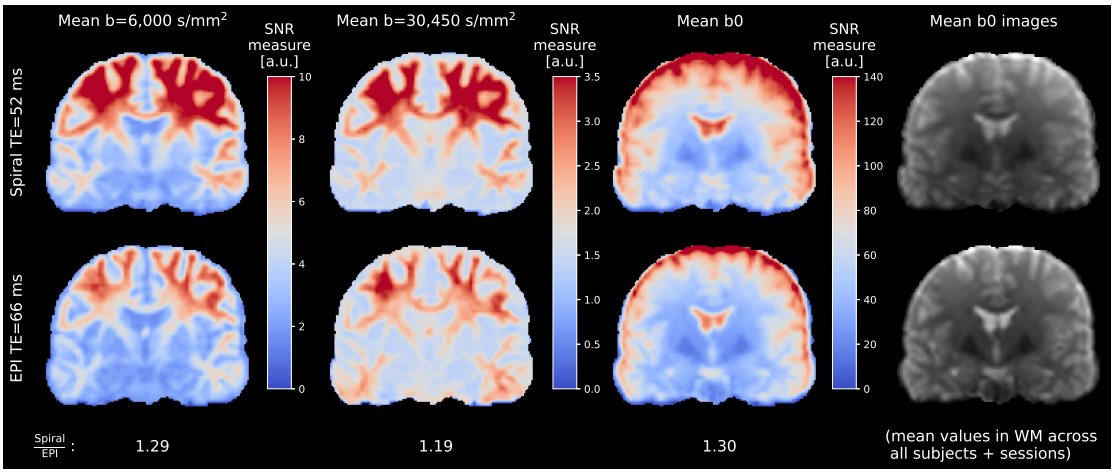

Figure 4.2: Maps of the SNR measure of the first subject for the mean signal of both shells and the mean b0 signal for spiral (top row) and EPI (bottom row) acquisitions. The last column shows the mean b0 images. Below the maps, the ratios of the mean SNR measure across all subjects and sessions in the white matter (WM) are displayed.

4.3.2 MR Axon Radius Mapping

Whole-brain maps of the axon radius estimates for the first subject are shown in Figure 4.3. In the white matter, the axon radius estimates varied mostly between 2 µm and 3.5 µm. The EPI data showed more voids in the axon radius maps, especially in the frontal lobe and in inferior brain regions, indicating regions where no reasonable axon radius was estimated in the fitting procedure.

Figure 4.4 shows an overlay of the MR axon radius estimates in the white matter on T1-weighted volumes for the first two subjects. Lower spatial variation of axon radius estimates across the white matter was observed in the spiral maps compared to EPI maps. Axon radius estimates dropped close to zero especially in inferior regions of the EPI maps, while this was not the case in spiral maps.

The lower variability of axon radius estimates in the spiral data was also reflected in the histograms of these estimates in the white matter (Figure 4.5), where the standard deviations were lower for the spiral data in both subjects by around a factor of 1.5. For EPI datasets, the distribution of axon radius estimates had a longer tail towards zero compared to the spiral datasets. Comparing data from all subjects (Appendix Figure A1), in almost all cases both the mean and the median of the estimated MR radius were higher in spiral datasets compared to EPI, while the standard deviation was lower in all cases. The histograms in Appendix Figure A2 show a direct comparison of spiral and EPI data. The peaks of the axon radius distributions were similar in almost all cases, but the longer tail of EPI distributions led to overall smaller median and mean values. Mean and median values of axon radius estimates in the corpus callosum (Appendix Figure A3) differed in some cases from the whole white matter and the standard deviations tended to be slightly higher.

Profiles of the axon radius along segments of the left CST are shown in Figure 4.6.

The mean axon radius estimates across subjects (solid line) were relatively constant across the whole tract in the spiral datasets for both test and retest, while in the EPI datasets, the mean radius increased from inferior towards superior positions. The variability of individual subjects (shaded lines) was also higher in the EPI data compared to spiral data, as indicated by a narrower 95% confidence interval (dashed lines).

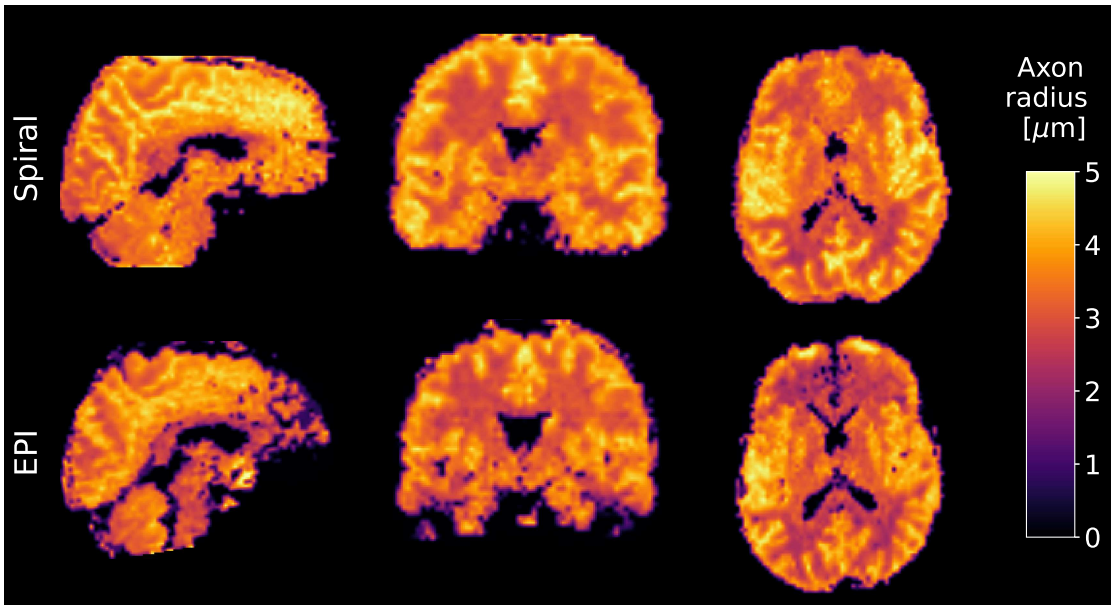

Figure 4.3: Axon radius maps estimated from spiral (top row) and EPI (bottom row) data of the first subject. The maps are thresholded at 5 μm, which was the upper bound used in the axon radius fitting procedure.

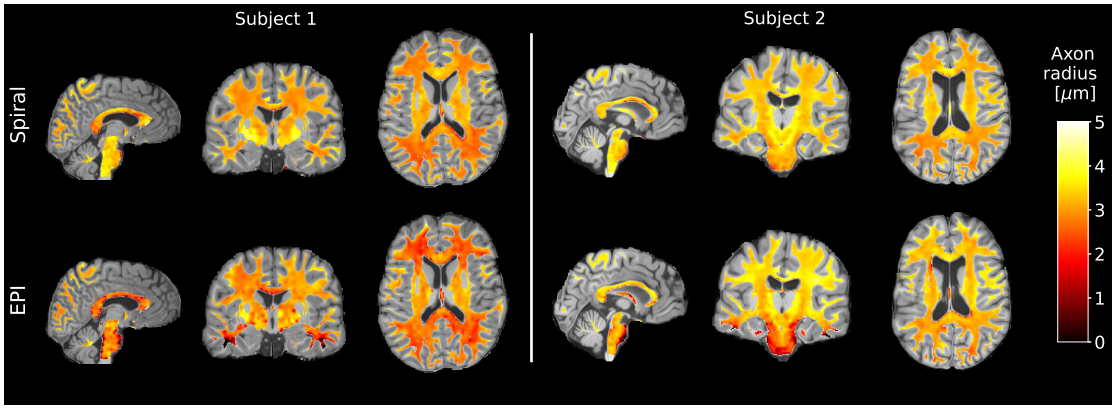

Figure 4.4: Overlay of estimated MR axon radius distributions in the white matter onto anatomical MPRAGE volumes for the first two subjects.

4.3.3 Test–Retest Reliability

The Bland-Altman plots in Figure 4.7 show the agreement between test and retest measurements. A low absolute mean difference (bias) was observed for most subjects, while for some subjects (e.g. subjects 7 and 10) there was a significant bias of up to 10% of

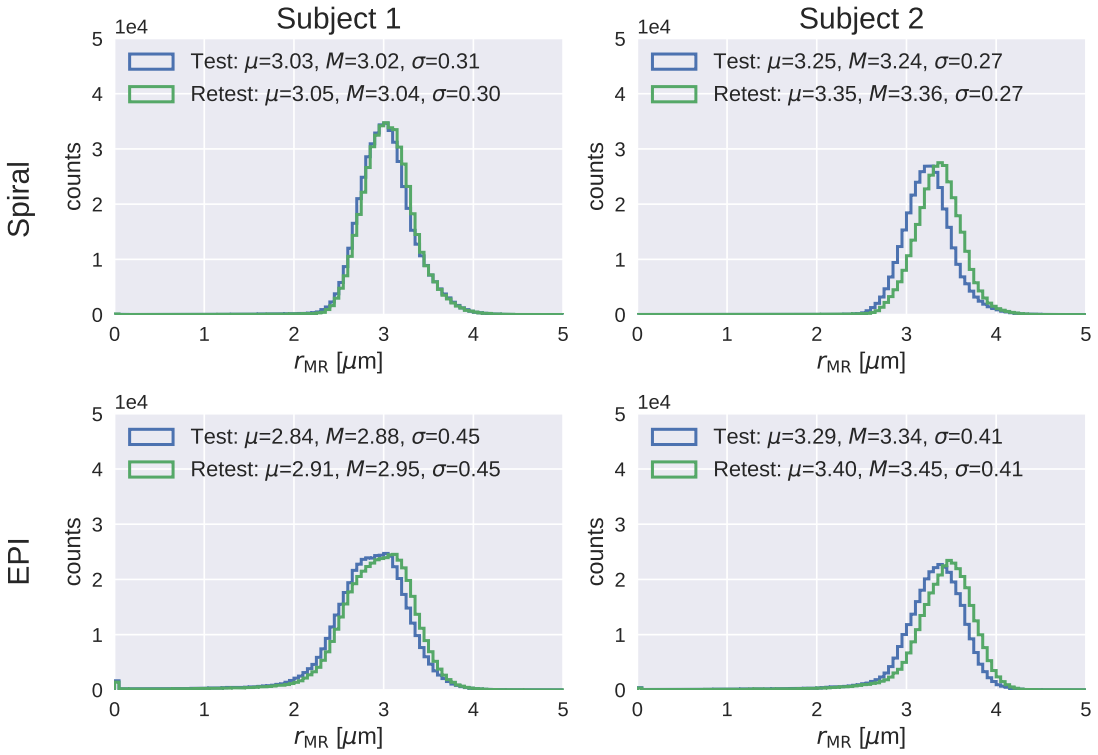

Figure 4.5: Histograms of the MR axon radius (r_{MR}) distributions in white matter of both test and retest measurements for the first two subjects. Mean (μ), median (M) and standard deviation (σ) of the distributions are shown in the legend.

the mean axon radius estimate. In the histograms of MR axon radius estimates in white matter voxels (Appendix Figure A1) this bias is observable as a shift in the axon radius distributions. The sign of the bias was consistent across spiral and EPI data, while the absolute amount of bias was similar in most cases. The variability between test and retest, indicated by the limits of agreement (outer solid lines), was lower by a factor of 1.5–2 in all spiral datasets compared to EPI.

Results for the TRV in the white matter, the corpus callosum and the left CST are shown in Table 4.1. The TRV in the white matter was approximately 1.5–2 times lower in spiral compared to EPI data. It was relatively consistent across all subjects, except for subjects with a high bias, where the TRV was significantly higher. These observations also hold for the corpus callosum, where however, the TRV is higher compared to the whole white matter. In segments of the left CST, the TRV was lower than for the white matter in all cases and lower for spiral data compared to EPI except for subject 6.

Figure 4.8 shows Bland-Altman plots of both repetitions of the test–retest study for subject 7, who was re-scanned to investigate the high bias in the first test–retest measurement. Variability, bias and TRV (Table 4.1) were significantly reduced for both spiral and EPI data in the repeated measurement.

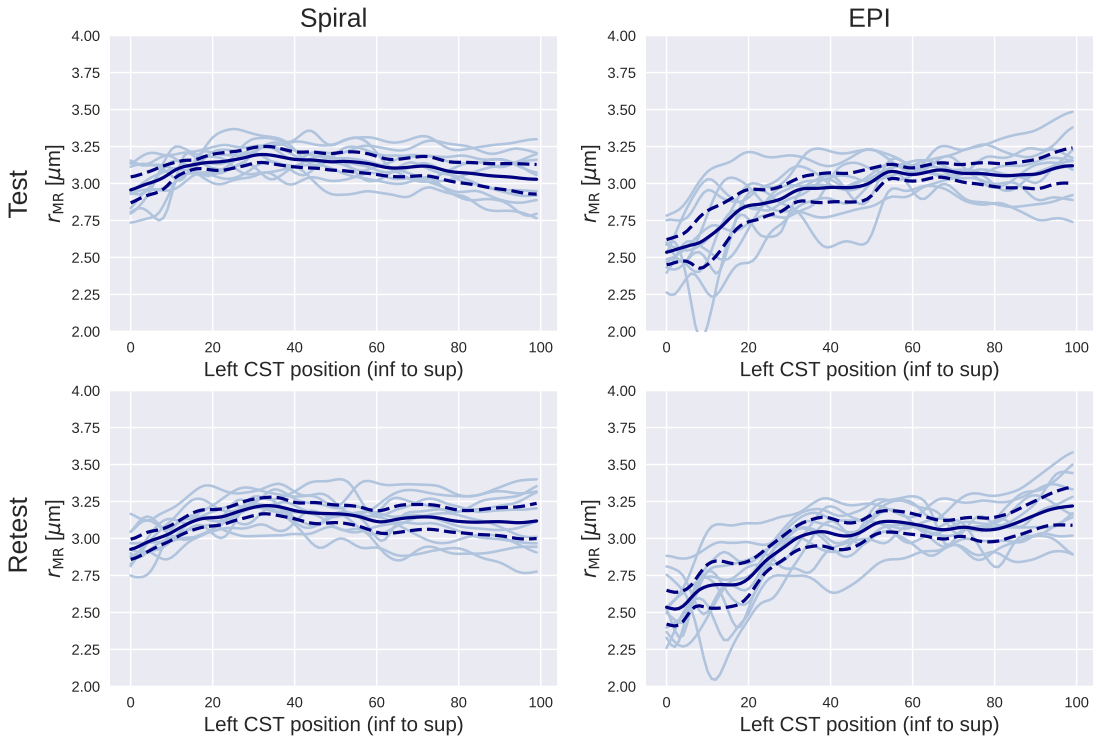

Figure 4.6: Profiles of the estimated axon radius in segments of the left CST from inferior (0) to superior (100) positions. The solid lines represent the mean over all subjects. Dashed lines indicate 95% confidence intervals, calculated as $\pm 1.96 \times \sigma/\sqrt{N}$, where σ is the standard deviation and N the number of subjects. Individual tract profiles are shown as shaded lines.

Subject:	1	2	3	4	5	6	7*	8	9	10
WM Spiral	4.00	4.48	5.23	4.50	5.65	4.41	10.38/5.34	6.07	4.48	7.77
WM EPI	8.83	6.61	11.72	12.00	15.92	9.74	17.67/7.72	9.72	8.92	13.60
CC Spiral	6.06	5.92	9.79	5.88	7.06	6.03	11.98/8.22	5.93	7.31	10.87
CC EPI	14.50	8.70	21.62	12.43	22.39	14.93	23.04/12.11	10.77	14.52	13.41
CST Spiral	1.89	2.16	2.66	2.43	4.71	2.55	4.62/2.72	2.12	3.11	4.04
CST EPI	2.82	3.64	3.74	4.77	6.48	2.05	6.74/3.38	3.32	4.52	4.67

Table 4.1: Test–retest variability [%] in white matter, the corpus callosum (CC) and the left CST of spiral and EPI datasets. The TRV values in white matter voxels obtained for EPI data agree with previously reported values, while the TRV in the left CST is slightly higher than in Ref. [111]. *The test–retest measurement for subject 7 was repeated to investigate the low repeatability in the first measurement.

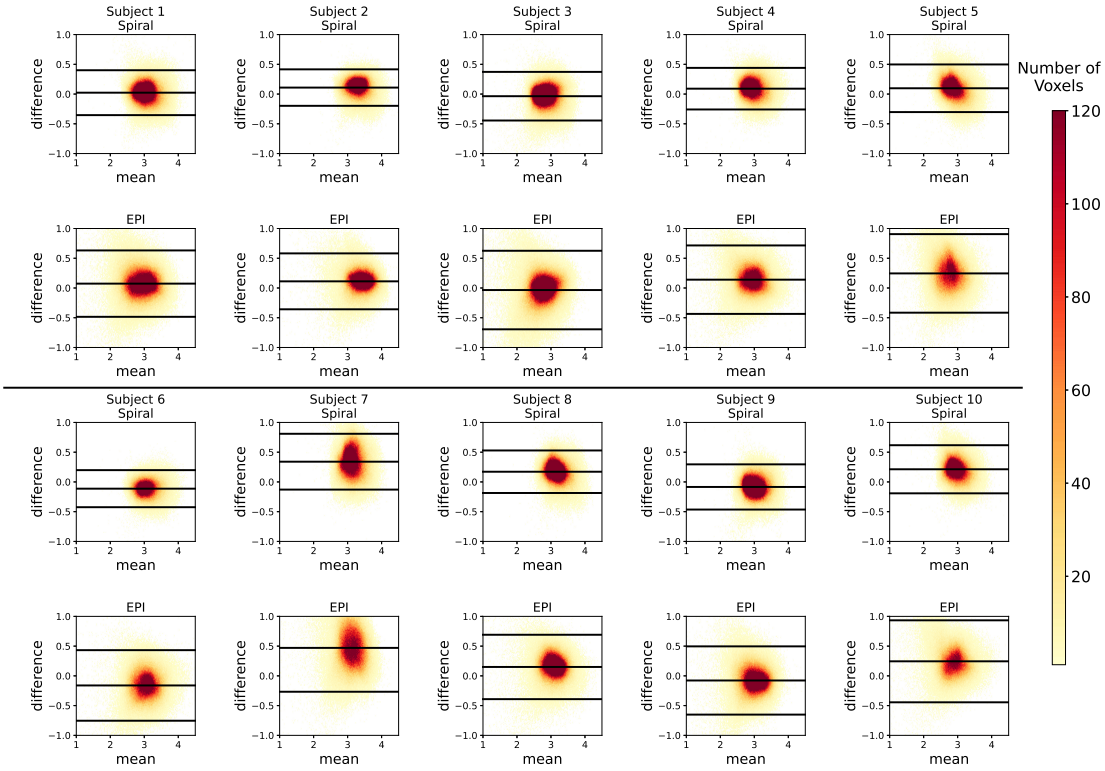

Figure 4.7: Bland–Altman plots of five subjects for all white matter voxels comparing test and retest measurements. Solid lines represent the absolute mean difference and the limits of agreement, calculated as $\pm 1.96 \times \sigma$, where σ is the standard deviation. Bland–Altman plots of all subjects can be found in Appendix Figure A4.

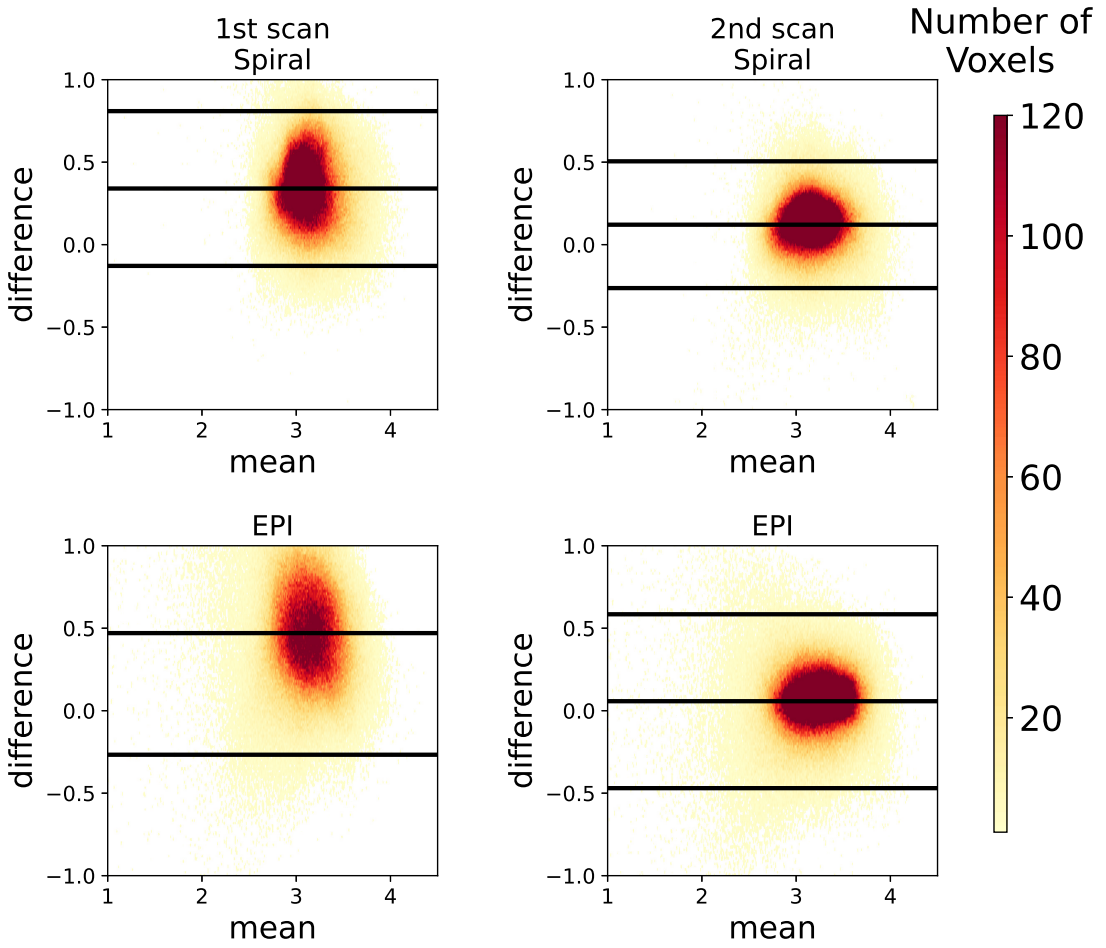

Figure 4.8: Bland-Altman plot of subject 7. The test–retest study for this subject was repeated in a second scan to investigate the large bias in the first scan.

4.4 Discussion

The results presented in the previous section show, that the spiral acquisition leads to more repeatable results compared to the state-of-the-art EPI-based approach. Reduced variability across the brain is observed in both white matter voxels and streamlines along the left CST. This is mainly attributed to the higher SNR due to the lower TE of the spiral readout and reduced artifacts by using field monitoring.

The theoretical SNR gain of the spiral acquisition due to shorter TE and therefore reduced T_2 decay would be around 20%, assuming an intra-axonal $T_2 = 75\,\text{ms}$ [133], [134]. This value was exceeded for both the mean b0 images and the low b-value shell ($b = 6000\,\text{s/mm}^2$). The reduced SNR improvement observed in the high b-value data ($b = 30450\,\text{s/mm}^2$) compared to the lower b-value data could be a result of a suboptimal image reconstruction of the spiral data. The conjugate-gradient method with least squares regularization adds noise to the reconstructed images at each iteration step. It is therefore important to find the optimal stopping point especially under low-SNR conditions [135]. SNR might additionally be affected by the 20% lower readout time of the spirals compared to the EPI readout. Although it is possible to increase the readout time of the spirals, that would result in increased susceptibility-induced artifacts such as blurring. Partial volume effects can be ruled out as a cause of the higher SNR ratio in the mean b0 and lower b-value shell, as similar SNR ratios were observed using a tighter white matter mask (Appendix Table A2).

Spiral and EPI trajectories were designed for the same nominal resolution, but are affected differently by T_2^* decay. The effective resolution is reduced by T_2^* blurring, which has a stronger effect on spirals as outer k-space is acquired later than in EPI [6]. In this study, this is partly compensated by the reduced nominal resolution of the EPI sequence in the phase-encoding direction. Matching the effective resolution would require increasing the nominal resolution of the spirals and therefore a longer readout, resulting in a smaller voxel size and therefore decreased SNR.

EPI based axon radius maps showed more artifacts compared to spiral data, which we mainly attribute to lower SNR and insufficient correction of eddy currents. The eddy current correction with the image-based data-driven approach in “eddy" is limited in the presence of strong diffusion gradients, where low SNR makes registration of diffusion volumes challenging and higher order eddy currents become more significant. The direct measurement of higher order fields leads to improved correction of eddy current induced artifacts [136], [137]. Insufficient correction of eddy currents results in local distortions of the images. The amount of distortion varies with different b-values and diffusion gradient directions. We observed submillimeter spatial shifts between the two shells in powder-averaged images, resulting in voids in the axon radius maps. Less distortion and a higher SNR in spiral images led to lower spatial variation in the estimation of the axon radius. This is especially observable in inferior regions of the brain, where the SNR is lower and the axon radius from EPI data is underestimated compared to that from

spiral data. Existing comparisons in the literature between EPI with and without field monitoring [138], as well as EPI and spiral readouts [6], [139] have shown that while using field monitoring for EPI data does reduce geometric distortions and ghosting, the spiral data shows higher SNR.

Mean axon radius estimates in the white matter (Appendix Figure A1) tended to be higher than previously published results both in the whole white matter and the corpus callosum [111], [140]. Axon radius estimates from spiral data were also on average higher compared to EPI. Two possible confounding factors could have led to these results. First, the Gaussian noise is estimated from strongly diffusion-weighted images with relatively low SNR, which leads to an underestimation of the noise level [141]. This may have resulted in an insufficient correction of Rician bias during spherical averaging. Insufficient bias correction leads to an overestimation of the spherically-averaged signal of the high b-value shell and consequently to lower estimates of the axon radius. This effect is stronger in EPI images, as they have lower SNR. Acquisition of additional data at lower b-value as in Ref. [111] solely used for noise mapping could improve noise estimation, as potential Rician bias in the noise map would be avoided, but also increase scan time. We found only small differences when estimating axon radii from the data acquired in Ref. [111] with noise maps based on lower and higher b-value data, though. The second confounding factor could be insufficient decay of the extra-axonal signal in spiral images due to the lower TE compared to EPI. This effect would lead to an overestimation of the spherically-averaged signal in the lower b-value shell and therefore to higher radius estimates.

Along-tract profiles of the axon radius estimates in the left CST showed lower variability between subjects in the spiral data. The TRV was lower for spiral data compared to EPI, in agreement with the results in the white matter. The EPI data showed a decreasing trend towards inferior regions, which could be caused by the low SNR in this region. The decreasing trend towards superior regions reported in a previous study [111] was not observed in the data. Instead, we observed a decreasing trend towards inferior positions in the EPI data, which we relate to low SNR and artifacts in inferior areas in the EPI data. A possible confounding factor could be the difference in b-value along the tract due to gradient nonlinearities (Appendix Figure A5). A lower b-value at the edges of the tracts could have an impact on the suppression of the extra-axonal compartment. However, the observed difference of the b-value along the tract of less than 3% was relatively small and did not match the pattern of the along-tract profiles.

The test–retest study showed a lower variability in axon radius maps based on spiral data compared to EPI. TRV values were significantly lower for spiral data in white matter voxels, the corpus callosum and the segments along the left CST. The TRV values obtained for the EPI data in white matter agreed with previously reported values, while the TRV in the left CST tended to be slightly higher [111]. The study in Ref. [111] averaged over two repetitions, while we only acquired one repetition, which could explain

the higher TRV.

The lower TRV in white matter of spirals (mean TRV including the repeated participant: 5.66%) compared to EPI (mean TRV: 11.13%) results in smaller sample sizes needed to distinguish between cohorts. An example power analysis (significance level $\alpha = 5\%$, power $1 - \beta = 0.95$) assuming a percentage difference in axon radius estimates of 10% (effect size spiral/EPI: 1.77/0.90) yields sample sizes of 8 (spiral) and 28 (EPI) samples per group (one-sided t-test) [142], [143].

While good repeatability was observed for most subjects, significant bias was apparent in some subjects, indicating a systematic error in the measurement. This bias could potentially arise from the subject, from the data acquisition, or from the image (pre)processing.

Regarding subjects, we found no larger motion in subjects with high bias compared to subjects with low bias. We also observed similar bias in spiral and EPI scans, suggesting a limited impact of subject motion. We found no apparent drift of the diffusion signal intensity during one axon radius measurement (data not shown) [144] and no relation between the bias and the average SNR over the white matter mask. We also investigated whether the off-isocenter position of the subject could be a cause, as gradient nonlinearities of the Connectom scanner increase strongly with increasing distance to the isocenter [145]. The absolute distance from the center of the FOV to the isocenter is shown in Appendix Table A3 for both test and retest, along with the distance between test and retest positions and the observed bias for each subject. However, no relation between the bias and the absolute off-center position or the difference in position between test and retest was found. Repetition of the acquisition for one of the subjects showing strong bias gave a much smaller bias, suggesting that the bias is not inherent to a given subject.

Regarding image processing, different parameter settings for the eddy current and motion correction procedures were tested, none of them having an impact on the bias. We also tried denoising of complex spiral data [119] to reduce the Rician bias before spherical-harmonic calculations, which also did not change the bias. To rule out the possibility that differences in pipeline could cause the bias, the whole image processing pipeline was also tested on a dataset acquired in a previous study [111], where low bias was reported for all subjects studied. The same low bias was obtained using our own pipeline for that data.

Regarding the acquisition, strong bias was seen in both EPI and spiral when it was seen at all. There also seemed to be a connection between strong bias and multiple subjects scanned in one day (but not a connection with just time of day). Together, this suggests that the bias might be due to usage-induced scanner drift. To investigate this, we calculated the percentage difference of the powder-averaged signals between the two sessions for subjects with small, moderate and large bias of the MR axon radius estimates (Appendix Figure A6) and found that the bias mainly resided in the high b-value shell. Gradient instabilities might cause such deviations, as the actual b-value

would then differ from the nominal b-value. Therefore, the test–retest study for subject 7 was repeated in the morning without any prior scanning giving improved results. The bias observed in the first test–retest study would be equivalent to a deviation of the high b-value of around 15%, corresponding to a 7.2% or 20 mT/m difference in gradient amplitude. Such strong instabilities of the gradients would typically not be expected, and may reflect as yet unknown limitations of the scanner hardware when it is pushed to its limits over long durations in the course of a day. It is relevant to note that in the study in Ref. [111], only one or two participants were recorded in a day, and always in the morning (personal communication from Jelle Veraart), which is in line with our observations.

4.5 Conclusions

Combining spiral k-space trajectories with field monitoring improved axon radius mapping in the white matter compared to a state-of-the-art EPI-based approach. The proposed approach both increased SNR and reduced artifacts in the strongly diffusion-weighted images, leading to reduced variability in resulting maps of the effective axon radius.

While the test–retest repeatability was good in most subjects, limited repeatability due to significant bias was found for some subjects after running the protocol multiple times in a day, suggesting that scanner stability could be an issue. This represents a previously unknown limitation of the axon radius mapping protocol which was independent of the readout method used. However, the precise origin of the observed bias requires further investigation.

4.6 Data Availability

The complete image processing and analysis pipeline, as well as the sequence source code and the Pulseq sequence file are available in the Github repository `https://github.com/mrphysics-bonn/AxonDiameter` (DOI: 10.5281/zenodo.10797780). A Docker container including the pipeline as well as example datasets are available in the Github repository.

The source code of the spiral reconstruction pipeline is available at `https://github.com/mrphysics-bonn/python-ismrmrd-reco`.

Chapter 5

Spiral 3DREAM Sequence for Fast Whole-Brain B1 Mapping

Magnetic Resonance in Medicine, 2025;93:321-329
Shared first authorship with co-author S. Niesen

5.1 Introduction

The measurement of the applied RF field (B_1^+) is important for different MRI applications, including accurate scaling of RF power to achieve the desired flip angle [146] and, particularly, quantitative MR imaging [147]. B_1^+ maps are also used on parallel transmit systems for static RF shimming or the calculation of dynamic pTx pulses [148].

The different approaches for the measurement of RF fields can be divided into magnitude- and phase-based methods. Magnitude-based methods include the (saturated) dual-angle B_1^+ mapping method based on a GRE acquisition [149], [150], the actual flip-angle-imaging (AFI) method [49], and the RF-prepared 3D FLASH acquisition [151]. The phase-sensitive method developed by Morell [152] and B_1^+ mapping based on the Bloch-Siegert shift (BSS) [48] are examples for phase-based methods. Several approaches for flip angle mapping are based on a stimulated echo (STE) signal [153]–[157]. One of these approaches is the dual refocusing echo acquisition mode (DREAM) sequence [157], which consists of a STEAM preparation, followed by a low-angle imaging pulse train acquiring two signals - the free induction decay (FID) and the virtual stimulated echo (STE*). Separating B_1^+ and spatial encoding weakens the specific absorption rate (SAR) burden and the quasi-simultaneously measurement of the two signals accelerates the scan and allows for volumetric B_1^+ mapping [50], [157]. The volumetric DREAM sequence [50] uses slice-selective pulses both for the STEAM preparation and for the imaging train and an interleaved slice acquisition order. Recently, DREAM has been extended to the 3DREAM sequence with a 3D readout [158] allowing for rapid whole-brain B_1^+ mapping. In the 3DREAM sequence, a single STEAM preparation with non-selective block pulses is applied before the 3D Cartesian imaging train. As a result, the STE* signal decreases as it is 'consumed' with each excitation, whereas the FID signal evolves towards a steady state [158]. The STE* decay is mainly determined by the excitation flip angle, the number of total excitations (echo train length - ETL), T_1 and TR [158] and can result in strong blurring leading to artifacts in resulting flip angle maps. One solution to compensate for the different evolution of FID and STE* signals, is to apply a filter on the FID images to align blurring levels [158], however decreasing the effective resolution.

The approach used in this work is based on the 3DREAM sequence and differs in terms of k-space acquisition in the imaging train. Instead of a Cartesian two phase encoding order, a non-Cartesian 3D stack-of-spirals readout is used to acquire the STE* and FID signals. Non-Cartesian k-space acquisition with spiral k-space trajectories benefits from short scan duration compared to conventional spin-warp sequences [159]. This advantage is used for the 3DREAM sequence to decrease the ETL and counteract the fast decay of the STE* signal [158] for reduced blurring and a higher effective resolution of B_1^+ maps.

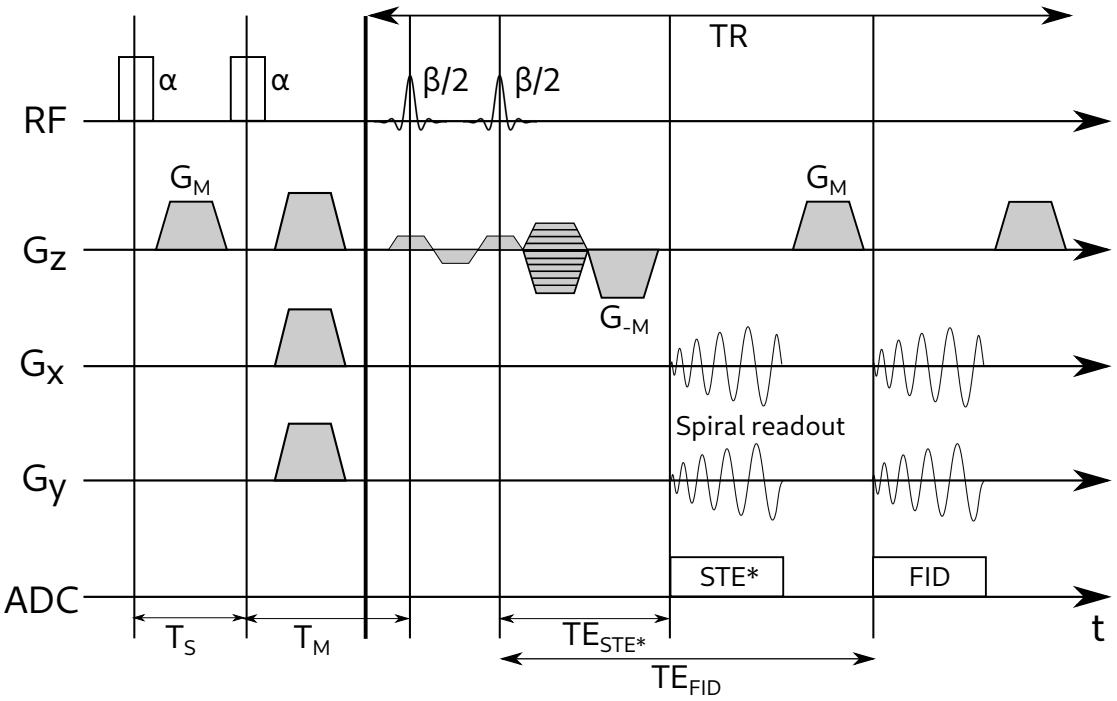

Figure 5.1: The spiral 3DREAM sequence starts with a STEAM preparation sequence with non-selective block pulses (flip angle α) followed by a spiral imaging train. Here, T_{S} is the STEAM preparation pulse interval and T_{M} is the mixing time. Fat saturation before the STEAM preparation (not shown) and binomial (1-1) pulses (flip angle β) at the beginning of the spiral imaging train are used to suppress fat signal. The gradients G_{M} and $G_{\text{-M}}$ have equal absolute gradient moments with opposite sign leading to a separation of the two signals in k-space. In the sequence utilized at the scanner, the phase encoding gradient, the second slab selection rephaser and the gradient $G_{\text{-M}}$ were merged into one gradient.

5.2 Methods

5.2.1 Implementation of Spiral 3DREAM

Figure 5.1 shows the spiral 3DREAM sequence. The STEAM preparation is the same as in the original Cartesian 3DREAM [158] using two non-selective block pulses. Fat saturation before the first STEAM preparation pulse (not shown) and two slab-selective binomial pulses for water-specific excitation [160] are used to reduce chemical shift artifacts.

The STE* signal is dephased by the first gradient G_{M} on the slice axis. The gradient $G_{\text{-M}}$ has the same absolute gradient moment with opposite sign and thus rephases the STE* signal, while dephasing the FID signal:

$$\int G_{\mathrm{M}}\,\mathrm{d}t = -\int G_{\text{-M}}\,\mathrm{d}t. \tag{5.1}$$

The FID signal is rephased with the second gradient G_{M}. G_{M} and $G_{\text{-M}}$ are further referred to as 'signal separation gradients'. In contrast to the original 3DREAM, these gradients were applied along the slice direction to reduce eddy current effects on the

spiral trajectory.

The STE* and FID signals were acquired with an accelerated 3D stack-of-spirals readout. Since the STE* and FID had the same effective TE, the flip angle quantification was T_2 compensated [50]. A dual-echo GRE reference scan was acquired before the spiral 3DREAM to calculate coil sensitivity and B_0 field maps. The spiral 3DREAM was implemented in Pulseq [78], [87].

5.2.2 Reconstruction

Reconstruction was done with an iterative SENSE reconstruction [67] using the PowerGrid toolbox [96]. The reconstruction included a time-segmented B_0 correction [73] with the B_0 map calculated from the dual-echo GRE reference scan. Coil sensitivity maps were calculated from the first echo of the reference scan with the ESPIRiT algorithm [58]. Image reconstruction was implemented as part of an open-source imaging workflow [112].

To equalize blurring due to different signal evolution of STE* and FID, the FID images were filtered after reconstruction using a global filter as proposed in Ref. [158].

5.2.3 Phantom Experiments

All measurements were performed on a MAGNETOM 7T Plus scanner (Siemens Healthineers AG, Forchheim, Germany) with a 32-channel receive, single-channel transmit coil (Nova Medical) on a homogeneous phantom [161] (Appendix Table A4). Flip angle maps were acquired with the spiral and Cartesian 3DREAM at an isotropic resolution of 5 mm (FOV: $200 \times 200 \times 200\,\mathrm{mm}^3$). The dual-angle method (DAM) [149], the BSS method [48] and an AFI sequence [49] were used as reference methods.

The spiral 3DREAM data were acquired in transversal orientation with flip angles $\alpha = 50\,^\circ$ and $\beta = 5\,^\circ$ ($\mathrm{TE}_{\mathrm{STE}^*} = 0.72\,\mathrm{ms}$, $\mathrm{TE}_{\mathrm{FID}} = 4.28\,\mathrm{ms}$). The spiral readout consisted of one interleaf per partition with an in-plane acceleration of $R_{\mathrm{int}} = 5$ and without additional acceleration in phase-encoding direction ($R_{\mathrm{Ph}} = 1$). A controlled aliasing in parallel imaging results in higher acceleration (CAIPIRINHA)-shift of $\delta = 4$ was applied [162] by using different sets of spiral interleaves in subsequent partitions (partition 1: first interleaf, partition 2: fifth interleaf, etc.). The ETL was 40 and the acquisition time (TA) excluding the reference scan was 0.33 s. The reference scan was acquired at the same FOV and resolution as the spiral scan. All sequence parameters can be found in Appendix Table A5.

The Cartesian 3DREAM data was acquired in sagittal orientation with non-selective pulses in the imaging train ($\mathrm{TE}_{\mathrm{STE}^*} = 1.06\,\mathrm{ms}$, $\mathrm{TE}_{\mathrm{FID}} = 2.26\,\mathrm{ms}$). An acceleration factor of $R = 2 \times 2$ in phase encoding directions led to an ETL of 400 and TA of 1.33 s. A CAIPIRINHA-shift of $\delta = 1$ was applied (implemented as in Ref. [158]). Flip angles α and β were the same as in the spiral sequence. Compared to the original 3DREAM [158],

a spoiling moment was added to the signal separation gradients in readout direction to better separate STE* and FID signals (Appendix Figure A7).

AFI flip angle maps were obtained using a flip angle of 50 °, an acceleration factor of $R = 2$, $\mathrm{TR}_1 = 20\,\mathrm{ms}$, $\mathrm{TR}_2 = 100\,\mathrm{ms}$, $\mathrm{TE} = 0.97\,\mathrm{ms}$ and $\mathrm{TA} = 80\,\mathrm{s}$. The BSS sequence acquired two images with $\pm 5\,\mathrm{kHz}$ offresonant Fermi pulses (peak $\mathrm{B}_1^+ = 7.72\,\mu\mathrm{T}$), an imaging flip angle of 20 °, $\mathrm{TE} = 6.25\,\mathrm{ms}$ and $\mathrm{TR} = 100\,\mathrm{ms}$. For the DAM, two 3D-GRE scans with flip angles 60 ° and 120 ° were acquired. $\mathrm{TE} = 0.95\,\mathrm{ms}$ and $\mathrm{TR} = 4\,\mathrm{s}$ were chosen to allow for almost full relaxation considering $\mathrm{T}_1 = 840\,\mathrm{ms}$ of the phantom. Both scans resulted in $\mathrm{TA} = 42\,\mathrm{min}$.

Flip angle maps of both 3DREAM sequences were compared with the reference methods using scatterplots, Pearson correlation coefficients and a linear fit for which the root-mean-square error (RMSE) was calculated. A centrally located sphere with a radius of ten voxels was selected as the region of interest, as signal dropouts were observed outside this sphere due to the high dynamic range of B_1^+ in the phantom [161]. All flip angle maps were registered to the magnitude image of the AFI sequence using FSL FLIRT [120] and a brain mask [163] followed by an eroding kernel, which was applied onto the maps.

To investigate the impact of acceleration on the flip angle maps obtained from the spiral 3DREAM, a non-accelerated spiral scan was acquired (ETL: 200). The non-accelerated scan was additionally executed with a segmented acquisition to keep the ETL per segment the same as in the accelerated scan. The segmented version consisted of five segments each with an own STEAM preparation and a waiting time of 3 s inbetween segments to allow for relaxation.

The repeatability of B_1^+ mapping with the accelerated spiral 3DREAM sequence was investigated by repeating the measurement in a second scan session on a different day (test–retest). The intraclass correlation coefficient (ICC) [164] for two-way mixed effects, single raters, was calculated and a Bland-Altman plot along with the reproducibility coefficient (RC) and the coefficient of variation (CV) was created to evaluate the repeatability of flip angle maps in test and retest measurements.

5.2.4 In Vivo Experiments

In vivo data were acquired with both 3DREAM sequences and the AFI sequence from five healthy volunteers (three male, two female, age between 24–48) after giving informed consent. The DAM and BSS were not performed in vivo. For the DAM the acquisition time was too high, making it susceptible to motion, and for the BSS the energy of the offresonant pulses was too low for accurate flip angle mapping due to SAR constraints.

Data were acquired at 5 mm and 3 mm isotropic resolution. The parameters of the scan at 5 mm resolution were the same as for the phantom experiments, but one interleaf with $R_{\mathrm{int}} = 6$, $R_{\mathrm{Ph}} = 1$ and $\delta = 5$ were chosen ($\mathrm{TE}_{\mathrm{STE}^*} = 0.72\,\mathrm{ms}$, $\mathrm{TE}_{\mathrm{FID}} = 3.96\,\mathrm{ms}$, $\mathrm{ETL} = 40$, $\mathrm{TA} = 0.30\,\mathrm{s}$). The scan at 3 mm resolution had a FOV of $216 \times 216 \times 216\,\mathrm{mm}^3$.

The spiral sequence parameters were: $TE_{STE^*} = 0.88\,ms$, $TE_{FID} = 6.28\,ms$, ETL = 72, TA = 0.87 s. The resolution of the spiral reference scan was limited to 4.32 mm to not excessively increase scan time. The acceleration of the Cartesian 3DREAM was increased to $R = 2 \times 4$ with $\delta = 2$ to decrease the ETL ($TE_{STE^*} = 1.25\,ms$, $TE_{FID} = 2.5\,ms$, ETL = 648, TA = 2.39 s). All other parameters of both 3DREAM sequences were kept the same as for the 5 mm in vivo scan. The parameters of the AFI sequence were kept the same as in the phantom experiments except for TE = 1.10 ms, resulting in TA = 4 min for the scan with 3 mm resolution. To investigate the effect of blurring in the STE* image, FID images of both 3DREAM sequences were reconstructed with and without the global filter and the high frequency error norm (HFEN) was calculated [165]. The global filter was applied onto synthesized k-space data as it describes the STE* decay and blurring of both 3DREAM sequences was compared with the FWHM of the reconstructed point object for 3 mm and 5 mm.

We observed different artifacts especially in the STE* images of the Cartesian and spiral 3DREAM depending on the moment and orientation of the signal separation gradients. Therefore, we acquired (a) the spiral 3DREAM with these gradients either in slice (G_z) or in one of the readout directions (G_x) and (b) the Cartesian 3DREAM with and without the spoiling moment added to the gradients (Appendix Figure A7). Changing the signal separation gradients, required a slight adjustment of the timing parameters (spiral 3DREAM: label '5 mm (RO)' in Appendix Table A5; Cartesian 3DREAM: $TE_{STE^*} = 1.37\,ms$, $TE_{FID} = 2.46\,ms$).

Flip angle maps of the 3DREAM sequences and the AFI were compared as in the phantom experiments.

5.3 Results

Figure 5.2 shows flip angle maps of one coronal and transversal slice in the phantom's center. The Pearson correlation coefficients and the linear fits indicate high agreement of both 3DREAM sequences with the reference methods. The slope of the linear fits of the spiral 3DREAM was higher compared to the Cartesian 3DREAM for all comparisons, however, in the AFI comparison, the RMSE was slightly increased for the spiral 3DREAM. For both 3DREAM sequences, but enhanced for the spiral 3DREAM, the coronal image contained a region with increased blurring at the bottom of the phantom, where low flip angles were observed.

Appendix Figure A8 shows the results for the non-accelerated, accelerated and non-accelerated segmented spiral scans. The accelerated scan had a similar Pearson correlation coefficient and RMSE, but higher slope in the comparison with the AFI as the non-accelerated segmented scan. An artifact (white arrow) was observed at the bottom of the phantom in the accelerated scan. The non-accelerated non-segmented scan showed significantly stronger blurring compared to the accelerated and segmented scans and underestimated high flip angles when compared to the AFI. The results of the spi-

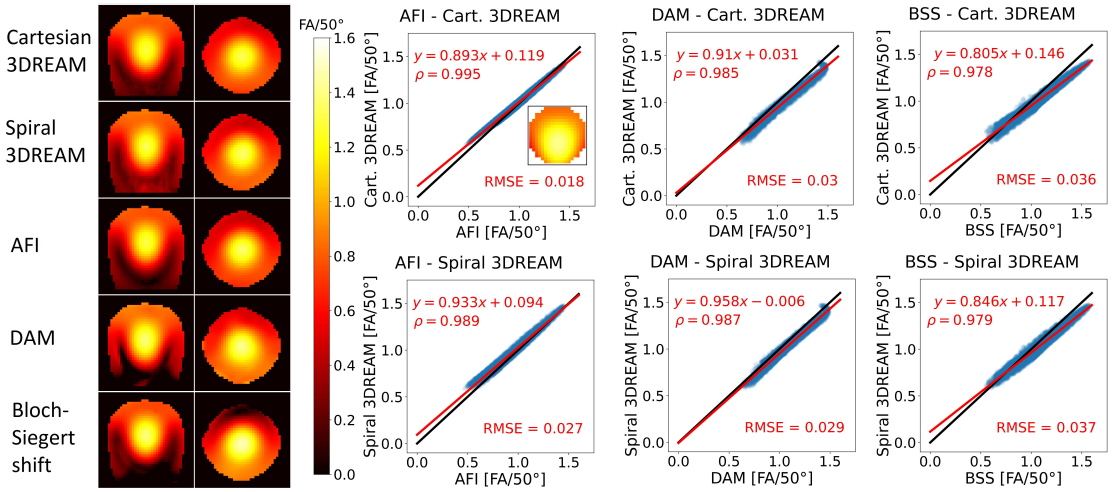

Figure 5.2: Left: Flip angle maps of the 3DREAM sequences, the AFI, the DAM and the BSS with an isotropic resolution of 5 mm for one coronal and one transversal slice. Right: Scatterplots comparing flip angle maps of the 3DREAM sequences to the three reference methods. The linear fit is shown as a red line alongside with the fit parameters and correlation coefficients ρ. The black line is the identity. A sphere, centered in the middle of the phantom and with a radius of ten voxels is selected for the comparison. The selected region for the comparison is shown in the inset of the first scatterplot.

ral 3DREAM test-retest measurements are shown in a Bland-Altman plot (Appendix Figure A9). The plot demonstrates larger differences at lower angles and an absolute mean difference close to zero. The ICC (0.993), RC (3.139 °), and CV (5.426 %) imply excellent test-retest reliability.

Figure 5.3 shows flip angle maps of one subject at 3 mm and 5 mm resolution acquired with the AFI and both 3DREAM sequences and the corresponding scatterplots. Overall, the flip angle distribution was similar for all three sequences with larger flip angles in the center of the brain and lower flip angles present in peripheral parts of the brain. 3DREAM flip angle maps at both resolutions showed some ventricular contrast, which was more pronounced in the Cartesian 3DREAM and stronger at 3 mm resolution compared to 5 mm resolution. The high agreement of both 3DREAM sequences with the AFI was reflected in high correlation coefficients and low RMSE (Table 5.1). Both 3DREAM sequences performed similarly, however the spiral 3DREAM had a slope closer to one and lower intercepts. A slight systematic underestimation at high flip angles ($> 50\,°$, dashed line) was most visible for the Cartesian 3DREAM at 5 mm resolution.

Figure 5.4(I) shows in vivo STE* and FID images of both 3DREAM sequences, acquired at an isotropic resolution of 3 mm. The contrast of both STE* and FID was different between the two 3DREAM sequences due to the difference in TE. In the spiral data the white to gray matter contrast was higher in FID images compared to the Cartesian sequence. Blurring in spiral STE* images was less pronounced than in Cartesian STE* images. This becomes apparent comparing the filtered FID images, where the blurring levels were aligned to the STE* images and comparing the HFEN: (Cartesian: 0.805, spiral: 0.386). The global filter did not alter the spiral FID signal as strong as the

#	age	gender	slope		intercept		ρ		RMSE	
			C-A	S-A	C-A	S-A	C-A	S-A	C-A	S-A
1	24	f	0.91	0.96	0.09	0.03	0.98	0.97	0.03	0.04
			0.87	0.91	0.10	0.07	0.98	0.98	0.03	0.03
2	28	m	0.86	0.91	0.09	0.03	0.97	0.96	0.03	0.03
			0.84	0.84	0.12	0.12	0.96	0.96	0.03	0.04
3	26	m	0.86	0.87	0.10	0.08	0.97	0.97	0.03	0.03
			0.81	0.84	0.17	0.16	0.97	0.97	0.03	0.03
4	48	f	0.85	0.86	0.10	0.07	0.98	0.97	0.03	0.03
			0.83	0.84	0.14	0.12	0.97	0.97	0.03	0.03
5	41	m	0.96	0.98	0.03	-0.02	0.98	0.97	0.03	0.03
			0.86	0.94	0.13	0.05	0.98	0.98	0.03	0.03

Table 5.1: Subject information including the subject number (#), age, gender (f: female, m: male) and the results of the linear fit for the comparison of Cartesian 3DREAM and AFI (C-A) and spiral 3DREAM and AFI (S-A) are shown for all five subjects. Listed are the slope and the intercept of the fit, the Pearson correlation coefficient ρ and the RMSE for 3 mm resolution in the first row of each subject and 5 mm resolution in the second row accordingly.

Cartesian FID. At 5 mm resolution the blurring was decreased (Appendix Figure A10, HFEN: Cartesian: 0.639, spiral: 0.100). These observations meet the lower FWHM of a global filtered point object for the spiral 3DREAM compared to the Cartesian 3DREAM (Appendix Figure A11(c)).

Figure 5.4(II) presents results with and without modified signal separation gradients at 5 mm resolution. Ring-shaped artifacts (red arrows) in readout direction (yellow arrows) appeared in the STE* images without modification of the signal separation gradients. For the Cartesian 3DREAM, the artifact was located at the top of the head (a) and for the spiral 3DREAM, it was located near the ear region (b). These artifacts were not visible in the FID images, but translated to the flip angle maps.

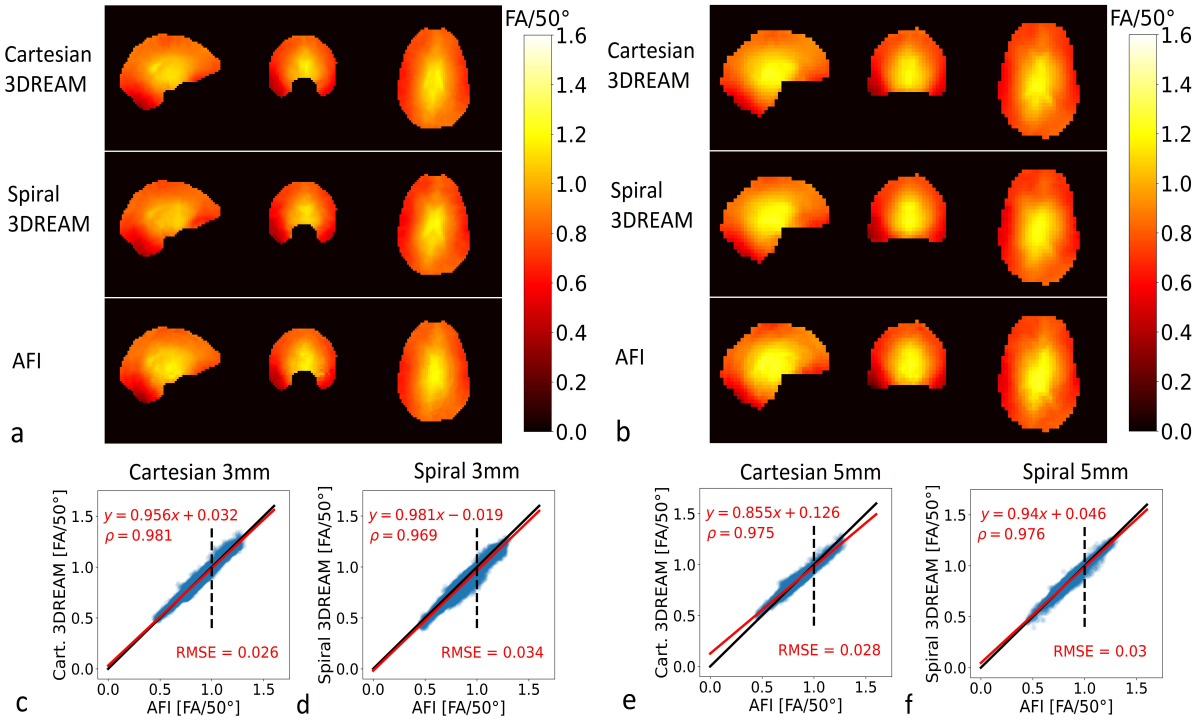

Figure 5.3: Top row: Normalized flip angle maps of subject 5 at (a) 3 mm and (b) 5 mm resolution from the Cartesian 3DREAM at the top, the spiral 3DREAM in the middle and the AFI in the bottom row. One central slice for each view (sagittal, coronal and transversal) is presented. Bottom row: Linear fits for the comparison of the masked flip angle maps with normalized axes for 3 mm (c-d) and 5 mm (e-f) resolution. The linear fit is shown as a red line alongside with the fit parameters and correlation coefficients ρ. The black line is the identity. In addition, the dashed line marks the flip angle 50 ° and thus the beginning of the underestimation at higher flip angles.

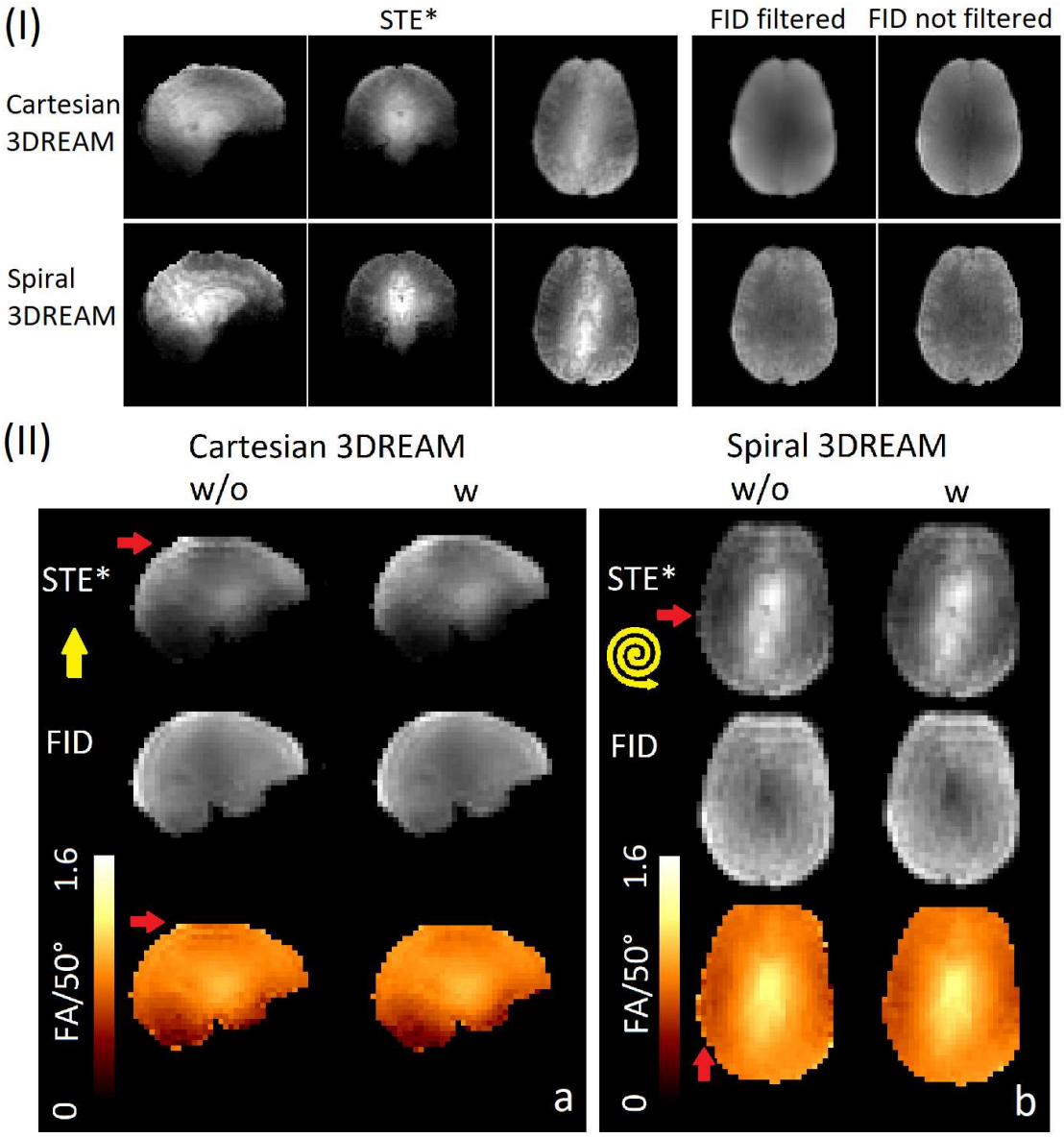

Figure 5.4: (I) One sagittal, coronal and transversal slice of the STE* at 3 mm resolution is shown for both Cartesian (top) and spiral (bottom) 3DREAM sequences. Additionally, the transversal slice of the FID is displayed on the right, with and without the FID filter applied. (II) (a) Sagittal STE* and FID images at 5 mm resolution as well as normalized flip angle maps of the Cartesian 3DREAM sequence without (w/o) and with (w) modified signal separation gradients. The red arrows point to the ring-shaped artifacts in the STE* images and in the flip angle maps. The yellow arrow indicates the readout direction. (b) The same results are shown for the spiral sequence, but a transversal slice is displayed as the readout direction differs from the Cartesian sequence. All images were obtained from subject 5.

5.4 Discussion

The results demonstrate accurate B_1^+ quantification with the spiral 3DREAM sequence with high statistical agreement to reference sequences, here the AFI, DAM and BSS. In phantom experiments, the reduction of the ETL in the spiral 3DREAM compared to the Cartesian 3DREAM, combined with one spiral interleave in-plane, led to an increased slope of the fit, indicating less underestimated flip angles due to less filtering of STE* near the *k*-space center [50]. As demonstrated in Appendix Figure A11(b), the trajectory led to reduced blurring. The small RMSE differences of the 3DREAM sequences originate mostly from voxels with lower flip angles. As demonstrated in the Bland-Altman plot, the computation precision decreases at low STE* signal. The registration partly smoothes these regions leading to small RMSE differences of the 3DREAM sequences.

The results from the phantom experiment with the accelerated, non-accelerated and non-accelerated segmented version of the spiral sequence justify the choice of the acceleration factor. Results from the accelerated scan were close to results of the non-accelerated segmented version, except for an artifact in a low-SNR region. Additionally, TA of the segmented scan increases due to waiting time between segments [158]. The long ETL combined with five in-plane interleaves of the non-accelerated non-segmented scan resulted in significantly increased blurring and underestimated high flip angles as less signal was present in *k*-space. The test-retest demonstrated high repeatability and a lack of systematic errors.

The flip angle maps of the 3DREAM and AFI were in high agreement in vivo as well. In Ref. [50] and [158], the observed ventricular contrast is attributed partly to tissue properties, but also to an increased T_1 and T_2 decay of the STE*. As can be seen in Appendix Figure A11(c), the spiral 3DREAM leads to less STE* decay compared to the Cartesian 3DREAM, explaining the reduced ventricular contrast, especially at 3 mm resolution. Due to the lower ETL, the 5 mm flip angle maps suffered less from the STE* decay, but both 3DREAM sequences performed well also at 3 mm resolution. Due to less STE* signal filtering near the *k*-space center, the slope of the spiral 3DREAM fit is increased, indicating a lower flip angle underestimation [50]. As in the phantom experiments, the spiral 3DREAM shows a slightly higher RMSE than the Cartesian 3DREAM after registration. Despite using six interleaves, the higher TE of the spiral 3DREAM increases the RMSE in regions with lower T_2^*, but only to a small extent. Using more interleaves would decrease TE, but increases ETL leading to more STE* blurring. Higher acceleration decreases blurring, but is limited by coil sensitivities and decreased SNR.

As demonstrated in Ref. [158], applying the correct global filter on the FID eliminates erroneous flip angles at the edge of the brain. The flip angle maps demonstrate equalized blurring for both contrasts using the global filter for the spiral 3DREAM as presented for the Cartesian 3DREAM in Ref. [158]. As the ETL was significantly shorter in spiral acquisitions, a much weaker filter was needed, which increased the effective resolution of

the flip angle maps. Both the TR and the ETL are essential parameters determining the blurring in the images, however as can be seen in Appendix Figure A11(c), the impact of the shorter ETL of the spiral 3DREAM leads to a stronger blurring reduction than the reduced TR of the Cartesian 3DREAM.

The observed ring-shaped artifacts in STE* images and flip angle maps, are attributed to folding of FID and STE* signals in k-space. Particularly, the dominant FID signal folds into the STE* signal. Applying the signal separation gradients of the spiral 3DREAM in slice direction instead of in readout direction led to a better separation of the FID and STE* k-spaces. This also reduced eddy current effects of the spoilers on the spiral readout, as cross-responses from other gradient axes are typically small [166]. The improved separation of k-spaces with an additional spoiling moment in the Cartesian 3DREAM reduced artifacts in a similar way.

The RF-prepared 3D FLASH method [151] has a wider dynamic range and includes correction for ventricular contrast. Similar to 3DREAM it acquires whole brain flip angle maps in seconds, however, it requires two shots, which increases motion sensitivity. In contrast, 3DREAM acquires both contrasts in one shot.

5.5 Conclusions

An extension of the 3DREAM sequence with a stack-of-spirals readout was presented. The spiral 3DREAM produced comparable B_1^+ mapping results to the existing Cartesian 3DREAM and to other established methods such as AFI. Comparing the 3DREAM sequences, the Cartesian 3DREAM with its shorter TE is more robust against low T_2^* regions than the spiral 3DREAM. However, the reduced ETL of the spiral 3DREAM leads to less filtering of high k-space frequencies, reducing the blurring in all encoding directions and the ventricular contrast. This allows for a higher effective resolution and also reduces filtering near the k-space center, reducing underestimation of high flip angles.

5.6 Data Availibility

The sequence designed with Pulseq can be found in the following openly available Github repository: `https://github.com/mrphysics-bonn/spiral3dream/tree/mrm_v3` (DOI: 10.5281/zenodo.13304406).

Chapter 6

Whole-brain Diffusion-Weighted Imaging at 7T with Multiband pTx Pulses and Field Monitoring

This chapter presents preliminary results and is partly based on abstracts presented at the ESMRMB 2023 and ESMRMB 2024 conferences. The GRAPE pulse design, the kT-Spokes pulse design (except for the VERSE gradients) and the pulse simulations presented in section 6.2.1 of this chapter were done by the co-author of these abstracts D. Löwen.

6.1 Introduction

Diffusion-Weighted Imaging (DWI) plays a crucial role in characterizing tissue microstructure, particularly in neuroscientific research. Diffusion-weighted images are the basis for signal representations as the diffusion tensor in Diffusion Tensor Imaging (DTI) [18] enabling voxel-wise quantification of diffusion anisotropy. Moreover, diffusion-weighted images serve as the foundation for advanced techniques such as fiber tractography [26], [167] and the development of specific tissue models [168].

DWI has intrinsically low signal-to-noise ratio (SNR), as its contrast mechanism is based on signal cancellation due to the diffusion of water molecules. One way to increase SNR is to acquire DWI data at ultra-high field strengths [7]. Nevertheless, 3T remains the preferred field strength for DWI in neuroscientific research, largely due to the challenges posed by ultra-high field strengths [53]. These challenges include increased B_0 and B_1 inhomogeneity as well as shorter T_2 and T_2^* relaxation times.

Lower T_2 relaxation times in white matter, which is the most investigated region in DWI, from 3T ($T_2 \approx 77\,\text{ms}$) to 7T ($T_2 \approx 50\,\text{ms}$) [169] decrease SNR gains due to the higher field strength depending on the echo time. Therefore, at ultra-high field it is beneficial to use k-space trajectories with short echo times such as spirals that can improve SNR compared to typically used EPI trajectories [6], [139]. Lower T_2^* relaxation times lead to faster signal decay during readout, which mostly affects outer k-space and therefore results in lower effective resolutions.

Inhomogeneity of the B_1 transmit field causes signal dropouts especially in lower brain areas as the cerebellum. At ultra-high fields, B_1 inhomogeneity is typically tackled by using parallel transmit (pTx) techniques. Both static B_1 shimming and dynamic pTx pulse design have been shown to improve B_1 homogeneity in DWI acquisitions [170], [171]. However, application of these techniques has not been shown for multiband acquisitions yet, which is crucial for time-efficient whole-brain DWI. Multiband pTx pulse design for spin-echo DWI is challenging, as typically large flip-angle slice-selective excitation and refocusing pulses are used. In this chapter, first results with multiband pTx pulses are shown. PTx pulses were designed with the kT-spokes [172], [173] and Gradient Ascent Pulse Engineering (GRAPE) [174], [175] concepts. The optimized pTx pulses are compared to standard circularly polarized (CP) mode pulses.

Increased static B_0 inhomogeneity at ultra-high field strengths leads to increased signal dropout, image distortion and blurring. Static inhomogeneity together with dynamic field inhomogeneities stemming from strong diffusion gradients causes significant degradation of DWI images. Image-based [110], [115] as well as k-space based corrections [9] based on magnetic field monitoring [8] have been proposed to mitigate these effects. In this chapter, EPI and spiral data reconstructed with field monitoring data and a higher order image reconstruction algorithm [9] are compared to standard image reconstruction with image-based off-resonance and eddy current correction.

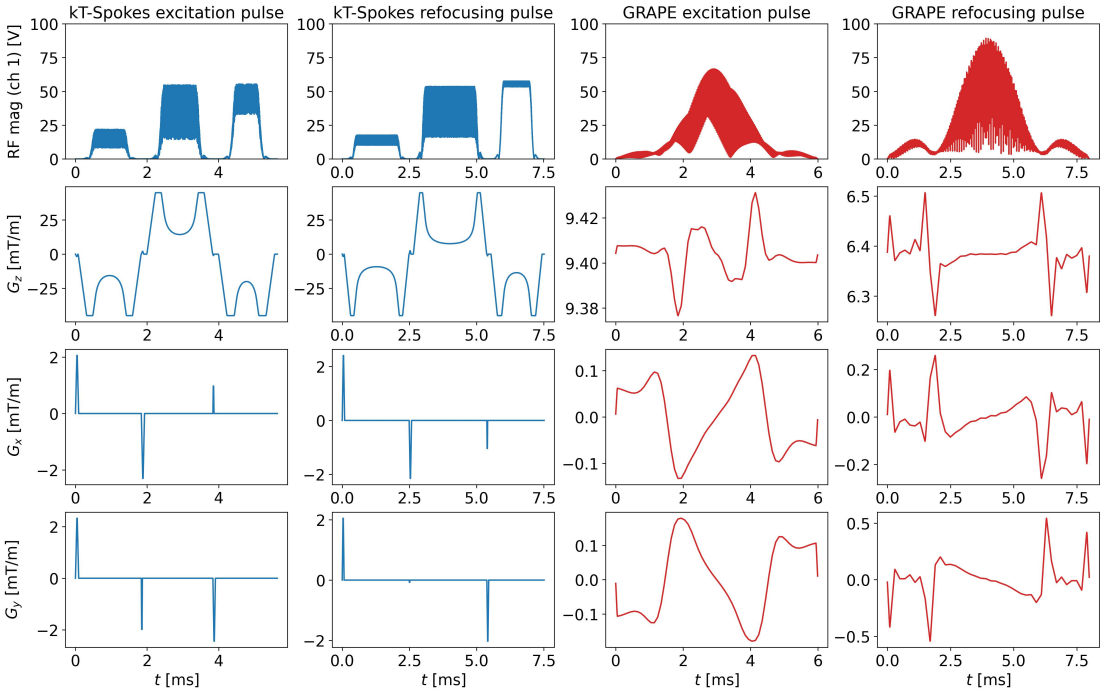

Figure 6.1: Left: Multiband kT-spokes excitation and refocusing pulses of one slice group. The magnitude of the first RF channel is displayed in the top row. Below, the slice-selective VERSE-gradients (on G_z axis) and the kT-point blips (on all axes) are shown. G_x and G_y axes are scaled down for improved visibility. Right: Multiband GRAPE excitation and refocusing pulses of the same slice group. The magnitude of the first RF channel and the optimized GRAPE gradients are shown. Note the different scaling of the G_z axis as the slice gradient is superimposed on the GRAPE gradients.

6.2 Methods

6.2.1 PTx Pulse Design

All pulses were optimized on a database of B_1 and B_0 maps using the universal pulse concept [51] rather than using subject-specific optimization during the scan session. Universal pulses do not require additional computation time or dedicated calibration sequences in the scan session, which makes them advantageous especially for computationally intensive slice-individual pulse optimization.

6.2.1.1 kT-Spokes Pulses

In the first step of kT-spokes pulse design [172], an asymmetric non-selective kT-points pulse (three kT-points) was optimized for homogeneous excitation (and refocusing) of the whole head across a database of 10 subjects. Based on this, specific pulses per slice position were further optimized through weights, that exponentially decreased with distance d to the slice center by a factor of $e^{-d/10\text{mm}}$. In this second optimization stage, the kT-points gradient blips were kept unchanged and the result was still a non-selective pulse per slice [172]. Since every pulse is finally optimized for a certain slice within the

head, the top of each head in the database was taken as a reference point to align the slice positions across different subjects.

The two-stage optimized non-selective pulses were then converted to slice-selective bipolar kT-spokes pulses by replacing the rectangular RF shape with a sinc shape yielding the same flip angle and adding slice-selection gradients [173]. Minimum-time variable-rate selective excitation (VERSE) [66] was applied to the pulses to decrease SAR. The total duration of the pulses was kept approximately constant before and after the application of VERSE.

In the last step, multiband pulses were created by superposition of the single-band pulses. Examples for resulting multiband excitation and refocusing pulses are shown in Figure 6.1. The time-bandwidth products (tbp) of the three sub-pulses were 3.0 with sub-pulse durations of 1.5 ms (excitation) and 2.3 ms (refocusing) before VERSE was applied. The total durations of the pulses after VERSE were 5.65 ms (excitation) and 7.52 ms (refocusing).

6.2.1.2 GRAPE Pulses

In a first step, a spectral selective pulse was optimized for the whole brain with the GRAPE algorithm [174] on a database of 15 subjects. The optimization was initialized with a sinc shaped pulse with target bandwidth Δf_T. In order to maintain spectral selectivity, B_0 maps from all subjects were duplicated five times and a random frequency shift $\Delta f(\vec{r})$ was added to each voxel following a Gaussian distribution with a standard deviation of $10\Delta f_T$. Then, the optimization target was set to the target flip angle for voxels within the target bandwidth – the passband ($|\Delta f(\vec{r})| \leq \Delta f_T/2$) – and to a flip angle of zero degrees for voxels outside the passband. A complex least-squares cost-function with a flat target phase in the passband was used to achieve a constant phase in slice-selection direction. A weighting term was added to the cost-function, which decreased at the borders of the passband to reduce constraints on the target slice profile.

In a second step, slice-specific pTx pulses were optimized by adjusting the weights inside the passband, such that they exponentially decreased with distance d to the slice center by a factor of $e^{-d/10\text{mm}}$, as in the kT-spokes design. Only the RF pulse shapes from the first step were further optimized for each slice, while the gradients were kept constant to allow for multiband excitation. Finally, a constant slice gradient corresponding to the target slice thickness was added and the pulses were superimposed for multiband excitation and refocusing.

The random frequency shifts cause a phase evolution, which corresponds to the effect of the slice selection gradient and prevents a flat phase throughout the target. This unwanted phase evolution is typically reversed by a slice rewinder gradient, which is not part of the optimization. Therefore, the phase evolution due to the random frequency shifts was removed by subtracting a free precession rotation from the Bloch simulation results of each voxel. The GRAPE excitation pulse had a duration of 6 ms (tbp: 3.6)

and the refocusing pulse had a duration of 8 ms (tbp: 3.2). The final pulses are shown in Figure 6.1.

6.2.1.3 Pulse Simulation

Bloch simulations were conducted for kT-spokes, GRAPE and default CP pulses using B_0 and B_1 maps of the first measured subject (see below). The CP pulses were SLR pulses from the vendors' pulse library with pulse durations of 6 ms (tbp: 4.8) and 12 ms (tbp: 6.0) for excitation and refocusing, respectively. Whole-brain signal maps were simulated for all excitation pulses, refocusing pulses (assuming ideal excitation – $M_0 = M_{xy}$) and for successive application of both pulses. At each voxel position (4 mm isotropic voxels) the transverse magnetization was simulated for each pulse that excites magnetization in the respective voxel. This was done for 20 samples with equidistant positions along a 3 mm line in slice direction and 30 spins per sample.

Averaging all spins in each sample yielded the transverse magnetization per sample such that "slice profiles" of the transverse magnetization were determined for each pulse. The total number of simulated pulses was 110, which all had a nominal slice thickness of 1.5 mm. The signal per voxel was then calculated as the sum of the integrals over all slice profiles that belonged to the respective voxel. Crusher gradients were added to the refocusing pulses to consider dephasing. Additionally, the same simulation was repeated at three distinct positions in the frontal lobe, brainstem and cerebellum with 100 equidistant samples along a 6 mm line in slice direction and 300 spins per sample to determine higher resolution slice profiles of the magnitude and phase of the transverse magnetization.

6.2.2 MRI Sequences and Data Acquisition

Data were acquired on a Siemens MAGNETOM 7T Plus scanner with a 32RX/8TX RF head coil (Nova Medical) from a male subject (47 years - subject 1). The protocol for Diffusion-Weighted Imaging (DWI) consisted of 30 uniformly distributed b-vectors, calculated with the 'dirgen' command of MrTrix3 [132], [176], with a b-value of $b = 1000$ s/mm^2. T_2-weighted volumes ($b = 0$ s/mm^2) were obtained with the same (5 volumes) and with inverted phase encoding direction (3 volumes).

The multiband pTx pulses were implemented in diffusion-weighted EPI and spiral sequences. The EPI sequence was a vendor-provided single-shot blipped-CAIPI diffusion-weighted EPI sequence with GRAPPA acceleration. The sequence was extended to incorporate pTx pulses and trigger for field monitoring. The spiral sequence was implemented with Pulseq and used a time-optimized [88] single-shot spiral-out trajectory. A sine-wave gradient was applied in slice direction during readout to reduce the g-factor penalty [177], [178]. Both EPI and spiral sequences included a fat saturation pulse before each excitation.

The diffusion protocol was measured with the EPI sequence using multiband (acceleration factor $MB = 2$) GRAPE, kT-spokes and default CP mode pulses. The EPI sequence used in-plane GRAPPA acceleration (factor $R = 2$) and partial Fourier sampling ($PF = 6/8$) resulting in an echo time of $TE = 62\,\text{ms}$ and a readout duration of 29.12 ms. Additionally, the EPI scan with GRAPE pulses was repeated including triggers for field monitoring. In this scan, FOV shifts were disabled in the sequence, as they were applied in image reconstruction by using field monitoring data. The same diffusion protocol was also measured with the spiral sequence using GRAPE multiband pulses ($MB = 2$) and field monitoring. The spiral readout was accelerated by a factor of $R = 3$ resulting in an echo time of $TE = 44\,\text{ms}$ and a readout duration of 21.45 ms. A low resolution GRE scan (32 phase-encoding lines) was acquired for coil sensitivity calibration. Other sequence parameters were: Slices= 110, FOV = $210 \times 210 \times 165\,\text{mm}^3$, 1.5 mm isotropic resolution, $TR = 6.4\,\text{s}$. This resulted in a total acquisition time of $TA = 4{:}13\,\text{min}$ for the EPI sequence and $TA = 4{:}20\,\text{min}$ for the spiral sequence. In addition, a B_0 field map was acquired with a multi-echo GRE scan at 1.5 mm isotropic resolution with echo times $TE = 3.06/5.10/7.14\,\text{ms}$ and a total acquisition time of $TA = 2{:}38\,\text{min}$. Field monitoring of both the EPI and spiral sequences was done with a field camera (Skope Magnetic Resonance Technologies, Zürich) in a separate session with optimized field probe positions to allow for full third spatial order monitoring.

Slice profiles of all three multiband pulses were measured with the spiral sequence. An additional phase encoding gradient was used to encode a FOV of 3.2 mm with a resolution of 0.2 mm along the slice direction (16 phase encoding steps). The in-plane resolution was 5 mm and two spiral shots were used. Other parameters were kept the same as in the spiral diffusion protocol resulting in a total acquisition time of $TA = 3{:}56\,\text{min}$. The CP slice profiles were measured for pulses without VERSE gradients, as the vendor implementation of VERSE was not available for the spiral sequence.

Additional data were acquired from a second subject (male, 28 years - subject 2) with both single- and multiband CP, kT-spokes and GRAPE pulses. VERSE was not applied to singleband CP and kT-spokes pulses, as the pulses had lower energy and SAR constraints were not violated. The diffusion protocol was slightly changed to 20 b-vectors ($b = 1000\,\text{s/mm}^2$) and three T_2-weighted volumes to reduce total scan time of the multiband scans to $TA = 2{:}57\,\text{min}$, while the singleband scans had a repetition time of $TR = 10.8\,\text{s}$ and a total acquisition time of $TA = 4{:}42\,\text{min}$.

6.2.3 Image Reconstruction and Processing

EPI data was reconstructed with the vendors' implementation of the slice-GRAPPA [179] multiband reconstruction algorithm. EPI and spiral data acquired with field monitoring were reconstructed with a higher order image reconstruction algorithm [9] using the PowerGrid [96] toolbox. Coil sensitivity maps were estimated with the ESPIRiT algorithm [58]. The field map data was unwrapped with the ROMEO algorithm [38] and filtered

with despiking and Gaussian filters ($\sigma = 0.5$ voxel). Field monitoring data was synchronized with the MR signal by cross-correlation of a frequency modulated sine-wave signal, which was acquired in a calibration prescan by both the field camera and the scanners' receive coil. The data was low-pass filtered and every second trigger of each volume acquisition was interpolated as the slice-TR was too low for consecutive excitation of field probes. Reconstruction of slice profile data was done with the "parallel imaging with compressed sensing (pics)" algorithm from the Berkeley Advanced Reconstruction Toolbox (BART) [83].

Reconstructed images were denoised [119], [141] and corrected for Gibbs-Ringing [114]. EPI images were corrected for distortions, eddy-currents and motion [110], [116]. EPI and spiral images reconstructed with higher order image reconstruction were only corrected for motion, as distortions and eddy currents were already corrected in the reconstruction by using field monitoring data. Images from all scans were corrected for gradient non-linearities [117] and registered to the midway space of the EPI CP and GRAPE acquisitions [120]. A brain mask was calculated from a T_1-weighted MPRAGE scan using ANTsPyNet [121] and registered to the DWI data using "FLIRT" from FSL [120]. White matter voxels were segmented from the MPRAGE images using FSL "FAST" [125] in order to determine the SNR only in white matter. Fractional anisotropy (FA) and mean diffusivity (MD) maps were calculated with FSL's "dtifit" command. An SNR measure was calculated by dividing the mean of the T_2-weighted and the diffusion-weighted images by the noise map obtained in the denoising step.

6.3 Results

Simulated signal maps of CP, kT-Spokes and GRAPE pulses are shown on the left in Figure 6.2 after excitation, after refocusing (assuming ideal excitation) and after successive application of both pulses. The signal after excitation was highest for the kT-spokes pulse with the lowest standard deviation. The CP and GRAPE pulses showed similar performance over the whole brain. The performance of the GRAPE refocusing pulses was better compared to CP and kT-spokes pulses with slightly higher signal and lower standard deviation across the brain. After application of both pulses, kT-Spokes and GRAPE pulses showed similar signal levels with lower standard deviation of the GRAPE signal, while CP pulses had significantly lower mean signal.

The slice profiles of the three pulses at three different positions are depicted on the right in Figure 6.2. kT-Spokes excitation pulses had a slightly thicker slice profile compared to CP and GRAPE pulses. All pulses showed high transverse magnetization in the frontal lobe (voxel 1), while performance in the cerebellum (voxel 3) was strongly reduced for CP and slightly reduced for GRAPE pulses. kT-spokes pulses showed reduced magnetization in the brainstem (voxel 2). GRAPE and CP slices were slightly displaced in the frontal lobe. Some phase variation across the slice was observed for kT-Spokes and GRAPE pulses, but the phase did not differ by more than 30°.

Figure 6.3 shows T_2-weighted and diffusion-weighted images after preprocessing. Enhanced signal in the cerebellum and in the center of the brain was visible for both kT-Spokes and GRAPE pTx pulses compared to CP pulses. Signal voids were present in the frontal lobe and the brainstem using kT-Spokes, which were not visible for CP and GRAPE pulses. Insets in the EPI GRAPE images with and without field monitoring show slightly reduced blurring in images reconstructed with field monitoring data. Enhanced signal especially in the white matter is visible in the spiral images, leading to a slightly different contrast compared to EPI images. Remaining artifacts related to B_0 inhomogeneities were visible especially in the frontal part of the brain.

SNR maps in Figure 6.4 show increased SNR in the cerebellum for both kT-Spokes and GRAPE pulses compared to CP pulses. The mean SNR in the brain was higher for kT-Spokes pulses compared to GRAPE pulses, while CP pulses had the lowest mean SNR. Spiral images showed increased SNR compared to EPI images across the whole brain. The percentage SNR gain of spiral images was higher for DWI volumes compared to T_2-weighted volumes.

Slice profiles of the three different pulses for three example slices are displayed in Figure 6.5. In the upper slice, the slice profiles of CP and GRAPE pulses were similar, while the kT-Spokes pulse had a slightly thicker slice profile. For the CP pulses, signal outside the excited slice was observed, which was not present for kT-Spokes and GRAPE pulses. In the middle slice, significant slice bending was visible for CP and GRAPE pulses in the anterior part of the brain. Slice bending was less pronounced for the kT-Spokes pulse, which instead showed signal voids in the anterior part of the slice. The slice thickness of the kT-spokes pulse was higher compared to the CP and GRAPE pulses. In the lower slice, slice bending was again present for the CP and GRAPE pulses in the anterior part (brainstem), but less pronounced compared to the middle slice. The slice profile of CP and kT-Spokes pulses was slightly thicker compared to GRAPE pulses and kT-Spokes pulses showed signal loss in the brainstem.

Figure 6.6 shows FA and MD maps obtained from DTI fits done for all EPI and spiral acquisitions. Poor DTI fits were observed in the lower part of the cerebellum in the CP volumes and in the the frontal lobe and the brainstem of kT-Spokes volumes (yellow arrows), corresponding to low SNR regions. Spiral FA maps appear less noisy compared to FA maps from EPI measurements. However, an artifact in the anterior part of the brainstem was visible in spiral FA and MD maps (red arrow).

In Figure 6.7 one coronal view of DWI images, SNR maps and FA maps is shown for single- and multiband CP, kT-Spokes and GRAPE pulses acquired from the second subject. Single- and multiband versions of each pulse led to similar signal patterns across the displayed coronal slice. Mean SNR was decreased for singleband pulses compared to multiband pulses. This resulted in more noise in FA maps, which was especially visible in the cerebellum of the singleband CP FA map.

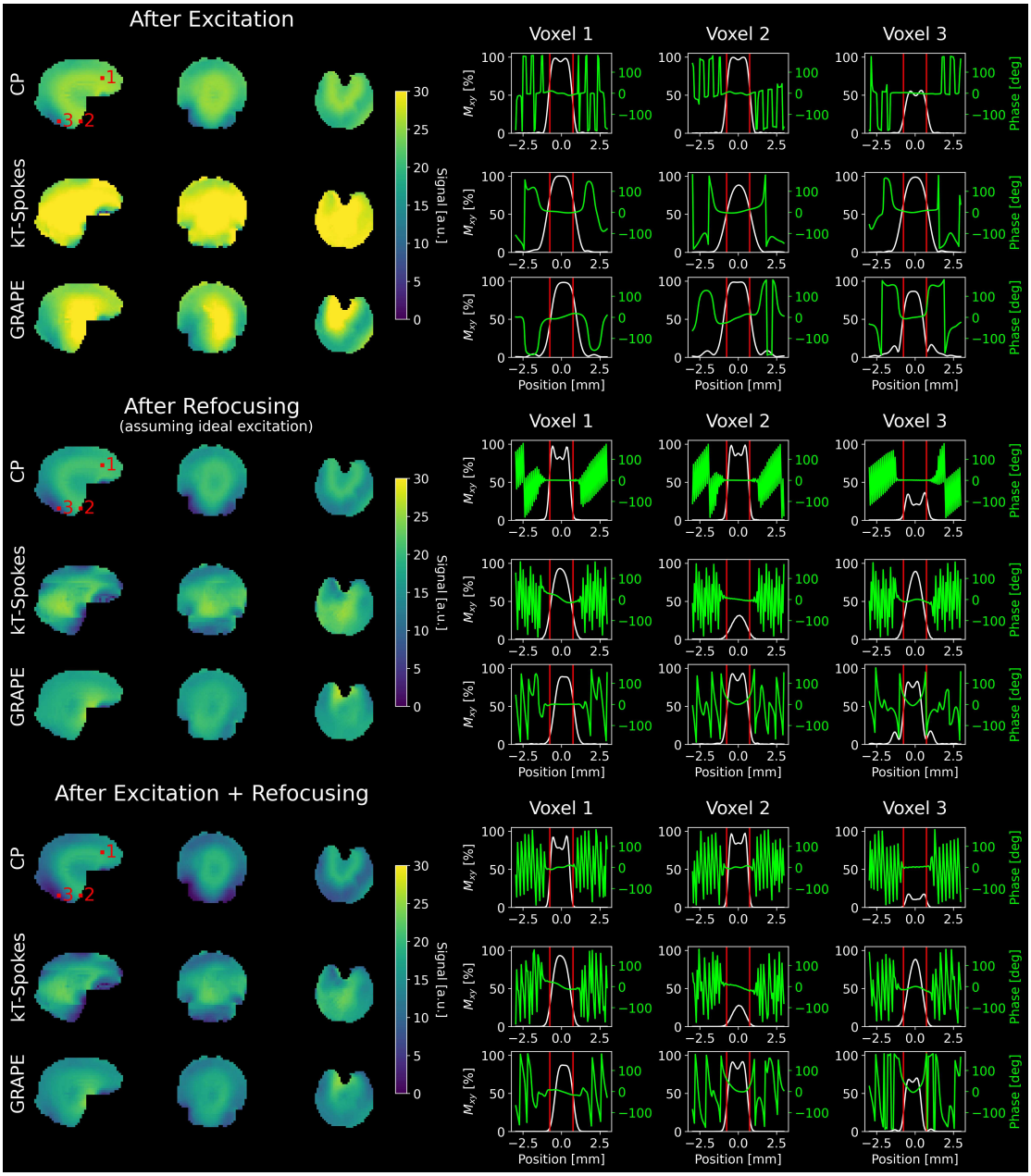

Figure 6.2: Left: Simulated signal of CP, kT-Spokes and GRAPE pulses after excitation, refocusing (assuming ideal excitation) and successive application of both pulses. The displayed signal level per voxel is the integral of the simulated transverse magnetization in slice direction. Mean and standard deviation of the signal over the whole brain after excitation were: CP: 21.8 ± 3.3, Spokes: 28.6 ± 2.6, GRAPE: 23.9 ± 4.3. After refocusing: CP: 17.1 ± 3.9, Spokes: 17.4 ± 4.0, GRAPE: 18.0 ± 2.3. After both pulses: CP: 13.5 ± 4.6, Spokes: 15.4 ± 4.0, GRAPE: 15.3 ± 2.9. Right: Simulated transverse magnetization of CP, kT-Spokes and GRAPE pulses along the slice direction at three distinct positions. The positions are marked in the sagittal slice of the CP signal maps. The Bloch simulations were done along a 6 mm line in slice direction. The red vertical lines show the target slice thickness of 1.5 mm. The magnitude of the transverse magnetization in percent of the initial magnetization is shown in white and the phase is shown in green.

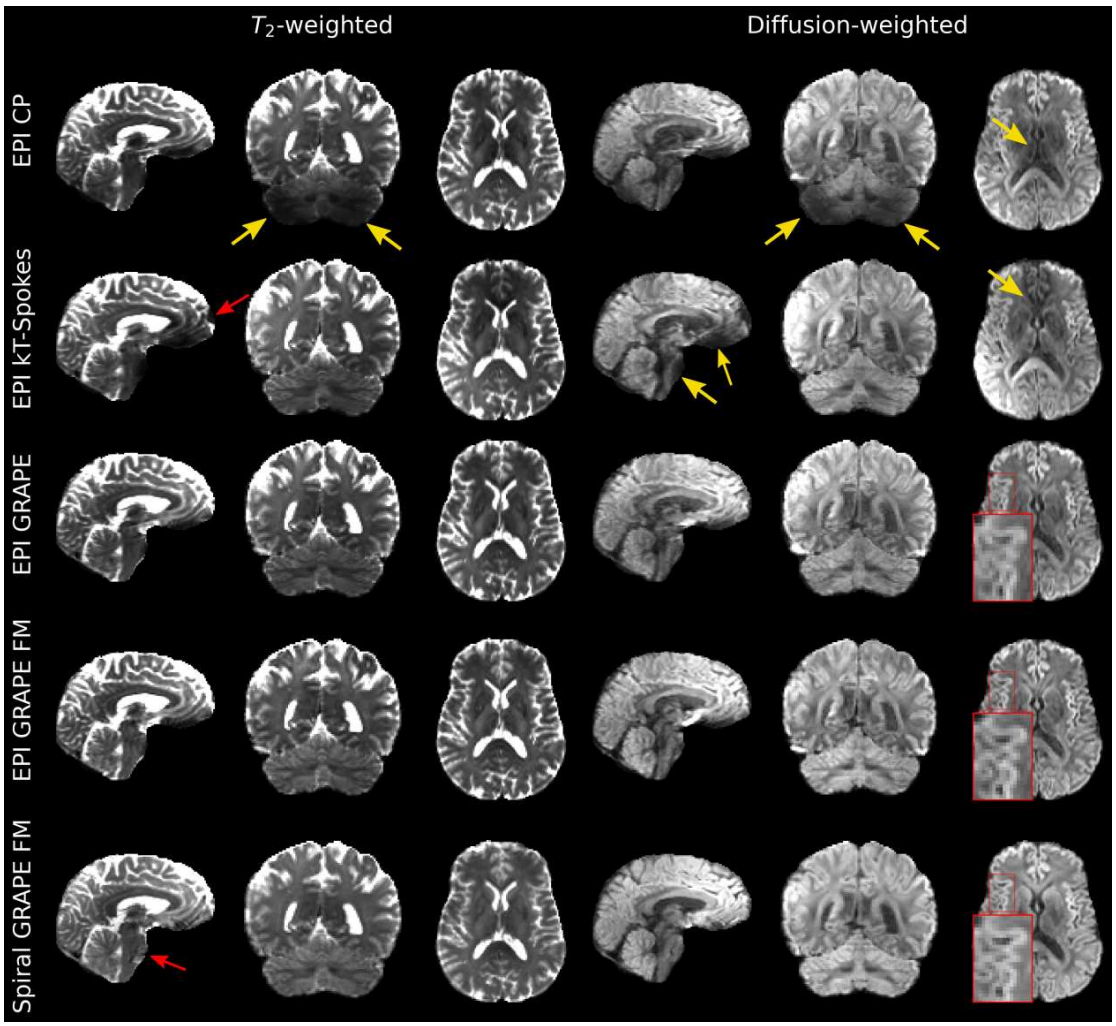

Figure 6.3: Preprocessed T_2- and diffusion-weighted ($b = 1000\,\mathrm{s/mm^2}$) whole-brain volumes of subject 1 acquired with EPI and spiral sequences using CP, kT-Spokes and GRAPE pulses. "FM" denotes higher order image reconstruction with field monitoring data. Yellow arrows mark areas, where signal loss is observed. Red arrows mark some of the artifacts related to B_0 inhomogeneity.

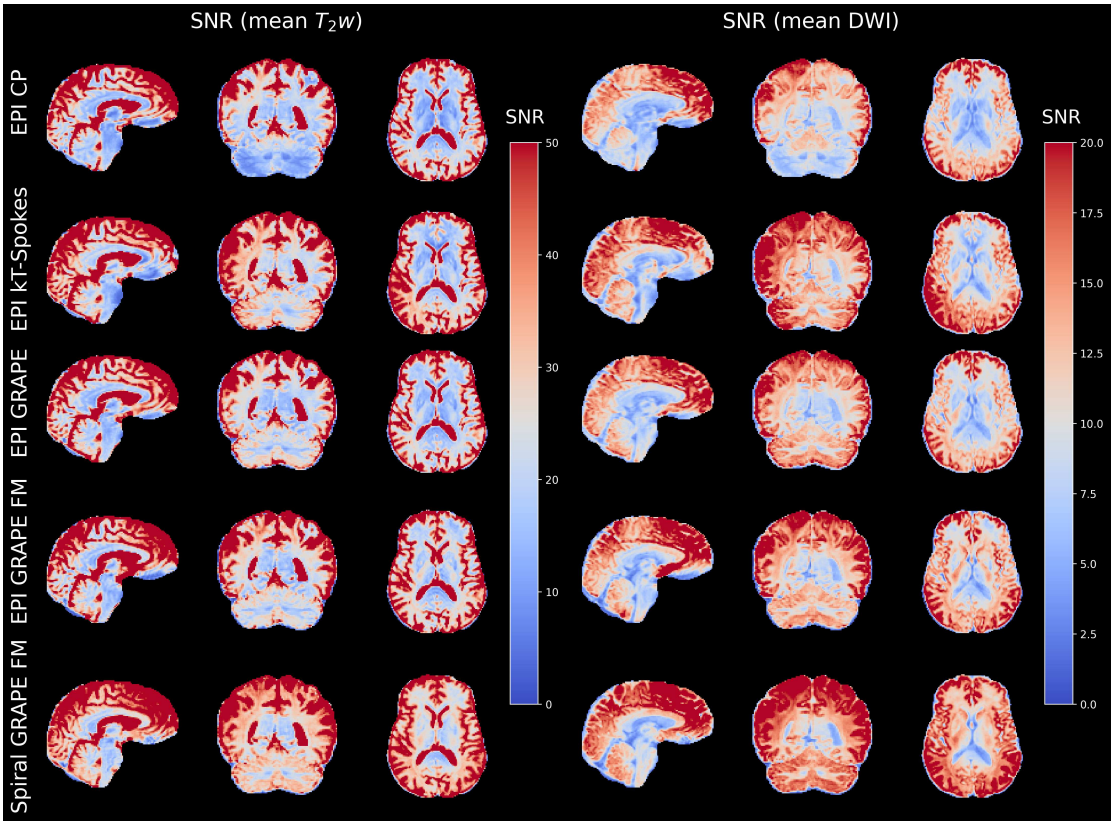

Figure 6.4: SNR maps of mean T_2-weighted and diffusion-weighted ($b = 1000\,\mathrm{s/mm^2}$) volumes acquired with EPI and spiral sequences using CP, kT-Spokes and GRAPE pulses (subject 1). "FM" denotes higher order image reconstruction with field monitoring data. Mean SNR values across the brain for the T_2-weighted volumes were: 38.23 (EPI CP), 43.62 (EPI kT-Spokes), 40.27 (EPI GRAPE), 42.97 (EPI GRAPE FM), 43.56 (Spiral GRAPE FM). For the diffusion-weighted volumes, the mean SNR values were: 11.93 (EPI CP), 14.07 (EPI kT-Spokes), 12.75 (EPI GRAPE), 13.58 (EPI GRAPE FM), 15.36 (Spiral GRAPE FM).

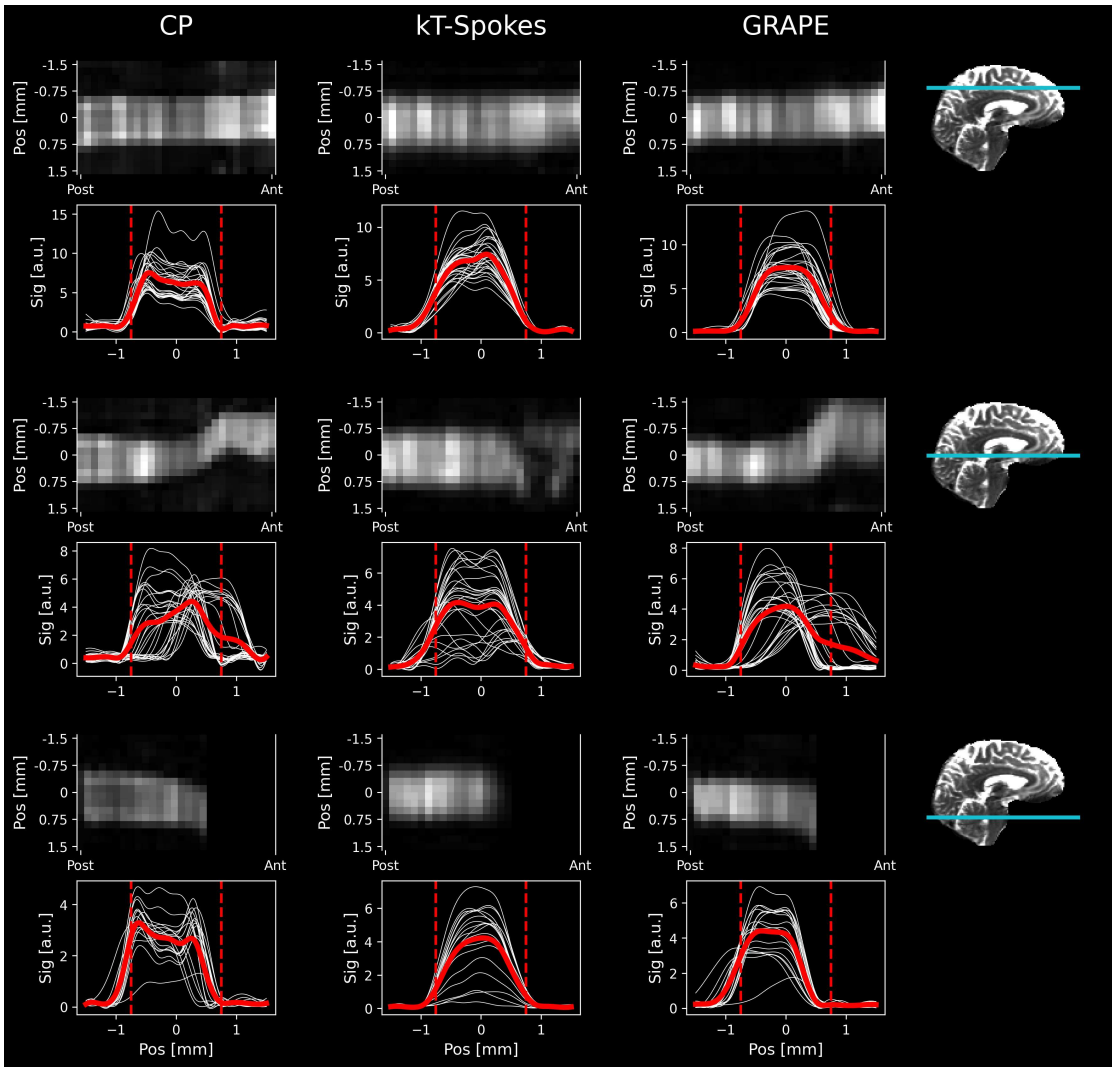

Figure 6.5: Slice profiles of CP, kT-Spokes and GRAPE pulses displayed for three example slices in the upper, middle and lower part of the brain (subject 1). Below each slice profile, cross sections along the anterior-posterior direction are plotted in white and the mean of all cross sections is shown in red. The nominal slice borders are indicated by dotted red lines. In the last column the position of the slice is shown.

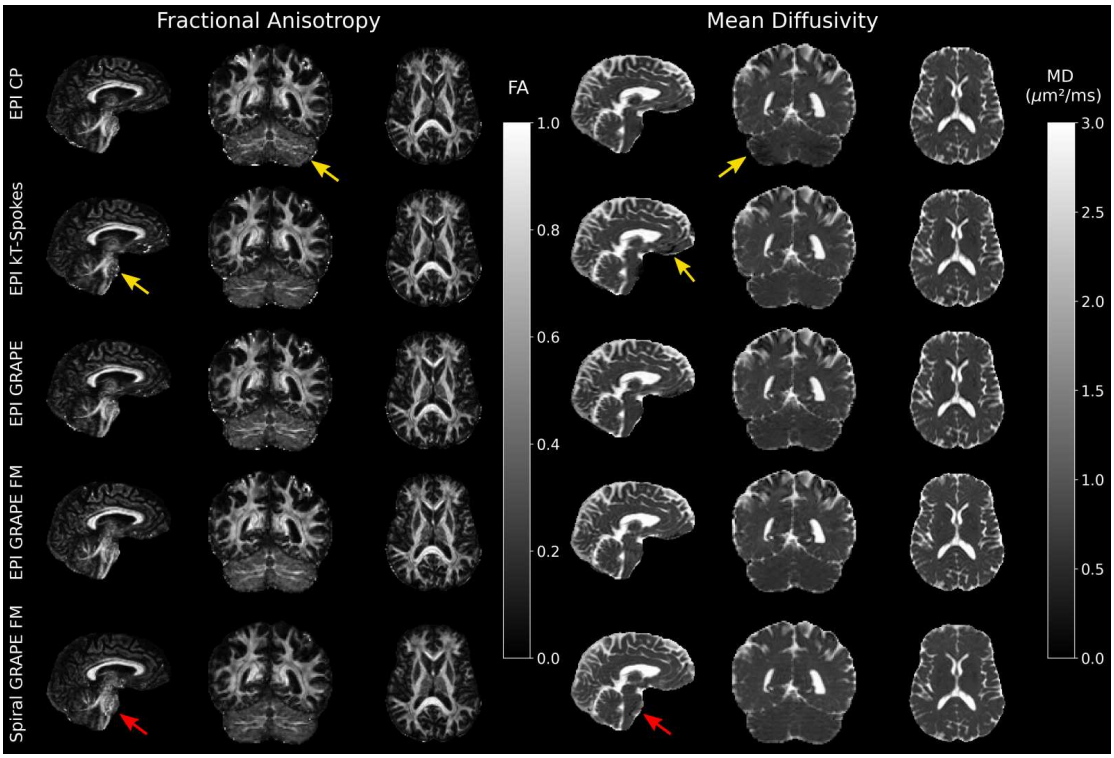

Figure 6.6: Fractional anisotropy and mean diffusivity maps obtained from DTI fits of all EPI and spiral acquisitions (subject 1). Yellow arrows mark areas, where poor DTI fits were observed. Red arrows mark an artifact in the anterior part of the brainstem in spiral images.

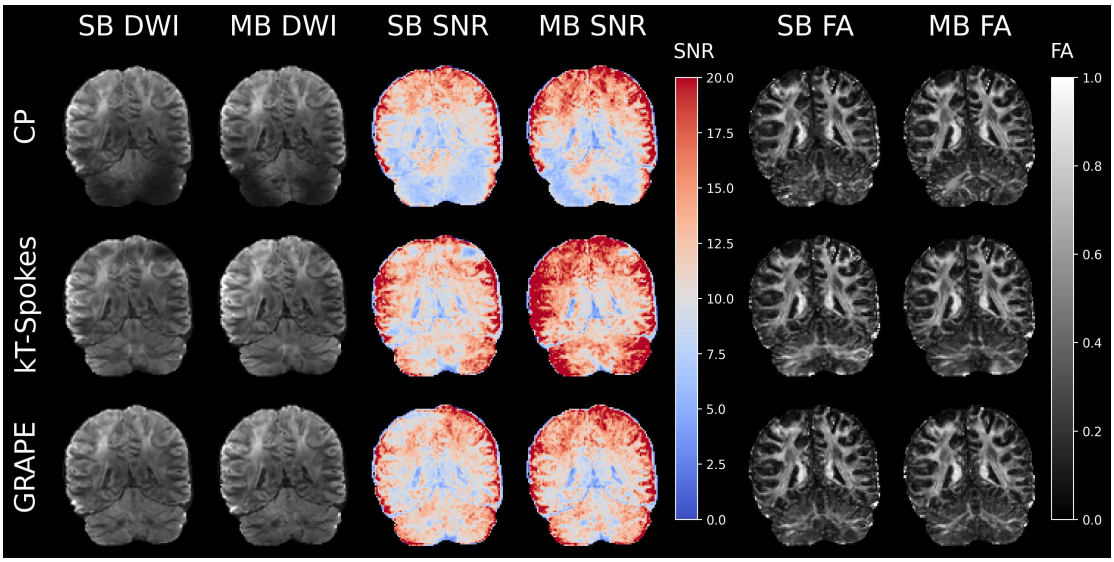

Figure 6.7: Diffusion-weighted ($b = 1000\,\mathrm{s/mm^2}$) volumes, SNR maps and fractional anisotropy maps acquired with the EPI sequence using singleband (SB) and multiband (MB) CP, kT-Spokes and GRAPE pulses (subject 2). SNR maps are shown for mean DWI volumes and mean SNR values in the brain were: 11.25 (SB CP), 12.77 (MB CP), 12.45 (SB kT-Spokes), 14.57 (MB kT-Spokes), 11.86 (SB GRAPE), 12.67 (MB GRAPE).

6.4 Discussion

The presented results demonstrate the great potential of multiband pTx pulses for whole-brain diffusion imaging at 7T. Both kT-Spokes and GRAPE pulses increased SNR in the cerebellum and in the center of the brain compared to CP pulses. Improved SNR in the cerebellum translated to less noise-related artifacts in FA and MD maps. However, signal voids were observed in areas with large off-resonances such as the brainstem and the frontal lobe for kT-Spokes pulses. In contrast, GRAPE pulses were more robust to off-resonances and led to better homogeneity throughout the brain, which was in agreement with the simulations. This can be explained by the increased number of degrees of freedom in GRAPE optimization. Pulse shapes and gradients are not only optimized for a limited number of points in excitation k-space, but for each discretized RF and gradient sample [174].

The simulations showed that the performance of the GRAPE excitation pulse was suboptimal compared to the kT-Spokes excitation pulse. A combination of kT-Spokes excitation and GRAPE refocusing pulses could improve results further. The simulation results after refocusing (with ideal excitation) and after application of both pulses were similar, which indicates that the final signal is mostly dependent on the performance of the refocusing pulses.

The overall higher SNR of kT-Spokes pulses compared to GRAPE and CP pulses matches with the slightly broader slice profile, which was observed both in simulations and measurements. The slice profile measurements also showed that both CP and GRAPE pulses suffer from slice bending in off-resonant areas of the brain such as the frontal part of the brain. The slice bending is caused by the limited bandwidths of the pulses, which are close to the off-resonance frequency ($\sim 300 - 400\,\mathrm{Hz}$) in these areas. In contrast, kT-spokes pulses consisted of shorter sub-pulses, which had considerably higher bandwidth ($> 1000\,\mathrm{Hz}$) per sub-pulse.

Realizing a higher bandwidth for the CP pulses would be possible by shortening the pulses at fixed time-bandwidth product. This would also increase SAR, which is feasible when using CP pulses, as the SAR constraints were not fully exhausted (65 % of maximum) for the given *TR*. Increasing the bandwidth of the GRAPE pulses is more challenging, as pulses with higher bandwidths do not reach the target flip angle in the optimization at the given SAR constraints. Higher SAR constraints could be used in GRAPE optimization, if VERSE would be applied to the final GRAPE pulses. However, this requires further investigation as the response to B_0 inhomogeneities might be affected if the optimized gradients are altered by VERSE.

The application of VERSE in kT-Spokes design was important for SAR reduction and to reach a reasonable *TR* for whole-brain imaging. We observed that it is crucial to preserve the total duration of the kT-spokes pulses when applying VERSE. Slice profiles were only slightly affected by the application of VERSE as shown in Appendix Figure A12. The bipolar design of kT-spokes pulses makes them more time-efficient

than monopolar pulses, but also more prone to off-resonances as slice bending occurs in opposite directions for subsequent sub-pulses due to opposite slice gradient signs. Therefore, high bandwidths are required for the sub-pulses. A comparison of bi- and monopolar kT-spokes pulses (Appendix Figure A12) indicates that slice profiles are not improved when using monopolar pulses.

Similar SNR would be expected for single- and multiband pulses, as multiband acceleration lowers SNR only by an increased g-factor, which is typically small at a multiband factor of $MB = 2$. Instead, lower SNR across the whole brain was observed in all DWI images acquired with singleband pulses compared to multiband pulses. We attribute this to differences in the vendors' image reconstruction algorithms (e.g. different regularization) for single- and multiband reconstruction.

Both kT-spokes and GRAPE pulses were optimized for a transverse orientation of the imaging volume aligned to the top of the head, which is not optimal in terms of volume coverage. In the pulse optimization, the same weighting parameter $e^{-d/10\text{mm}}$ as in Gras et al. [172] was used. The authors of that paper investigated that the perfomance of their slice-selective pTx pulses is robust to small tilts and offsets using this weighting, which however needs to be investigated for the proposed multiband pulses.

As kT-Spokes and GRAPE pulses were not optimized for specific subjects but were calculated as universal pulses, further tests on different subjects are required before these pulses can be routinely used in clinical studies. This includes tests on subjects with different head shapes, sizes, and ages.

Higher order reconstruction with field monitoring data reduced blurring in EPI images compared to standard image reconstruction with image-based distortion correction. This is especially the case for diffusion-weighted images, as eddy currents due to strong diffusion gradients are effectively corrected [5]. Field monitoring also enables usage of spiral readouts, which are more time-efficient in sampling k-space compared to EPI and allow for shorter echo times resulting in higher SNR. The SNR gain of spirals compared to EPI is higher in DWI images (13 %) compared to T_2-weighted images (1.5 %) as T_2 is shorter in white and gray matter compared to CSF, which is suppressed in DWI images. In white matter voxels the SNR gain was 17 %, which is lower than the expected SNR gain of 43 % when assuming $T_2 = 50\,\text{ms}$ in white matter. The lower SNR gain can be explained with the higher total acceleration factor and the shorter readout time of spirals compared to EPI. However, the shorter spiral readout is beneficial to reduce off-resonance related artifacts and blurring due to T_2^* signal decay.

Off-resonance artifacts are still problematic for both EPI and spiral sequences and were not fully corrected in both image-based distortion correction and higher order image reconstruction. These artifacts were especially visible in the frontal part of the brain and near the ear canals, where strong B_0 gradients are present and the B_0 field map is not accurate enough. Improvements in B_0 mapping might be possible by using a regularized field map estimation of multi-echo GRE data [180].

6.5 Conclusions

The designed multiband kT-spokes and GRAPE pulses improved whole-brain B1 homogeneity in diffusion-weighted images compared to non-pTx pulses. While kT-spokes pulses suffered from signal dropouts in areas with large B_0 inhomogeneities in the frontal lobe and brainstem, this limitation was overcome with GRAPE pulses. Further SNR improvement was possible by combining pTx pulses with a time-efficient spiral readout and field monitoring. Large B_0 inhomogeneities still remain challenging for both pulse design and image reconstruction. Limited bandwidth of GRAPE pulses due to SAR restrictions led to bended slices, while distortions and blurring in EPI and spiral images were not fully corrected.

Chapter 7

Conclusions

The aim of this thesis was to improve the acquisition and quality of diffusion-weighted images at high and ultra-high field strengths. A fast spiral DWI sequence with multiband acceleration was combined with various techniques for field inhomogeneity correction.

In order to simplify and accelerate prototyping of new MR pulse sequences for DWI, a workflow based on open-source tools was developed. This workflow was used for the development of a multiband spiral sequence for DWI, a stack-of-spirals 3DREAM sequence and a multi-echo Cartesian GRE sequence for mapping of B_0 field inhomogeneities. These sequences formed the foundation for generating the results in the subsequent parts of this thesis. Different reconstruction algorithms were integrated into this workflow, including reconstruction of non-Cartesian data and correction for static and dynamic B_0 field inhomogeneities. It was successfully demonstrated that data acquisition at different MRI sites with the same sequence is possible by using the proposed workflow. Further development of this workflow may focus on removing remaining manual processing steps and reducing reconstruction times for spiral sequences in order to enable routine imaging during clinical studies.

The developed multiband spiral sequence was successfully used for DWI measurements at a 3T scanner with a high performance gradient system. From these DWI measurements, axon radii in the white matter of the human brain were estimated. The results were compared to those of a multiband EPI sequence and it was shown that the higher SNR provided by the spiral readout can improve axon radius estimation by reducing test–retest variability. It was also demonstrated that using magnetic field monitoring enables the usage of non-Cartesian spiral trajectories and reduces artifacts related to eddy currents in images with strong diffusion weighting. However, a significant bias was detected in test–retest measurements of some subjects, pointing towards a potential issue regarding repeatability of axon radius estimation. While it was found that the deviations between test and retest resided mainly in the images with stronger diffusion-weighting, the reason for the bias remained unclear. A deeper investigation of this issue might focus on the stability of the gradient system at higher gradient strengths. One possible method would be magnetic field monitoring, although this approach is challenging at higher gradient strengths due to strong dephasing of the field probes.

Moving from high (3T) to ultra-high (7T) field, one of the main challenges is the inhomogeneity of the B_1 transmit field. Mitigating B_1 inhomogeneities requires accurate mapping of the actual B_1 fields. In the third part of this thesis, an improved version of the 3DREAM B_1 mapping sequence with a stack-of-spirals readout was developed. It was demonstrated that the spiral 3DREAM sequence can generate accurate B_1 maps within a few seconds of acquisition time. Blurring and ventricular contrast in B_1 maps were reduced when using a spiral instead of a Cartesian readout especially at higher image resolution. A future extension of this sequence might be the implementation of multi-channel B_1 mapping for parallel transmit coils.

In the last part of this thesis, whole-brain DWI at 7T was performed using multiband

parallel transmit (pTx) pulses in EPI and spiral DWI sequences. PTx pulses largely mitigated the deteriorating effects of B_1 inhomogeneities that led to signal loss in the cerebellum and the center of the brain. While kT-Spokes pulses were prone to B_0 inhomogeneity, this issue was resolved by using GRAPE pulses. The increased signal in the cerebellum improved diffusion tensor fitting, which resulted in more accurate fractional anisotropy and mean diffusivity maps. One remaining challenge is the low bandwidth of the GRAPE pulses, which leads to bended slices in areas with large B_0 inhomogeneity. It was not possible to increase bandwidths due to SAR constraints. The application of VERSE could loosen SAR constraints, but the effect of VERSE on gradients optimized with the GRAPE algorithm has not yet been investigated.

It was also demonstrated that the increased SNR of spiral DWI led to improved diffusion tensor fitting compared to EPI DWI. Additionally, image reconstruction based on the measured actual encoding fields resulted in slightly improved image quality compared to image-based corrections. While dynamic B_0 inhomogeneities in EPI and spiral sequences were largely corrected by field monitoring, static B_0 inhomogeneities remained challenging due to inaccuracies in B_0 maps and changing B_0 fields due to subject motion. This is especially problematic for spiral imaging, where off-resonant signal leads to strong blurring in images. Future improvements in the accuracy of static B_0 mapping methods would enhance image quality, but motion related field changes cannot be addressed by static field mapping and are a significant challenge in single-shot diffusion-weighted imaging.

Appendix

Supporting Figures

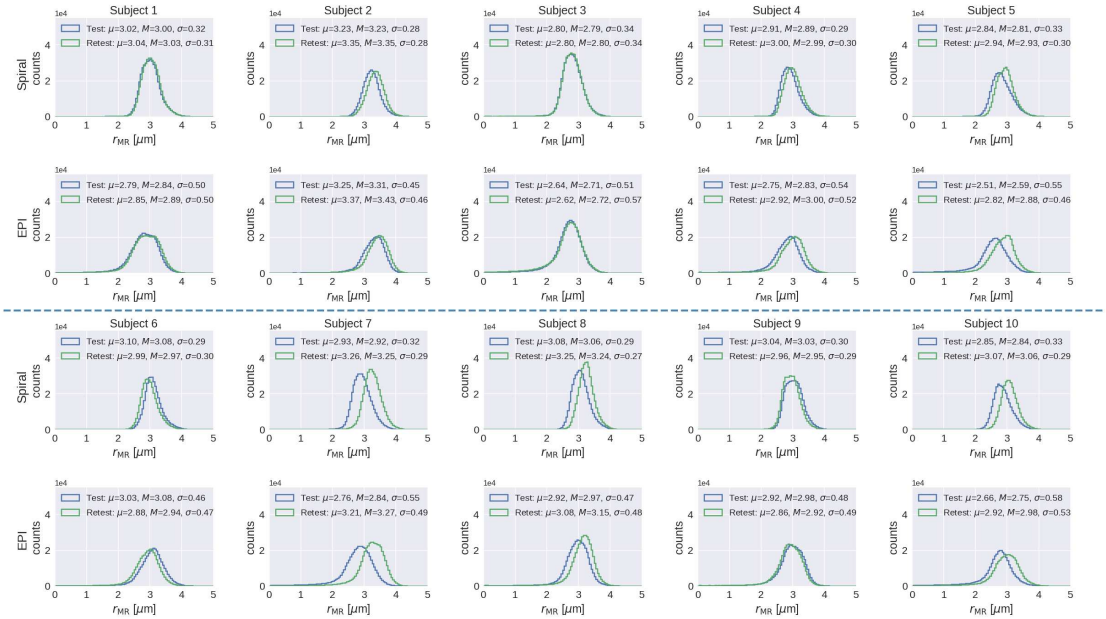

Figure A1: Histograms of the MR axon radius (r_{MR}) distributions in white matter comparing test and retest measurements for all subjects. Mean (μ), median (M) and standard deviation (σ) of the distributions are shown in the legend.

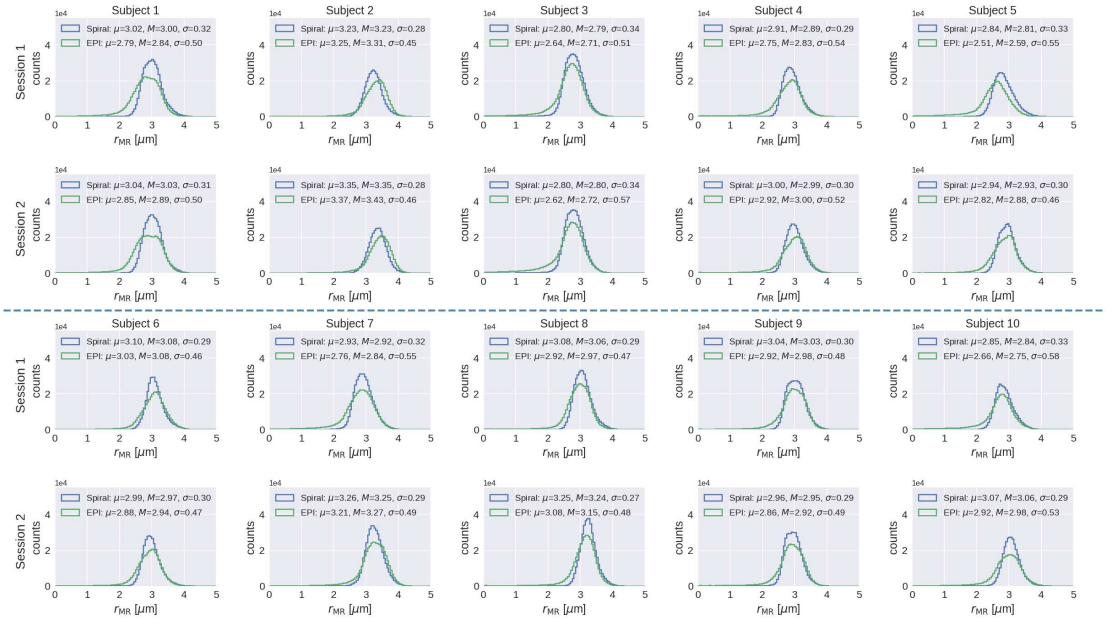

Figure A2: Histograms of the MR axon radius (r_{MR}) distributions in white matter comparing EPI and spiral data for all subjects and sessions. Mean (μ), median (M) and standard deviation (σ) of the distributions are shown in the legend.

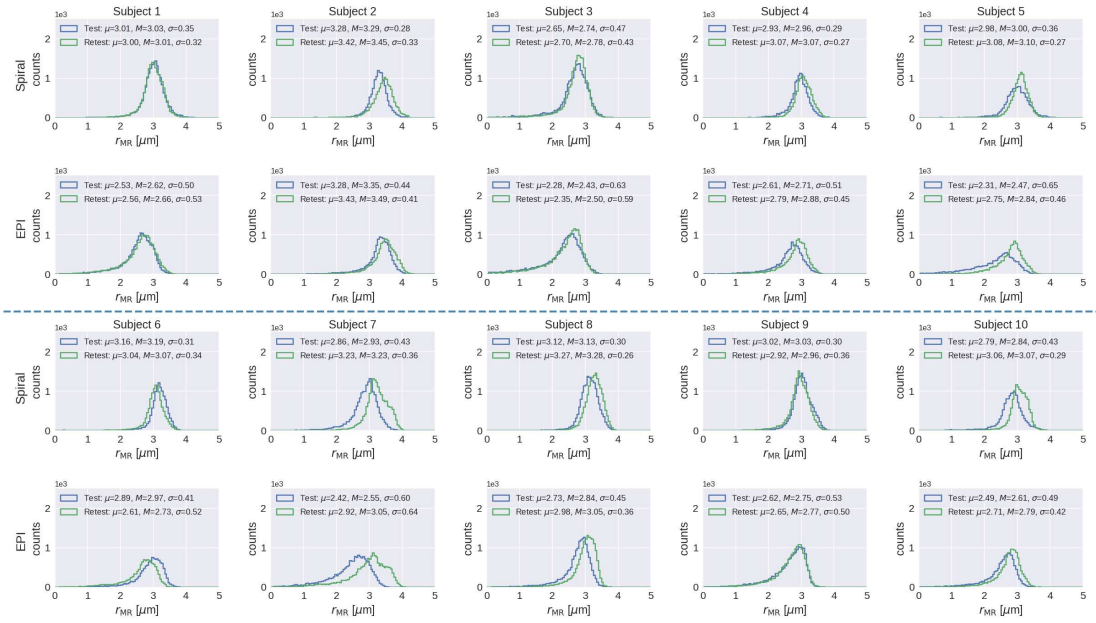

Figure A3: Histograms of the MR axon radius (r_{MR}) distributions in the corpus callosum comparing test and retest measurements for all subjects. Mean (μ), median (M) and standard deviation (σ) of the distributions are shown in the legend.

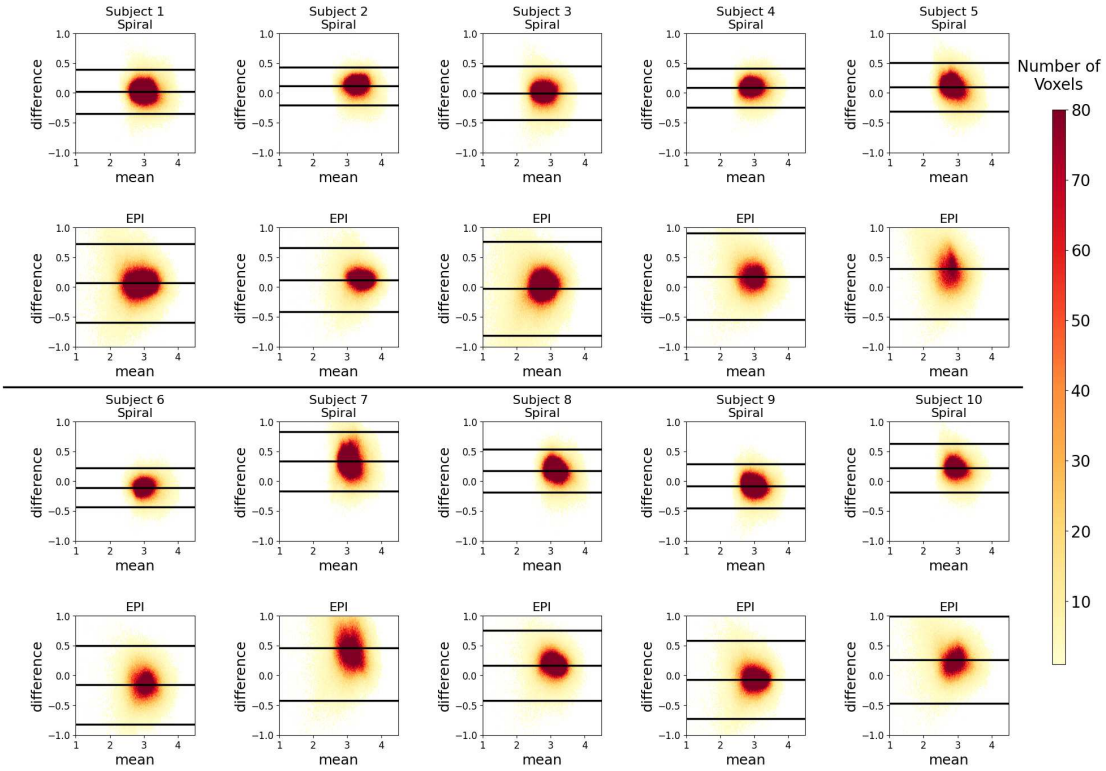

Figure A4: Bland-Altman plots of all subjects for all white matter voxels. Solid lines represent the absolute mean difference and the limits of agreement, calculated as $1.96 \times \sigma$, where σ is the standard deviation.

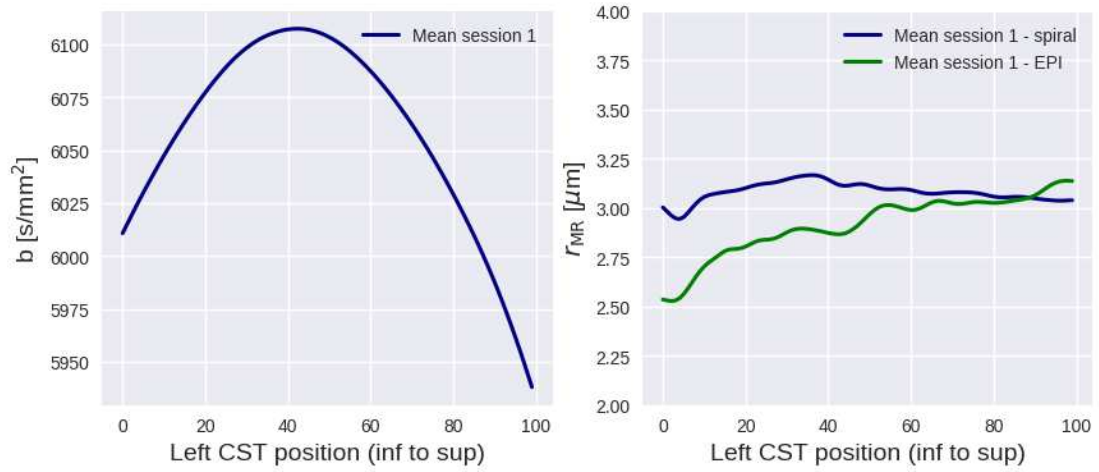

Figure A5: Left: Mean b-value across all subjects along the left CST from inferior to superior positions. Right: Corresponding mean axon radii along the left CST as shown in Figure 4.6 (top left and right).

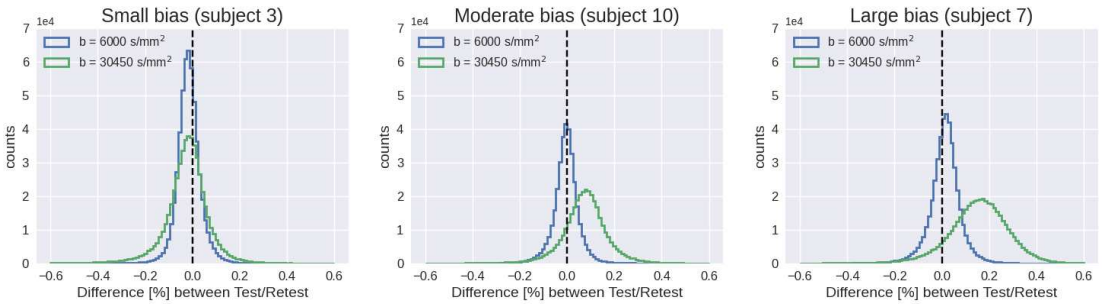

Figure A6: Histograms of difference [%] between test and retest of powder-averaged signals in the white matter. The difference Δ [%] was calculated for both shells as $\Delta = (\bar{S}_{\text{test}} - \bar{S}_{\text{retest}})/\bar{S}_{\text{test}}$, where $\bar{S}$ is the powder-averaged signal. Three different subjects with small, moderate and large bias of the MR axon radius are displayed.

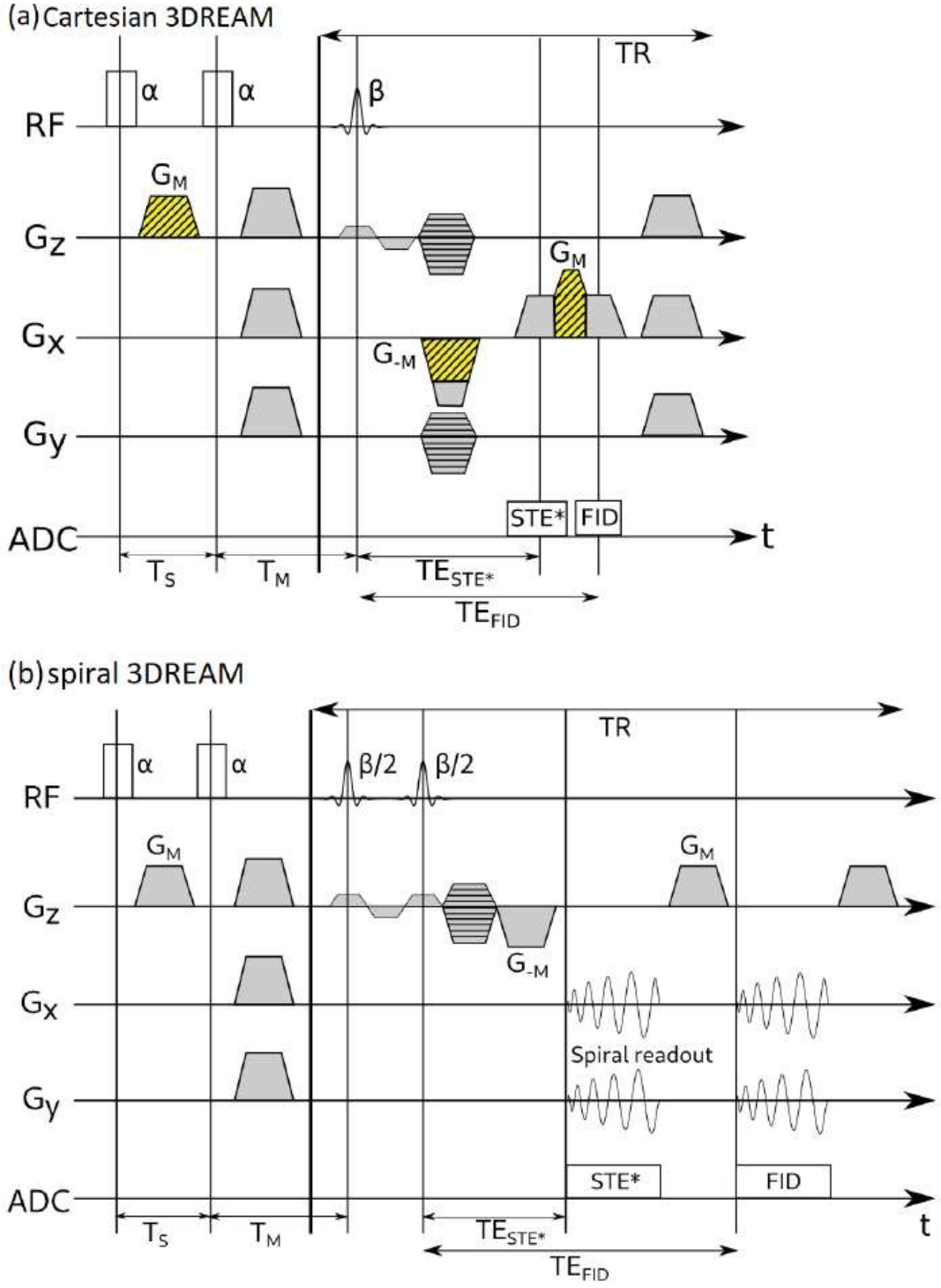

Figure A7: (a) The sequence diagram of the modified Cartesian 3DREAM with an additional spoiler moment (highlighted in yellow) between the STE* and FID readouts to better separate the signals in k-space. (b) The sequence diagram of the spiral 3DREAM sequence (Figure 1) with signal separation gradients in slice direction.

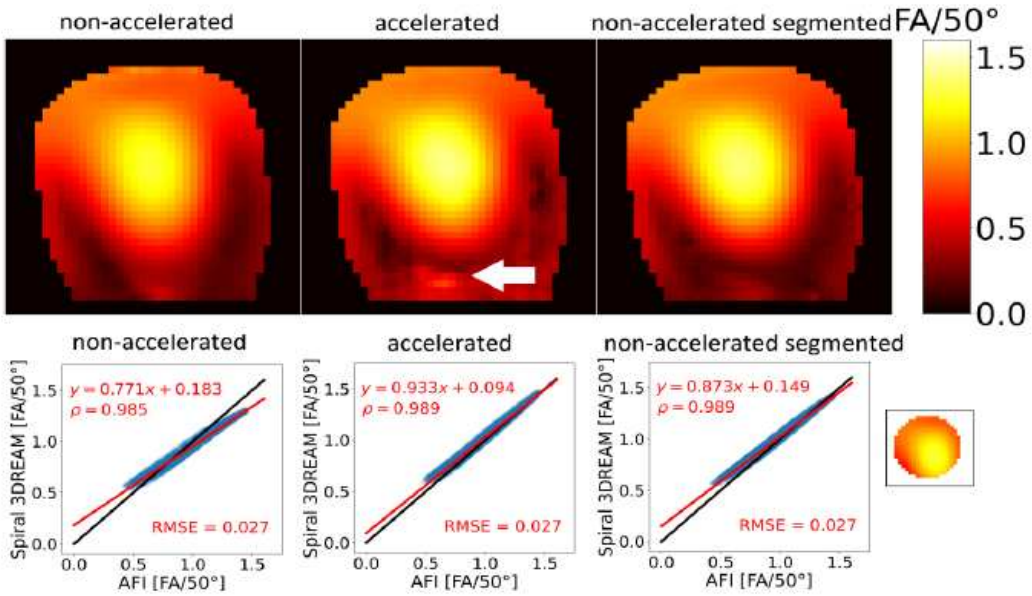

Figure A8: Phantom experiments with different acceleration of the spiral 3DREAM sequence. Top row: One sagittal 5 mm slice in the phantom's center for a non-accelerated, accelerated, and non-accelerated segmented spiral scan. Bottom row: Scatterplots with linear fits for the comparison of the flip angle maps to the AFI sequence with normalized axes, corresponding to the three acceleration schemes. The selected region for the comparison is placed in the bottom-right hand corner. A white arrow points to a region with increased blurring at the bottom of the phantom, which is not present in the non-accelerated segmented scan.

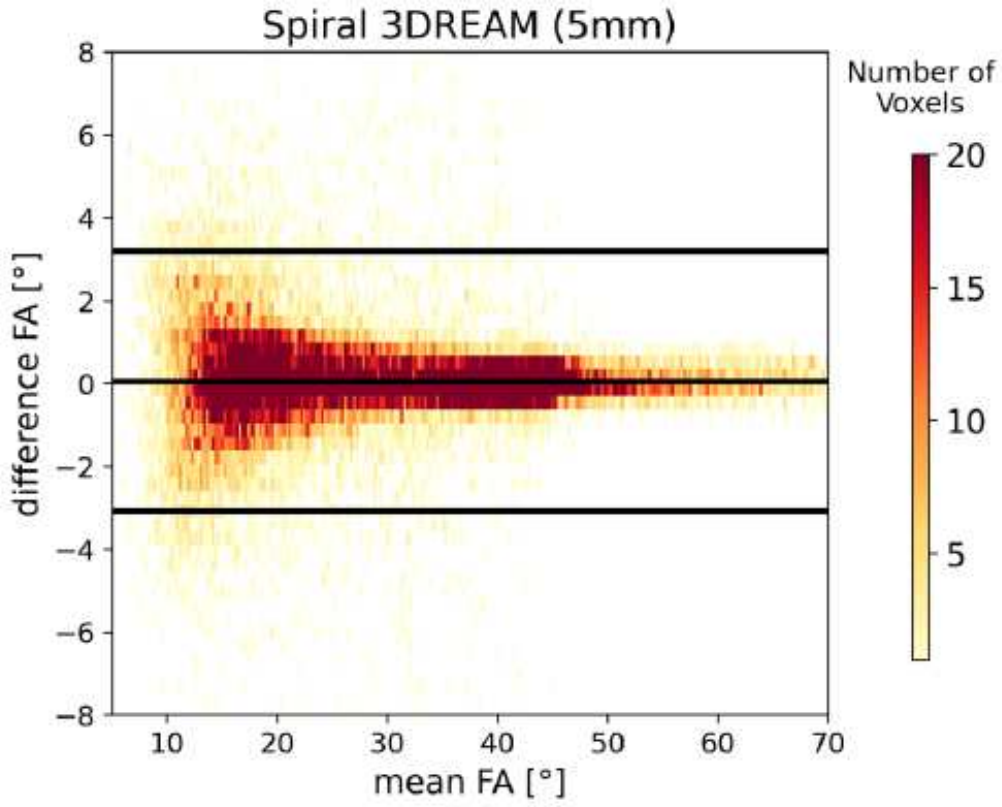

Figure A9: Bland-Altman plot for the test-retest measurement of the spiral 3DREAM sequence. Solid lines represent the absolute mean difference of the two measurements and the limits of agreement, calculated as $\pm 1.96 \times \sigma$, where σ is the standard deviation.

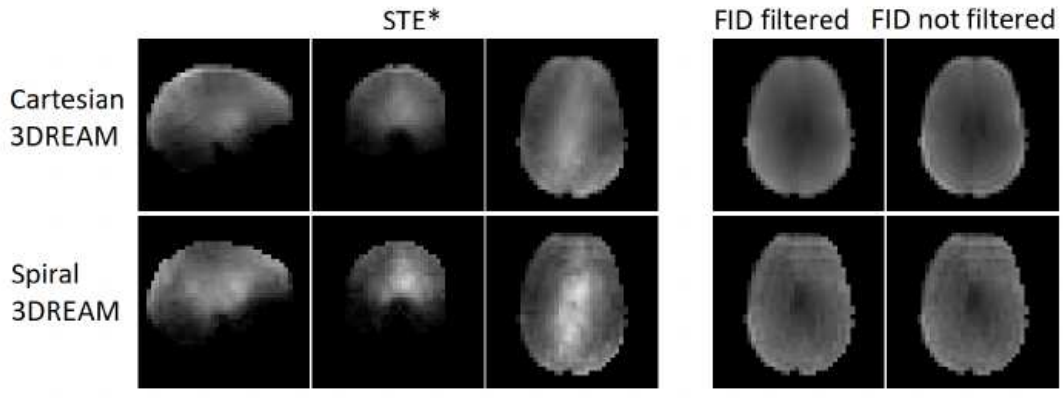

Figure A10: One sagittal, coronal and transversal slice of the STE* at 5 mm resolution is shown for both Cartesian (top) and spiral (bottom) 3DREAM sequences. Additionally, the transversal slice of the FID is displayed on the right, with and without the FID filter applied.

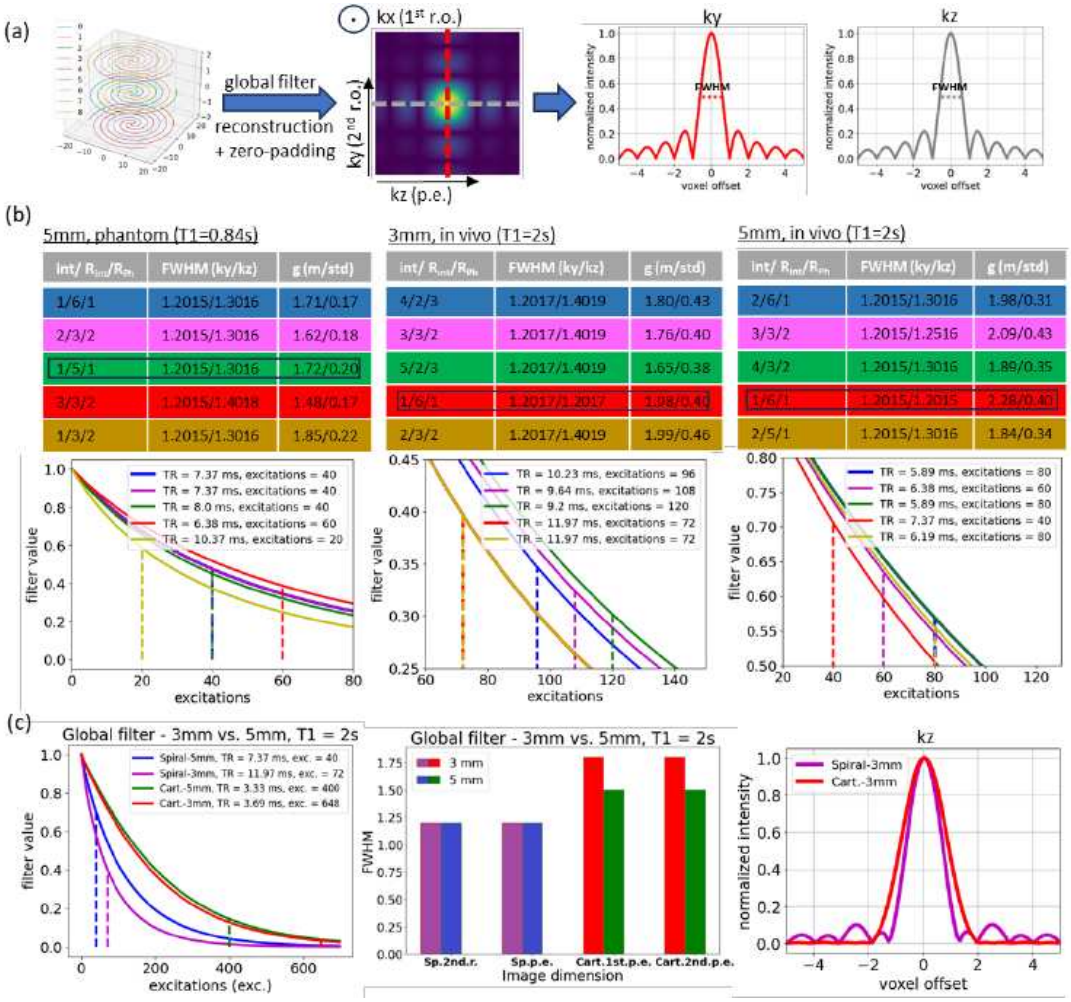

Figure A11: (a) To investigate the STE* decay, a fully sampled k-space of ones was synthesized with different spiral trajectories and the global filter was applied onto each interleaf. The FWHM of the reconstructed, zero-padded point spread function (PSF) shows the STE* blurring effect. (b) Left: Spiral trajectories with different interleaves and accelerations and the color-matched global filter. The abbreviations are as follows: int = accelerated spiral interleaves; Rint = in-plane acceleration; RPh = acceleration in phase-encoding direction. More interleaves lead to a shorter TE and TR, which results in a less significant global filter value decay with increasing excitations. However, more interleaves relate to more excitations, which results in low filter values at high k-space frequencies. This will be handled by using acceleration. The mean (m) and standard deviation (std) of computed g-factor maps with 200 replica are presented. The blurring (see FWHM) is stronger in phase-encoding direction than in readout-direction, especially for 3mm. More interleaves in-plane lead to stronger blurring in phase-encoding direction, even though the total number of excitations (ETL) is the same (see 3mm, in vivo, FWHM of red and yellow curves). (c) Global filter of the in vivo experiment parameters. Left: The Cartesian 3DREAM benefits from shorter TR, but the spiral 3DREAM leads to less filtering at higher frequencies due to less excitations. Right: The spiral 3DREAM has lower blurring especially at 3mm than the Cartesian 3DREAM.

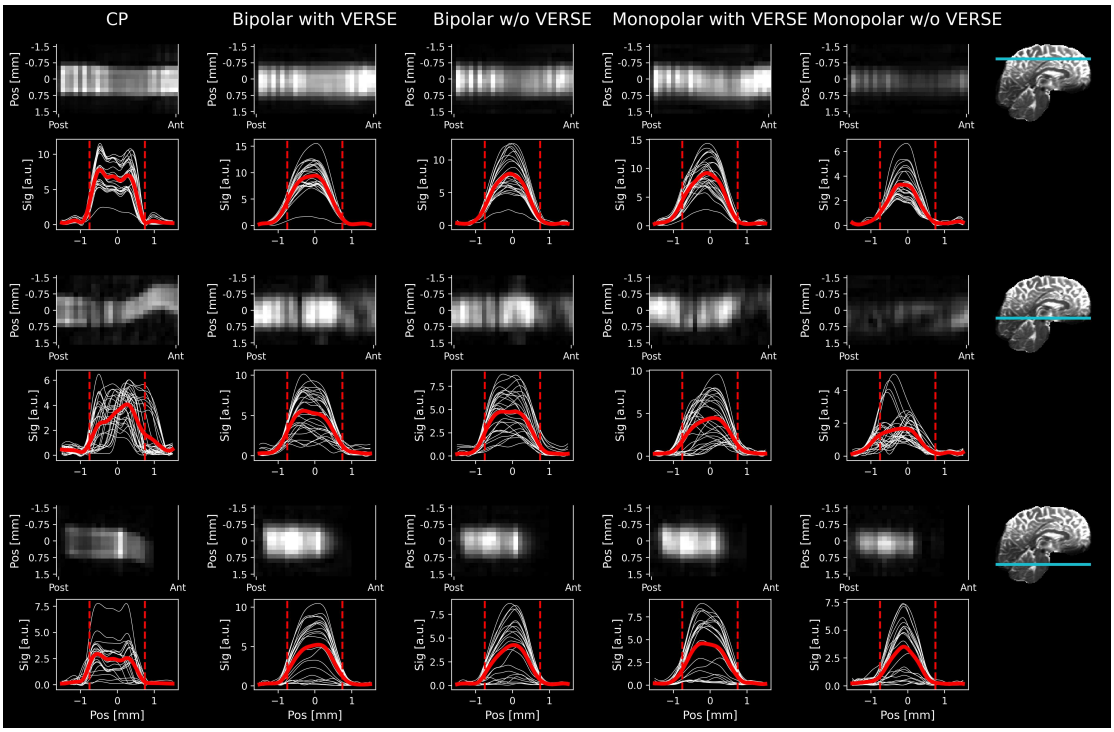

Figure A12: Slice profiles of monopolar and bipolar kT-Spokes pulses with and without VERSE are displayed for three example slices in the upper, middle and lower part of the brain (subject 2, male, 28 years). As a reference, slice profiles of CP pulses are plotted in the first column. Below each slice profile, cross sections along the anterior-posterior are plotted in white and the mean of all cross sections are shown in red. The nominal slice borders are indicated by dotted red lines. In the last column the position of the slice is shown.

Supporting Tables

FIG. 4	Pulseq:	gre_3D_caipi_nonsel_rfspoil_te5.seq (upper) gre_3D_caipi_nonsel_rfspoil_te5_fatimg.seq (lower)
	JEMRIS:	gre_3D_caipi_nonsel_rfspoil_te5.xml (upper) gre_3D_caipi_nonsel_rfspoil_te5_fatimg.xml (lower)
	Reconstruction:	bart_jemris.py
	Raw data/images/metadata available on: https://osf.io/vnh4a/ (DOI 10.17605/OSF.IO/VNH4A) or on request due to large file size.	
FIG. 5	Pulseq:	gre_3D_caipi_nonsel_te25.seq (upper) gre_3D_nocaipi_nonsel_te25.seq (lower)
	JEMRIS:	gre_3D_caipi_nonsel_te25.xml (upper) gre_3D_nocaipi_nonsel_te25.xml (lower)
	Reconstruction:	bart_jemris.py
	Raw data/images/metadata available on: https://osf.io/vnh4a/ (DOI 10.17605/OSF.IO/VNH4A) or on request due to large file size.	
FIG 6.	Pulseq:	gre_b0mapping_4e1a6.seq
	Metadata:	gre_b0mapping_4e1a6.h5
	Raw data:	raw_gre_b0mapping.h5
	Image data:	b0mapping.h5
	Seq. source:	write_cartesian.py
	Reconstruction:	bart_pulseq_cartesian.py
FIG 7.	Sequences:	spiralout_gre_jemris.seq (a), spiralout_gre_fatsat_7T_15f2a.seq (b+c), spiralout_gre_fatsat_3T_d9aac.seq (d+e), spiralout_gre_fatsat_3T_GE_9e1f5.seq (f)
	Metadata:	spiralout_gre_jemris.h5 (a), spiralout_gre_fatsat_7T_15f2a.h5 (b+c), spiralout_gre_fatsat_3T_d9aac.h5 (d+e), spiralout_gre_fatsat_3T_GE_9e1f5.h5 (f)
	Raw data:	raw_spiralout_gre_jemris.h5 (a), raw_spiralout_gre_fatsat_7T.h5 (b+c), raw_spiralout_gre_fatsat_3TSkyra.h5 (d), raw_spiralout_gre_fatsat_3TPrisma.h5 (e) raw_spiralout_gre_fatsat_3T_GE_UHP.h5 (f)
	Image data:	spiralout_jemris.h5 (a), spiralout_fatsat_pypulseq_7T.h5 (b) spiralout_fatsat_pypulseq_b0corrected.h5 (c), spiralout_fatsat_pypulseq_3TSkyra.h5 (d), spiralout_fatsat_pypulseq_3TPrisma.h5 (e), spiralout_fatsat_pypulseq_3T_GE_UHP.h5 (f)
	JEMRIS:	spiralout_gre.xml (a)
	Seq. source:	write_spiral.py (b-f)
	Reconstruction:	bart_jemris.py (a) bart_pulseq_spiral.py (b,d,e,f) B0-corrected reonstruction (c): See README on GitHub repo
FIG 8.	JEMRIS:	spiralout_gre.xml
	Raw data:	signals_spiralout_clean_slc30.h5 / signals_spiralout_clean_slc30.h5 (1st col.) signals_spiralout_CS_slc30.h5 / signals_spiralout_CS_slc30.h5 (2nd col.) signals_spiralout_Susc70Mhz_slc30.h5 / signals_spiralout_Susc70Mhz_slc90.h5 (3rd col.)
	Image data:	reco_spiralout_clean_slc30.h5 / reco_spiralout_clean_slc90.h5 (1st col.) reco_spiralout_CS_slc30.h5 / reco_spiralout_CS_slc90.h5 (2nd col.) reco_spiralout_Susc70Mhz_slc30.h5 / reco_spiralout_Susc70Mhz_slc90.h5 (3rd col.)
	Reconstruction:	bart_jemris.py

Table A1: Pulseq sequence, raw data, metadata and image filenames in the GitHub repository linked to the Figures in chapter 3. Additionally, the reconstruction scripts, the sequence source code for PyPulseq sequences and XML files for JEMRIS sequences are listed.

Shell	SNR ratio - WM mask used in chapter 4	SNR ratio - Tight WM mask
b0	1.30	1.31
b6000	1.29	1.28
b30450	1.19	1.20

Table A2: Ratio of the mean SNR measure across all subjects and sessions as in Figure 4.2. The ratios are listed for the white matter (WM) mask used in chapter 4 and a tighter white matter mask. For the tighter mask, a higher threshold of > 0.98 and an additional binary erosion was used to make sure only pure white matter voxels were selected.

Subject	Absolute distance to isocenter (Test) [mm]	Absolute distance to isocenter (Retest) [mm]	Absolute distance Test-Retest [mm]	Bias [μm]
1	26.89	23.63	3.28	0.02
2	15.83	24.70	9.08	0.11
3	27.63	38.24	18.10	-0.04
4	28.25	28.22	1.61	0.09
5	23.67	27.91	12.15	0.10
6	23.26	23.42	5.55	0.11
7	30.19	23.49	10.11	0.34
7*	28.47	32.31	4.22	0.17
8	24.40	32.63	10.00	0.08
9	33.52	35.05	2.90	0.21
10	26.95	29.90	4.91	0.12

Table A3: Absolute distances of the center of the FOV to the scanner's isocenter for both measurements (Test & Retest) and each subject (only spiral datasets). Also, the absolute distances between the centers of the FOV of both measurements, i.e. the difference between the two scan positions are shown. In the last column the respective bias is shown, which is the mean of the differences between Test and Retest for all white matter voxels as in the Bland-Altman plots in Figure 4.7.

volume [l]	T1 [ms]	T2 [ms]	center frequency [MHz]	H20-amount [%]	PVP K30-amount [%]	Agarose-amount [%]	NaCl-amount [%]	conductivity [S/m]	relative permittivity
4.8	840	38	297.217	61.8	36.0	1.5	0.7	0.49	53.66

Table A4: Physical parameters and composition of the phantom used in the phantom experiments.

Image volume			STEAM pulses		Binomial pulses			Acceleration					
resolution	FOV	orientation	α	duration	β	duration	tbp	int	Ph	R_{int}	R_{Ph}	δ	ETL
3 mm (in vivo)	216 mm isotropic	transversal	50 °	400 µs	5 °	200 µs	6	1	72	6	1	5	72
5 mm (phantom)	200 mm isotropic	transversal	50 °	400 µs	5 °	200 µs	6	1	40	5	1	4	40
5 mm (in vivo)	200 mm isotropic	transversal	50 °	400 µs	5 °	200 µs	6	1	40	6	1	5	40
5 mm (RO, in vivo)	200 mm isotropic	transversal	50 °	400 µs	5 °	200 µs	6	1	40	6	1	5	40

spiral 3DREAM timing						GRE reference scan	
$TE_{STE'}$	TE_{FID}	TR	T_M	T_S	TA	resolution	TA
0.88 ms	6.28 ms	11.98 ms	1.70 ms	5.40 ms	0.87 s	4.32 mm	21.59 s
0.72 ms	4.28 ms	8.00 ms	1.42 ms	3.56 ms	0.33 s	5.00 mm	15.49 s
0.72 ms	3.96 ms	7.37 ms	1.42 ms	3.24 ms	0.30 s	5.00 mm	15.49 s
0.72 ms	4.28 ms	7.69 ms	1.42 ms	3.56 ms	0.32 s	5.00 mm	15.49 s

Table A5: Measurement parameters of the spiral 3DREAM sequence for different resolutions. The abbreviations are as follows: tbp = time bandwidth product; int = accelerated spiral interleaves; Ph = phase encoding steps; Rint = in-plane acceleration; RPh = acceleration in phase-encoding direction; δ = CAIPIRINHA shift; ETL = echo train length; TM = mixing time; TS = STEAM preparation pulse interval; TA = acquisition time. “5 mm (RO)" refers to the spiral scan with modified signal separation gradients applied in readout direction.

References

[1] E. O. Stejskal and J. E. Tanner, "Spin Diffusion Measurements: Spin Echoes in the Presence of a Time-Dependent Field Gradient", *The Journal of Chemical Physics*, vol. 42, no. 1, pp. 288–292, 1965.

[2] D. Le Bihan, E. Breton, D. Lallemand, *et al.*, "MR imaging of intravoxel incoherent motions: Application to diffusion and perfusion in neurologic disorders.", *Radiology*, vol. 161, no. 2, pp. 401–407, 1986.

[3] D. K. Jones, "Studying connections in the living human brain with diffusion MRI", *Cortex*, Special Issue on "Brain Hodology - Revisiting Disconnection Approaches to Disorders of Cognitive Function", vol. 44, no. 8, pp. 936–952, 2008.

[4] K. Setsompop, J. Cohen-Adad, B. Gagoski, *et al.*, "Improving diffusion MRI using simultaneous multi-slice echo planar imaging", *NeuroImage*, vol. 63, no. 1, pp. 569–580, 2012.

[5] B. J. Wilm, C. Barmet, S. Gross, *et al.*, "Single-shot spiral imaging enabled by an expanded encoding model: Demonstration in diffusion MRI", *Magnetic Resonance in Medicine*, vol. 77, no. 1, pp. 83–91, 2017.

[6] Y. Lee, B. Wilm, D. Brunner, *et al.*, "On the signal-to-noise ratio benefit of spiral acquisition in diffusion MRI", *Magnetic Resonance in Medicine*, vol. 85, no. 4, pp. 1924–1937, 2021.

[7] R. Pohmann, O. Speck, and K. Scheffler, "Signal-to-noise ratio and MR tissue parameters in human brain imaging at 3, 7, and 9.4 tesla using current receive coil arrays", *Magnetic Resonance in Medicine*, vol. 75, no. 2, pp. 801–809, 2016.

[8] C. Barmet, N. De Zanche, and K. Pruessmann, "Spatiotemporal magnetic field monitoring for MR", *Magnetic Resonance in Medicine*, vol. 60, no. 1, pp. 187–197, 2008.

[9] B. Wilm, C. Barmet, M. Pavan, *et al.*, "Higher Order Reconstruction for MRI in the Presence of Spatiotemporal Field Perturbations", *Magnetic Resonance in Medicine*, vol. 65, no. 6, pp. 1690–1701, 2011.

[10] F. Padormo, A. Beqiri, J. V. Hajnal, *et al.*, "Parallel transmission for ultrahigh-field imaging", *NMR in Biomedicine*, vol. 29, no. 9, pp. 1145–1161, 2016.

[11] I. I. Rabi, J. R. Zacharias, S. Millman, *et al.*, "A New Method of Measuring Nuclear Magnetic Moment", *Physical Review*, vol. 53, no. 4, pp. 318–318, 1938.

[12] F. Bloch, "Nuclear Induction", *Physical Review*, vol. 70, no. 7-8, pp. 460–474, 1946.

[13] E. M. Purcell, H. C. Torrey, and R. V. Pound, "Resonance Absorption by Nuclear Magnetic Moments in a Solid", *Physical Review*, vol. 69, no. 1-2, pp. 37–38, 1946.

[14] M. A. Bernstein, K. F. King, and X. J. Zhou, *Handbook of MRI Pulse Sequences*. Elsevier, 2004.

[15] E. L. Hahn, "Spin Echoes", *Physics Today*, vol. 3, no. 12, pp. 21–21, 1950.

[16] A. Fick, "Ueber Diffusion", *Annalen der Physik*, vol. 170, no. 1, pp. 59–86, 1855.

[17] H. C. Torrey, "Bloch Equations with Diffusion Terms", *Physical Review*, vol. 104, no. 3, pp. 563–565, 1956.

[18] P. J. Basser, J. Mattiello, and D. Lebihan, "Estimation of the Effective Self-Diffusion *Tensor* from the NMR Spin Echo", *Journal of Magnetic Resonance, Series B*, vol. 103, no. 3, pp. 247–254, 1994.

[19] D. A. Porter and R. M. Heidemann, "High resolution diffusion-weighted imaging using readout-segmented echo-planar imaging, parallel imaging and a two-dimensional navigator-based reacquisition", *Magnetic Resonance in Medicine*, vol. 62, no. 2, pp. 468–475, 2009.

[20] T. K. Truong and A. Guidon, "High-resolution multishot spiral diffusion tensor imaging with inherent correction of motion-induced phase errors", *Magnetic Resonance in Medicine*, vol. 71, no. 2, pp. 790–796, 2014.

[21] K. Setsompop, Q. Fan, J. Stockmann, *et al.*, "High-resolution in vivo diffusion imaging of the human brain with generalized slice dithered enhanced resolution: Simultaneous multislice (gSlider-SMS)", *Magnetic Resonance in Medicine*, vol. 79, no. 1, pp. 141–151, 2018.

[22] M. Engström and S. Skare, "Diffusion-weighted 3D multislab echo planar imaging for high signal-to-noise ratio efficiency and isotropic image resolution", *Magnetic Resonance in Medicine*, vol. 70, no. 6, pp. 1507–1514, 2013.

[23] C. Liu, M. E. Moseley, and R. Bammer, "Simultaneous phase correction and SENSE reconstruction for navigated multi-shot DWI with non-cartesian k-space sampling", *Magnetic Resonance in Medicine*, vol. 54, no. 6, pp. 1412–1422, 2005.

[24] N.-k. Chen, A. Guidon, H.-C. Chang, *et al.*, "A robust multi-shot scan strategy for high-resolution diffusion weighted MRI enabled by multiplexed sensitivity-encoding (MUSE)", *NeuroImage*, vol. 72, pp. 41–47, 2013.

[25] D. S. Novikov, V. G. Kiselev, and S. N. Jespersen, "On modeling", *Magnetic Resonance in Medicine*, vol. 79, no. 6, pp. 3172–3193, 2018.

[26] T. E. Conturo, N. F. Lori, T. S. Cull, *et al.*, "Tracking neuronal fiber pathways in the living human brain", *Proceedings of the National Academy of Sciences*, vol. 96, no. 18, pp. 10 422–10 427, 1999.

[27] J. H. Jensen, J. A. Helpern, A. Ramani, *et al.*, "Diffusional kurtosis imaging: The quantification of non-gaussian water diffusion by means of magnetic resonance imaging", *Magnetic Resonance in Medicine*, vol. 53, no. 6, pp. 1432–1440, 2005.

[28] P. P. Mitra, "Multiple wave-vector extensions of the NMR pulsed-field-gradient spin-echo diffusion measurement", *Physical Review B*, vol. 51, no. 21, pp. 15 074–15 078, 1995.

[29] P. T. Callaghan and M. E. Komlosh, "Locally anisotropic motion in a macroscopically isotropic system: Displacement correlations measured using double pulsed gradient spin-echo NMR", *Magnetic Resonance in Chemistry*, vol. 40, no. 13, S15–S19, 2002.

[30] D. Topgaard, "Multidimensional diffusion MRI", *Journal of Magnetic Resonance*, vol. 275, pp. 98–113, 2017.

[31] J. Veraart, E. Fieremans, and D. Novikov, "On the scaling behavior of water diffusion in human brain white matter", *NeuroImage*, vol. 185, pp. 379–387, 2019.

[32] N. Seiberlich, V. Gulani, F. Calamante, *et al.*, Eds., *Quantitative Magnetic Resonance Imaging* (Advances in Magnetic Resonance Technology and Applications). Academic Press, 2020, vol. 1.

[33] M. W. Haskell, J.-F. Nielsen, and D. C. Noll, "Off-resonance artifact correction for MRI: A review", *NMR in Biomedicine*, vol. 36, no. 5, e4867, 2023.

[34] J. F. Schenck, "The role of magnetic susceptibility in magnetic resonance imaging: MRI magnetic compatibility of the first and second kinds", *Medical Physics*, vol. 23, no. 6, pp. 815–850, 1996.

[35] C. Hutton, A. Bork, O. Josephs, *et al.*, "Image Distortion Correction in fMRI: A Quantitative Evaluation", *NeuroImage*, vol. 16, no. 1, pp. 217–240, 2002.

[36] Y. Geiger and A. Tal, "Optimal echo times for multi-gradient echo-based B $_0$ field-mapping", *NMR in Biomedicine*, vol. 33, no. 7, e4316, 2020.

[37] H. Abdul-Rahman, M. Arevalillo-Herráez, M. Gdeisat, *et al.*, "Robust three-dimensional best-path phase-unwrapping algorithm that avoids singularity loops", *Applied Optics*, vol. 48, no. 23, pp. 4582–4596, 2009.

[38] B. Dymerska, K. Eckstein, B. Bachrata, *et al.*, "Phase unwrapping with a rapid opensource minimum spanning tree algorithm (ROMEO)", *Magnetic Resonance in Medicine*, vol. 85, no. 4, pp. 2294–2308, 2021.

[39] T. A. Bley, O. Wieben, C. J. François, *et al.*, "Fat and water magnetic resonance imaging", *Journal of Magnetic Resonance Imaging*, vol. 31, no. 1, pp. 4–18, 2010.

[40] S. Robinson and J Jovicich, "B0 mapping with multi-channel RF coils at high field", *Magnetic Resonance in Medicine*, vol. 66, no. 4, pp. 976–988, 2011.

[41] J. Liu, J. A. De Zwart, P. Van Gelderen, *et al.*, "Effect of head motion on MRI B_0 field distribution", *Magnetic Resonance in Medicine*, vol. 80, no. 6, pp. 2538–2548, 2018.

[42] C. Boesch, R. Gruetter, and E. Martin, "Temporal and spatial analysis of fields generated by eddy currents in superconducting magnets: Optimization of corrections and quantitative characterization of magnet/gradient systems", *Magnetic Resonance in Medicine*, vol. 20, no. 2, pp. 268–284, 1991.

[43] B. U. Foerster, D. Tomasi, and E. C. Caparelli, "Magnetic field shift due to mechanical vibration in functional magnetic resonance imaging", *Magnetic Resonance in Medicine*, vol. 54, no. 5, pp. 1261–1267, 2005.

[44] M. Stich, C. Pfaff, T. Wech, *et al.*, "The Temperature Dependence of Gradient System Response Characteristics", *Magnetic Resonance in Medicine*, vol. 83, no. 4, pp. 1519–1527, 2020.

[45] D. G. Norris and J. M. Hutchison, "Concomitant magnetic field gradients and their effects on imaging at low magnetic field strengths", *Magnetic Resonance Imaging*, vol. 8, no. 1, pp. 33–37, 1990.

[46] N. De Zanche, C. Barmet, J. A. Nordmeyer-Massner, *et al.*, "NMR Probes for measuring magnetic fields and field dynamics in MR systems", *Magnetic Resonance in Medicine*, vol. 60, no. 1, pp. 176–186, 2008.

[47] C. M. Collins, W. Liu, W. Schreiber, *et al.*, "Central brightening due to constructive interference with, without, and despite dielectric resonance", *Journal of Magnetic Resonance Imaging*, vol. 21, no. 2, pp. 192–196, 2005.

[48] L. I. Sacolick, F. Wiesinger, I. Hancu, *et al.*, "B_1 mapping by Bloch-Siegert shift", *Magnetic Resonance in Medicine*, vol. 63, no. 5, pp. 1315–1322, 2010.

[49] V. L. Yarnykh, "Actual flip-angle imaging in the pulsed steady state: A method for rapid three-dimensional mapping of the transmitted radiofrequency field", *Magnetic Resonance in Medicine*, vol. 57, no. 1, pp. 192–200, 2007.

[50] K. Nehrke, M. J. Versluis, A. Webb, *et al.*, "Volumetric B1+ mapping of the brain at 7T using DREAM", *Magnetic Resonance in Medicine*, vol. 71, no. 1, pp. 246–256, 2014.

[51] V. Gras, A. Vignaud, A. Amadon, *et al.*, "Universal pulses: A new concept for calibration-free parallel transmission", *Magnetic Resonance in Medicine*, vol. 77, no. 2, pp. 635–643, 2017.

[52] W. Perman, S. Hilal, H. Simon, *et al.*, "Contrast manipulation in NMR imaging", *Magnetic Resonance Imaging*, vol. 2, no. 1, pp. 23–32, 1984.

[53] K Setsompop, R Kimmlingen, E Eberlein, *et al.*, "Pushing the limits of in vivo diffusion MRI for the Human Connectome Project", *NeuroImage*, vol. 80, pp. 220–233, 2013.

[54] R. Turner, D. Le Bihan, and A. Scott Chesnicks, "Echo-planar imaging of diffusion and perfusion", *Magnetic Resonance in Medicine*, vol. 19, no. 2, pp. 247–253, 1991.

[55] G. H. Glover, "Simple analytic spiral K-space algorithm", *Magnetic Resonance in Medicine*, vol. 42, no. 2, pp. 412–415, 1999.

[56] G. H. Glover and S. Lai, "Self-navigated spiral fMRI: Interleaved versus single-shot", *Magnetic Resonance in Medicine*, vol. 39, no. 3, pp. 361–368, 1998.

[57] A. Deshmane, V. Gulani, M. A. Griswold, *et al.*, "Parallel MR imaging", *Journal of Magnetic Resonance Imaging*, vol. 36, no. 1, pp. 55–72, 2012.

[58] M. Uecker, P. Lai, M. J. Murphy, *et al.*, "ESPIRiT - An eigenvalue approach to autocalibrating parallel MRI: Where SENSE meets GRAPPA", *Magnetic Resonance in Medicine*, vol. 71, no. 3, pp. 990–1001, 2014.

[59] K. P. Pruessmann, M. Weiger, M. B. Scheidegger, *et al.*, "SENSE: Sensitivity encoding for fast MRI", *Magnetic Resonance in Medicine*, vol. 42, no. 5, pp. 952–962, 1999.

[60] C. A. McKenzie, E. N. Yeh, M. A. Ohliger, *et al.*, "Self-calibrating parallel imaging with automatic coil sensitivity extraction", *Magnetic Resonance in Medicine*, vol. 47, no. 3, pp. 529–538, 2002.

[61] M. Barth, F. Breuer, P. J. Koopmans, *et al.*, "Simultaneous multislice (SMS) imaging techniques", *Magnetic Resonance in Medicine*, vol. 75, no. 1, pp. 63–81, 2016.

[62] B. Zahneisen, B. A. Poser, T. Ernst, *et al.*, "Three-dimensional Fourier encoding of simultaneously excited slices: Generalized acquisition and reconstruction framework", *Magnetic Resonance in Medicine*, vol. 71, no. 6, pp. 2071–2081, 2014.

[63] J. Pauly, P. Le Roux, D. Nishimura, *et al.*, "Parameter relations for the Shinnar-Le Roux selective excitation pulse design algorithm (NMR imaging)", *IEEE Transactions on Medical Imaging*, vol. 10, no. 1, pp. 53–65, 1991.

[64] M. Shinnar, L. Bolinger, and J. S. Leigh, "The use of finite impulse response filters in pulse design", *Magnetic Resonance in Medicine*, vol. 12, no. 1, pp. 81–87, 1989.

[65] S. Conolly, D. Nishimura, and A. Macovski, "Variable-Rate Selective Excitation", *Journal of Magnetic Resonance*, vol. 78, no. 3, pp. 440–458, 1988.

[66] B. Hargreaves, C. Cunningham, D. Nishimura, *et al.*, "Variable-rate selective excitation for rapid MRI sequences", *Magnetic Resonance in Medicine*, vol. 52, no. 3, pp. 590–597, 2004.

[67] K. Pruessmann, M. Weiger, P. Börnert, *et al.*, "Advances in sensitivity encoding with arbitrary k-space trajectories", *Magnetic Resonance in Medicine*, vol. 46, no. 4, pp. 638–651, 2001.

[68] J. D. O'Sullivan, "A Fast Sinc Function Gridding Algorithm for Fourier Inversion in Computer Tomography", *IEEE Transactions on Medical Imaging*, vol. 4, no. 4, pp. 200–207, 1985.

[69] J. I. Jackson, C. H. Meyer, D. G. Nishimura, *et al.*, "Selection of a Convolution Function for Fourier Inversion Using Gridding", *IEEE Transactions on Medical Imaging*, vol. 10, no. 3, pp. 473–478, 1991.

[70] J. G. Pipe and P. Menon, "Sampling density compensation in MRI: Rationale and an iterative numerical solution", *Magnetic Resonance in Medicine*, vol. 41, no. 1, pp. 179–186, 1999.

[71] A. Maeda, K. Sano, and T. Yokoyama, "Reconstruction by weighted correlation for MRI with time-varying gradients", *IEEE Transactions on Medical Imaging*, vol. 7, no. 1, pp. 26–31, 1988.

[72] A. Macovski, "Volumetric NMR imaging with time-varying gradients", *Magnetic Resonance in Medicine*, vol. 2, no. 1, pp. 29–40, 1985.

[73] D. C. Noll, C. H. Meyer, J. M. Pauly, *et al.*, "A Homogeneity Correction Method for Magnetic Resonance Imaging with Time-Varying Gradients", *IEEE Transactions on Medical Imaging*, vol. I, no. 4, 1991.

[74] L.-C. Man, J. M. Pauly, and A. Macovski, "Multifrequency Interpolation for Fast Off-Resonance Correction", *Magnetic Resonance in Medicine*, vol. 37, no. 5, pp. 785–792, 1997.

[75] ISMRM Reproducible Research Study Group, *MR-Hub Website*. [Online]. Available: `https://www.ismrm.org/mri_unbound/` (visited on 04/25/2022).

[76] *Open Source Imaging Initiative*. [Online]. Available: `https://www.opensourceimaging.org/` (visited on 02/01/2022).

[77] O. Maier, S. H. Baete, A. Fyrdahl, *et al.*, "CG-SENSE revisited: Results from the first ISMRM reproducibility challenge", *Magnetic Resonance in Medicine*, vol. 85, no. 4, pp. 1821–1839, 2021.

[78] K. Layton, S. Kroboth, F. Jia, *et al.*, "Pulseq: A rapid and hardware-independent pulse sequence prototyping framework", *Magnetic Resonance in Medicine*, vol. 77, no. 4, pp. 1544–1552, 2017.

[79] J.-F. Nielsen and D. C. Noll, "TOPPE: A framework for rapid prototyping of MR pulse sequences", *Magnetic Resonance in Medicine*, vol. 79, no. 6, pp. 3128–3134, 2018.

[80] M. S. Hansen and T. S. Sørensen, "Gadgetron: An open source framework for medical image reconstruction", *Magnetic Resonance in Medicine*, vol. 69, no. 6, pp. 1768–1776, 2013.

[81] S. Inati, J. Naegele, N. Zwart, *et al.*, "ISMRM Raw data format: A proposed standard for MRI raw datasets", *Magnetic Resonance in Medicine*, vol. 77, no. 1, pp. 411–421, 2017.

[82] *NIfTI neuroimaging informatics technology initiative. National Institute of Mental Health website.* [Online]. Available: `http://nifti.nimh.nih.gov` (visited on 05/02/2022).

[83] M. Uecker, J. I. Tamir, F. Ong, *et al.*, "The BART Toolbox for Computational Magnetic Resonance Imaging", in *Proceedings of the International Society for Magnetic Resonance in Medicine*, vol. 24, 2016.

[84] T. Stöcker, K. Vahedipour, D. Pflugfelder, *et al.*, "High-Performance Computing MRI Simulations", *Magnetic Resonance in Medicine*, vol. 64, no. 1, pp. 186–193, 2010.

[85] *JEMRIS Website*. [Online]. Available: `www.jemris.org` (visited on 02/22/2022).

[86] *Pulseq Website*. [Online]. Available: `pulseq.github.io/` (visited on 02/08/2022).

[87] K. Ravi, S. Geethanath, and J. Vaughan, "PyPulseq: A Python Package for MRI Pulse Sequence Design", *Journal of Open Source Software*, vol. 4, no. 42, p. 1725, 2019.

[88] M. Lustig, S. Kim, and J. Pauly, "A fast method for designing time-optimal gradient waveforms for arbitrary k-space trajectories", *IEEE Transactions on Medical Imaging*, vol. 27, no. 6, pp. 866–873, 2008.

[89] K. Chow, P. Grant, and H Xue, "Prototyping Image Reconstruction and Analysis with FIRE", in *Proceedings from the 24th Annual SCMR Scientific Sessions*, 2021.

[90] S. J. Vannesjo, N. N. Graedel, L. Kasper, *et al.*, "Image reconstruction using a gradient impulse response model for trajectory prediction", *Magnetic Resonance in Medicine*, vol. 76, no. 1, pp. 45–58, 2016.

[91] F. A. Breuer, M. Blaimer, M. F. Mueller, *et al.*, "Controlled aliasing in volumetric parallel imaging (2D CAIPIRINHA).", *Magnetic Resonance in Medicine*, vol. 55, no. 3, pp. 549–56, 2006.

[92] *TOPPE Website*. [Online]. Available: `https://toppemri.github.io/` (visited on 05/02/2022).

[93] A. Fortin, S. Salmon, J. Baruthio, *et al.*, "Flow MRI simulation in complex 3D geometries: Application to the cerebral venous network", *Magnetic Resonance in Medicine*, vol. 80, no. 4, pp. 1655–1665, 2018.

[94] S. Van Der Walt, J. L. Schönberger, J. Nunez-Iglesias, *et al.*, "Scikit-image: Image processing in python", *PeerJ*, vol. 2014, no. 1, pp. 1–18, 2014.

[95] P. Virtanen, R. Gommers, T. E. Oliphant, *et al.*, "SciPy 1.0: Fundamental Algorithms for Scientific Computing in Python", *Nature Methods*, vol. 17, pp. 261–272, 2020.

[96] A. Cerjanic, J. L. Holtrop, G. C. Ngo, *et al.*, "PowerGrid: A open source library for accelerated iterative magnetic resonance image reconstruction", *Proceedings of the International Society for Magnetic Resonance in Medicine*, vol. 24, p. 525, 2016.

[97] B. P. Sutton, D. C. Noll, and J. A. Fessler, "Fast, iterative image reconstruction for MRI in the presence of field inhomogeneities", *IEEE Transactions on Medical Imaging*, vol. 22, no. 2, pp. 178–188, 2003.

[98] F. Ong and M. Lustig, "SigPy: A Python Package for High Performance Iterative Reconstruction", in *Proceedings of the International Society for Magnetic Resonance in Medicine*, vol. 27, 2019.

[99] M. Loecher, M. J. Middione, and D. B. Ennis, "A gradient optimization toolbox for general purpose time-optimal MRI gradient waveform design", *Magnetic Resonance in Medicine*, vol. 84, no. 6, pp. 3234–3245, 2020.

[100] G. Tong, S. Geethanath, and J. T. J. Vaughan, "Bridging Open Source Sequence Simulation and Acquisition with py2jemris", *Proceedings of the International Society for Magnetic Resonance in Medicine*, vol. 29, 2021.

[101] S. Waxman, "Determinants of conduction velocity in myelinated nerve fibers", *Muscle & Nerve*, vol. 3, no. 2, pp. 141–150, 1980.

[102] T. Kuhlmann, G. Lingfeld, A. Bitsch, *et al.*, "Acute axonal damage in multiple sclerosis is most extensive in early disease stages and decreases over time", *Brain*, vol. 125, no. 10, pp. 2202–2212, 2002.

[103] Y. Assaf, T. Blumenfeld-Katzir, Y. Yovel, *et al.*, "Axcaliber: A method for measuring axon diameter distribution from diffusion MRI", *Magnetic Resonance in Medicine*, vol. 59, no. 6, pp. 1347–1354, 2008.

[104] D. Alexander, P. Hubbard, M. Hall, *et al.*, "Orientationally invariant indices of axon diameter and density from diffusion MRI", *NeuroImage*, vol. 52, no. 4, pp. 1374–1389, 2010.

[105] S. Huang, A. Nummenmaa, T. Witzel, *et al.*, "The impact of gradient strength on in vivo diffusion MRI estimates of axon diameter", *NeuroImage*, vol. 106, pp. 464–472, 2015.

[106] J Veraart, D Nunes, U Rudrapatna, *et al.*, "Noninvasive quantification of axon radii using diffusion MRI", *eLife*, vol. 9, e49855, 2020.

[107] M. Nilsson, S. Lasič, I. Drobnjak, *et al.*, "Resolution limit of cylinder diameter estimation by diffusion MRI: The impact of gradient waveform and orientation dispersion", *NMR in Biomedicine*, vol. 30, no. 7, e3711, 2017.

[108] F. Aboitiz, A. Scheibel, R. Fisher, *et al.*, "Fiber composition of the human corpus callosum", *Brain Research*, vol. 598, no. 1-2, pp. 143–153, 1992.

[109] L. Burcaw, E. Fieremans, and D. Novikov, "Mesoscopic structure of neuronal tracts from time-dependent diffusion", *NeuroImage*, vol. 114, pp. 18–37, 2015.

[110] J. Andersson and S. Sotiropoulos, "An integrated approach to correction for off-resonance effects and subject movement in diffusion MR imaging", *NeuroImage*, vol. 125, pp. 1063–1078, 2016.

[111] J Veraart, EP Raven, LJ Edwards, *et al.*, "The variability of MR axon radii estimates in the human white matter", *Human Brain Mapping*, vol. 42, pp. 2201–2213, 2021.

[112] M. Veldmann, P. Ehses, K. Chow, *et al.*, "Open-source imaging and reconstruction workflow", *Magnetic Resonance in Medicine*, vol. 88, no. 6, pp. 2395–2407, 2022.

[113] BE Dietrich, DO Brunner, B. J. Wilm, *et al.*, "A field camera for MR sequence monitoring and system analysis", *Magnetic Resonance in Medicine*, vol. 75, no. 4, pp. 1831–1840, 2016.

[114] E. Kellner, B. Dhital, V. Kiselev, *et al.*, "Gibbs-ringing artifact removal based on local subvoxel-shifts: Gibbs-Ringing Artifact Removal", *Magnetic Resonance in Medicine*, vol. 76, no. 5, pp. 1574–1581, 2016.

[115] J. Andersson, M. Graham, I. Drobnjak, *et al.*, "Towards a comprehensive framework for movement and distortion correction of diffusion MR images: Within volume movement", *NeuroImage*, vol. 152, pp. 450–466, 2017.

[116] J. Andersson, M. Graham, E. Zsoldos, *et al.*, "Incorporating outlier detection and replacement into a non-parametric framework for movement and distortion correction of diffusion MR images", *NeuroImage*, vol. 141, pp. 556–572, 2016.

[117] A. Janke, H. Zhao, G. Cowin, *et al.*, "Use of spherical harmonic deconvolution methods to compensate for nonlinear gradient effects on MRI images", *Magnetic Resonance in Medicine*, vol. 52, no. 1, pp. 115–122, 2004.

[118] J. Sijbers, A. Den Dekker, P. Scheunders, *et al.*, "Maximum-likelihood estimation of Rician distribution parameters", *IEEE Transactions on Medical Imaging*, vol. 17, no. 3, pp. 357–361, 1998.

[119] L. Cordero-Grande, D. Christiaens, J. Hutter, *et al.*, "Complex diffusion-weighted image estimation via matrix recovery under general noise models", *NeuroImage*, vol. 200, pp. 391–404, 2019.

[120] M. Jenkinson, P. Bannister, M. Brady, *et al.*, "Improved Optimization for the Robust and Accurate Linear Registration and Motion Correction of Brain Images", *NeuroImage*, vol. 17, no. 2, pp. 825–841, 2002.

[121] N. Tustison, P. Cook, A. Holbrook, *et al.*, "The ANTsX ecosystem for quantitative biological and medical imaging", *Scientific Reports*, vol. 11, no. 1, p. 9068, 2021.

[122] M. Afzali, H. Knutsson, E. Özarslan, *et al.*, "Computing the orientational-average of diffusion-weighted MRI signals: A comparison of different techniques", *Scientific Reports*, vol. 11, no. 1, p. 14 345, 2021.

[123] R. Bammer, M. Markl, A. Barnett, *et al.*, "Analysis and generalized correction of the effect of spatial gradient field distortions in diffusion-weighted imaging", *Magnetic Resonance in Medicine*, vol. 50, no. 3, pp. 560–569, 2003.

[124] M. Paquette, C. Eichner, and A. Anwander, "Gradient Non-Linearity Correction for Spherical Mean Diffusion Imaging", *Proceedings of the International Society for Magnetic Resonance in Medicine*, vol. 27, p. 550, 2019.

[125] Y. Zhang, M. Brady, and S. Smith, "Segmentation of brain MR images through a hidden Markov random field model and the expectation-maximization algorithm", *IEEE Transactions on Medical Imaging*, vol. 20, no. 1, pp. 45–57, 2001.

[126] A. Hammers, R. Allom, M. Koepp, *et al.*, "Three-dimensional maximum probability atlas of the human brain, with particular reference to the temporal lobe", *Hum Brain Mapp*, vol. 19, no. 4, pp. 224–247, 2003.

[127] J. Yeatman, R. Dougherty, N. Myall, *et al.*, "Tract Profiles of White Matter Properties: Automating Fiber-Tract Quantification", *PLoS ONE*, vol. 7, no. 11, e49790, 2012.

[128] E. Garyfallidis, M. Brett, B. Amirbekian, *et al.*, "Dipy, a library for the analysis of diffusion MRI data", *Frontiers in Neuroinformatics*, vol. 8, 2014.

[129] J. Kruper, J. Yeatman, A. Richie-Halford, *et al.*, "Evaluating the Reliability of Human Brain White Matter Tractometry", *Aperture Neuro*, vol. 2021, no. 1, p. 25, 2021.

[130] J. Tournier, F. Calamante, and A. Connelly, "Improved probabilistic streamlines tractography by 2nd order integration over fibre orientation distributions", *Proceedings of the International Society for Magnetic Resonance in Medicine*, vol. 18, p. 1670, 2010.

[131] B. Jeurissen, J. Tournier, T. Dhollander, *et al.*, "Multi-tissue constrained spherical deconvolution for improved analysis of multi-shell diffusion MRI data", *NeuroImage*, vol. 103, pp. 411–426, 2014.

[132] J. Tournier, R. Smith, D. Raffelt, *et al.*, "MRtrix3: A fast, flexible and open software framework for medical image processing and visualisation", *NeuroImage*, vol. 202, p. 116 137, 2019.

[133] E. McKinnon and J. Jensen, "Measuring intra-axonal T $_2$ in white matter with direction-averaged diffusion MRI", *Magnetic Resonance in Medicine*, vol. 81, no. 5, pp. 2985–2994, 2019.

[134] M. Pizzolato, M. Andersson, E. Canales-Rodríguez, *et al.*, "Axonal T2 estimation using the spherical variance of the strongly diffusion-weighted MRI signal", *Magnetic Resonance in Medicine*, vol. 86, pp. 118–134, 2022.

[135] G. Varela-Mattatall, P. Dubovan, T. Santini, *et al.*, "Single-shot spiral diffusion-weighted imaging at 7T using expanded encoding with compressed sensing", *Magnetic Resonance in Medicine*, vol. 90, no. 2, pp. 615–623, 2023.

[136] B. Wilm, Z. Nagy, C. Barmet, *et al.*, "Diffusion MRI with concurrent magnetic field monitoring", *Magnetic Resonance in Medicine*, vol. 74, no. 4, pp. 925–933, 2015.

[137] R. Ma, M. Akçakaya, S. Moeller, *et al.*, "A field-monitoring-based approach for correcting eddy-current-induced artifacts of up to the 2nd spatial order in human-connectome-project-style multiband diffusion MRI experiment at 7T: A pilot study", *NeuroImage*, vol. 216, p. 116 861, 2020.

[138] G. Ramos-Llordén, D. Park, J. Kirsch, *et al.*, "Eddy current-induced artifact correction in high b-value ex vivo human brain diffusion MRI with dynamic field monitoring", *Magnetic Resonance in Medicine*, vol. 91, no. 2, pp. 541–557, 2024.

[139] S. Feizollah and C. L. Tardif, "High-resolution diffusion-weighted imaging at 7 Tesla: Single-shot readout trajectories and their impact on signal-to-noise ratio, spatial resolution and accuracy", *NeuroImage*, vol. 274, p. 120 159, 2023.

[140] S. Huang, Q. Tian, Q. Fan, *et al.*, "High-gradient diffusion MRI reveals distinct estimates of axon diameter index within different white matter tracts in the in vivo human brain", *Brain Structure and Function*, vol. 225, no. 4, pp. 1277–1291, 2020.

[141] J Veraart, DS Novikov, D Christiaens, *et al.*, "Denoising of diffusion MRI using random matrix theory", *NeuroImage*, vol. 142, pp. 394–406, 2016.

[142] D. Lakens, "Calculating and reporting effect sizes to facilitate cumulative science: A practical primer for t-tests and ANOVAs", *Frontiers in Psychology*, vol. 4, 2013.

[143] F. Faul, E. Erdfelder, A. Buchner, *et al.*, "Statistical power analyses using G*Power 3.1: Tests for correlation and regression analyses", *Behavior Research Methods*, vol. 41, no. 4, pp. 1149–1160, 2009.

[144] S. Vos, C. Tax, P. Luijten, *et al.*, "The importance of correcting for signal drift in diffusion MRI", *Magnetic Resonance in Medicine*, vol. 77, no. 1, pp. 285–299, 2017.

[145] Q. Fan, C. Eichner, M. Afzali, *et al.*, "Mapping the human connectome using diffusion MRI at 300 mT/m gradient strength: Methodological advances and scientific impact", *NeuroImage*, vol. 254, p. 118 958, 2022.

[146] B. Slayman, K. King, and P. Licato, *Nutation angle measurement during MRI prescan.* US Patent 5,416,412. May 16, 1995.

[147] B. Shah, S. Anderson, J. Scalera, *et al.*, "Quantitative MR imaging: Physical principles and sequence design in abdominal imaging", *Radiographics : a review publication of the Radiological Society of North America, Inc*, vol. 31, no. 3, pp. 867–880, 2011.

[148] U. Katscher and P. Börnert, "Parallel RF transmission in MRI", *NMR in Biomedicine*, vol. 19, no. 3, pp. 393–400, 2006.

[149] R. Stollberger, P. Wach, G. McKinnon, *et al.*, "RF-field mapping in vivo.", in *Proceedings of the Society of Magnetic Resonance in Medicine*, vol. 7, 1988, p. 106.

[150] C. Cunningham, J. Pauly, and K. Nayak, "Saturated double-angle method for rapid B1+ mapping", *Magnetic Resonance in Medicine*, vol. 55, no. 6, pp. 1326–1333, 2006.

[151] D. Zhu, M Schär, and Q. Qin, "Ultrafast B1 mapping with RF-prepared 3D FLASH acquisition: Correcting the bias due to T1-induced k-space filtering effect", *Magnetic Resonance in Medicine*, vol. 88, no. 2, pp. 757–769, 2022.

[152] G. Morrell, "A phase-sensitive method of flip angle mapping", *Magnetic Resonance in Medicine*, vol. 60, no. 4, pp. 889–894, 2008.

[153] S. Akoka, F. Franconi, F. Seguin, *et al.*, "Radiofrequency map of an NMR coil by imaging", *Magnetic Resonance Imaging*, vol. 11, no. 3, pp. 437–441, 1993.

[154] F. Jiru and U Klose, "Fast 3D radiofrequency field mapping using echo-planar imaging", *Magnetic Resonance in Medicine*, vol. 56, no. 6, pp. 1375–1379, 2006.

[155] G. Helms, J Finsterbusch, N. Weiskopf, *et al.*, "Rapid radiofrequency field mapping in vivo using single-shot STEAM MRI", *Magnetic Resonance in Medicine*, vol. 60, no. 3, pp. 739–743, 2008.

[156] K. Nehrke and P. Börnert, "Fast B1 mapping using a STEAM-based bloch-siegert preparation pulse.", in *Proceedings of the International Society for Magnetic Resonance in Medicine*, vol. 19, 2011, p. 4411.

[157] K. Nehrke and P. Börnert, "DREAM-a novel approach for robust, ultrafast, multislice B1 mapping", *Magnetic Resonance in Medicine*, vol. 68, no. 5, pp. 1517–1526, 2012.

[158] P. Ehses, D. Brenner, R. Stirnberg, *et al.*, "Whole-brain B1-mapping using three-dimensional DREAM", *Magnetic Resonance in Medicine*, vol. 82, no. 3, pp. 924–934, 2019.

[159] J. Tsao, "Ultrafast imaging: Principles, pitfalls, solutions, and applications", *Journal of Magnetic Resonance Imaging*, vol. 32, no. 2, pp. 252–266, 2010.

[160] D. McRobbie, E. Moore, M. Graves, *et al.*, "Acronyms anonymous I: Spin echo", in *MRI from Picture to Proton*, Cambridge: Cambridge University Press, 2017, pp. 185–206.

[161] M. Voelker, O. Kra, O. Speck, *et al.*, "Quality Assurance Phantoms and Procedures for UHF MRI - The German Ultrahigh Field Imaging (GUFI) Approach.", in *Proceedings of the International Society for Magnetic Resonance in Medicine*, vol. 26, 2017, p. 3912.

[162] F. Breuer, M. Blaimer, R. Heidemann, *et al.*, "Controlled aliasing in parallel imaging results in higher acceleration (CAIPIRINHA) for multi-slice imaging.", *Magnetic Resonance in Medicine*, vol. 53, no. 3, pp. 684–91, 2005.

[163] S. Smith, "Fast robust automated brain extraction", *Human Brain Mapping*, vol. 17, no. 3, pp. 143–155, 2002.

[164] T. Koo and M. Li, "A Guideline of Selecting and Reporting Intraclass Correlation Coefficients for Reliability Research", *Journal of Chiropractic Medicine*, vol. 15, no. 2, pp. 155–163, 2016.

[165] Y. Han, H. Du, F. Lam, *et al.*, "Image reconstruction using analysis model prior", *Computational and Mathematical Methods in Medicine*, vol. 2016, no. 1, 2016.

[166] S. J. Vannesjo, M. Haeberlin, L. Kasper, *et al.*, "Gradient system characterization by impulse response measurements with a dynamic field camera", *Magnetic Resonance in Medicine*, vol. 69, no. 2, pp. 583–593, 2013.

[167] B. Jeurissen, M. Descoteaux, S. Mori, *et al.*, "Diffusion MRI fiber tractography of the brain", *NMR in Biomedicine*, vol. 32, no. 4, e3785, 2019.

[168] D. S. Novikov, E. Fieremans, S. N. Jespersen, *et al.*, "Quantifying brain microstructure with diffusion MRI: Theory and parameter estimation", *NMR in Biomedicine*, vol. 32, no. 4, e3998, 2019.

[169] E. F. Cox and P. A. Gowland, "Measuring T2 and T2' in the brain at 1.5T, 3T and 7T using a hybrid gradient echo-spin echo sequence and EPI", in *Proceedings of the International Society for Magnetic Resonance in Medicine*, vol. 16, 2008, p. 1411.

[170] B. Ding, S. N. Williams, I. Dragonu, *et al.*, "Slice-specific B shimming improves the repeatability of multishot DWI at 7 T", *Magnetic Resonance in Medicine*, vol. Early View, 2024.

[171] M. Zhang, B. Ding, I. Dragonu, *et al.*, "Dynamic parallel transmit diffusion MRI at 7T", *Magnetic Resonance Imaging*, vol. 111, pp. 35–46, 2024.

[172] V. Gras, B. A. Poser, X. Wu, *et al.*, "Optimizing BOLD sensitivity in the 7T Human Connectome Project resting-state fMRI protocol using plug-and-play parallel transmission", *NeuroImage*, vol. 195, pp. 1–10, 2019.

[173] G. Saïb, V. Gras, F. Mauconduit, *et al.*, "kT-spokes: Combining kT-points with spokes to ease ramp pulse design for TOF slab selection with parallel transmission at 7T", in *Proceedings of the International Society for Magnetic Resonance in Medicine*, vol. 26, 2018, p. 2690.

[174] L. Van Damme, F. Mauconduit, T. Chambrion, *et al.*, "Universal nonselective excitation and refocusing pulses with improved robustness to off-resonance for Magnetic Resonance Imaging at 7 Tesla with parallel transmission", *Magnetic Resonance in Medicine*, vol. 85, no. 2, pp. 678–693, 2021.

[175] N. Khaneja, T. Reiss, C. Kehlet, *et al.*, "Optimal control of coupled spin dynamics: Design of NMR pulse sequences by gradient ascent algorithms", *Journal of Magnetic Resonance*, vol. 172, no. 2, pp. 296–305, 2005.

[176] D. Jones, M. Horsfield, and A. Simmons, "Optimal strategies for measuring diffusion in anisotropic systems by magnetic resonance imaging", *Magnetic Resonance in Medicine*, vol. 42, no. 3, pp. 515–525, 1999.

[177] B. Zahneisen, B. A. Poser, T. Ernst, *et al.*, "Simultaneous Multi-Slice fMRI using spiral trajectories", *NeuroImage*, vol. 92, pp. 8–18, 2014.

[178] B. Bilgic, B. A. Gagoski, S. F. Cauley, *et al.*, "Wave-CAIPI for highly accelerated 3D imaging", *Magnetic Resonance in Medicine*, vol. 73, no. 6, pp. 2152–2162, 2015.

[179] K. Setsompop, B. A. Gagoski, J. R. Polimeni, *et al.*, "Blipped-controlled aliasing in parallel imaging for simultaneous multislice echo planar imaging with reduced g-factor penalty", *Magnetic Resonance in Medicine*, vol. 67, no. 5, pp. 1210–1224, 2012.

[180] C. Y. Lin and J. A. Fessler, "Efficient Regularized Field Map Estimation in 3D MRI", *IEEE Transactions on Computational Imaging*, vol. 6, pp. 1451–1458, 2020.

List of Figures

List of Tables

List of Publications

Papers

- Veldmann M, Ehses P, Chow K, Nielsen JF, Zaitsev M, Stöcker T. "Open-source MR imaging and reconstruction workflow". *Magn Reson Med.* 2022;88:2395-2407, DOI: `https://doi.org/10.1002/mrm.29384`.
  Chapter 3 corresponds to this article. Personal contribution: 85% (Pipeline conceptualization and implementation, data acquisition, data analysis, manuscript writing)

- Veldmann M, Edwards LJ, Pine KJ, Ehses P, Ferreira M, Weiskopf N, Stöcker T. "Improving MR axon radius estimation in human white matter using spiral acquisition and field monitoring". *Magn Reson Med.* 2024;92:1898-1912, DOI: `https://doi.org/10.1002/mrm.30180`
  Chapter 4 corresponds to this article. Personal contribution: 80% (Sequence design, implementation of image reconstruction, data acquisition, field measurements, data analysis, manuscript writing)

- Valsala PI, Veldmann M, Bosch D, Scheffler K, Ehses P. "Submillimeter balanced SSFP BOLD–functional MRI accelerated with 3D stack-of-spirals at 9.4 T". *Magn Reson Med.* 2024;92:186-201, DOI: `https://doi.org/10.1002/mrm.30064`.

- Niesen S, Veldmann M, Ehses P, Stöcker T. "Spiral 3DREAM sequence for fast whole-brain B1 Mapping". *Magn Reson Med.* 2025;93:321-329, DOI: `https://doi.org/10.1002/mrm.30282`
  Chapter 5 corresponds to this article. Personal contribution: 45% (Shared equally with co-author S. Niesen: Sequence design, implementation of image reconstruction, data acquisition, manuscript writing)

Conference contributions

- Veldmann M, Löwen D, Stöcker T. "Whole-brain diffusion-weighted imaging at 7T with universal multiband GRAPE pTx pulses", *ESMRMB Congress 2024*, oral presentation

Chapter 6 is partly based on this abstract. Personal contribution: 70% (Sequence design, implementation of image reconstruction, data acquisition, data analysis, manuscript writing). PTx pulse design was done by co-author D. Löwen.

- Niesen S, Veldmann M, Stöcker T. "Tensor-valued encoded diffusion MRI with spiral readout for whole-brain mapping of microscopic fractional anisotropy", *Proc. Intl. Soc. Mag. Reson. Med. 32;5100*

- Veldmann M, Löwen D, Pracht ED, Ehses P, Stirnberg R, Stöcker T. "Towards whole-brain diffusion-weighted imaging at 7T using universal multi-band kT-spokes pTx pulses", *ESMRMB Congress 2023*, poster presentation
  Chapter 6 is partly based on this abstract. Personal contribution: 70% (Sequence design, implementation of image reconstruction, data acquisition, data analysis, manuscript writing). PTx Pulse design was done by co-author D. Löwen (except for VERSE gradients).

- Veldmann M, Edwards LE, Pine KJ, Ehses P, Weiskopf N, Stöcker T. "Spiral readout improves in vivo MR axon radius estimation in human white matter", *Proc. Intl. Soc. Mag. Reson. Med. 31;5172*, poster presentation

- Veldmann M, Niesen S, Ehses P, Stöcker T. "Spiral 3DREAM sequence for fast whole-brain B1 Mapping", *Proc. Intl. Soc. Mag. Reson. Med. 30;1612*, poster presentation

- Veldmann M, Ehses P, Chow K, Zaitsev M, Stöcker T. "Open-Source MR Imaging Workflow", *Proc. Intl. Soc. Mag. Reson. Med.* 29;729, oral presentation

- Veldmann M, Ehses P, Stöcker T. "Spiral in/out trajectory with GIRF prediction for passband bSSFP fMRI at 7T", *ESMRMB Congress 2020*, oral presentation

- Valsala P, Ehses P, Veldmann M, Scheffler K. "Accelerated 3D stack-of-spiral bSSFP for functional imaging at 9.4T: Pilot study", *Proc. Intl. Soc. Mag. Reson. Med. 30;1102*

- Valsala P, Ehses P, Veldmann M, Scheffler K. "Rapid and high-resolution bSSFP fMRI using 3D stack of spirals at 9.4 T", *Proc. Intl. Soc. Mag. Reson. Med. 31;1278*

Acknowledgements

I am grateful to all those people who have supported and guided me throughout the last years. This work would not have been possible without their contributions and encouragement. I would like to thank

- my supervisor Prof. Dr. Tony Stöcker for giving me the opportunity to work on this exciting PhD project after I finished my Master Thesis in his group. I am grateful for his guidance, support, the freedom to explore my own ideas and his open ear for any questions.
- Philipp Ehses, who introduced me to the topic of MRI already during my Master Thesis. Thanks for patiently answering all my questions and for many fruitful discussions.
- my fellow Phd (and Postdoc) colleagues Matthias Serger, Simon Blömer, Difei Wang, Daniel Löwen, Yannik Völzke, Svenja Niesen and Monica Ferreira. Thanks for many interesting conversations, for helping each other out and for the exciting games at the Kicker table.
- Ed Pracht and Rüdiger Stirnberg for many helpful discussions on different scientific and technical aspects of MRI.
- Sascha Brunheim for his technical support especially with the field probe system and Anke Rühling for introducing me to the MRI scanning procedures.
- the whole MR Physics group at the DZNE for the great (working) atmosphere. It is a pleasure to work in such a friendly and supportive environment.
- Kerrin Pine, Luke Edwards and Nik Weiskopf from the MPI in Leipzig for giving me the chance to spend three great weeks in their group and do a research project on the Connectom scanner.
- all co-authors of my publications. Without their contributions many parts of this thesis would not have been possible.
- Matthias Serger, Philipp Ehses, Yannik Völzke and Daniel Löwen for proofreading parts of this thesis.

- my family and friends, and especially Kik, for their continuous support and encouragement.

Eidesstattliche Erklärung

Ich versichere an Eides statt, dass die Dissertation von mir selbstständig und ohne unzulässige fremde Hilfe unter Beachtung der „Grundsätze zur Sicherung guter wissenschaftlicher Praxis an der Heinrich-Heine-Universität Düsseldorf“ erstellt worden ist.

Ort, Datum Unterschrift